

**DOT/FAA/TC-17/18**

Federal Aviation Administration  
William J. Hughes Technical Center  
Aviation Research Division  
Atlantic City International Airport  
New Jersey 08405

# **Effects of Repair Procedures on Bonded Repairs of Airframe Structures**

November 2017

Final Report

This document is available to the U.S. public through the National Technical Information Services (NTIS), Springfield, Virginia 22161.

This document is also available from the Federal Aviation Administration William J. Hughes Technical Center at [actlibrary.tc.faa.gov](http://actlibrary.tc.faa.gov).



U.S. Department of Transportation  
**Federal Aviation Administration**

## **NOTICE**

This document is disseminated under the sponsorship of the U.S. Department of Transportation in the interest of information exchange. The U.S. Government assumes no liability for the contents or use thereof. The U.S. Government does not endorse products or manufacturers. Trade or manufacturers' names appear herein solely because they are considered essential to the objective of this report. The findings and conclusions in this report are those of the author(s) and do not necessarily represent the views of the funding agency. This document does not constitute FAA policy. Consult the FAA sponsoring organization listed on the Technical Documentation page as to its use.

This report is available at the Federal Aviation Administration William J. Hughes Technical Center's Full-Text Technical Reports page: [actlibrary.tc.faa.gov](http://actlibrary.tc.faa.gov) in Adobe Acrobat portable document format (PDF).

**Technical Report Documentation Page**

1. Report No. <b>DOT/FAA/TC-17/18</b>		2. Government Accession No.		3. Recipient's Catalog No.	
4. Title and Subtitle <b>EFFECTS OF REPAIR PROCEDURES ON BONDED REPAIRS OF AIRFRAME STRUCTURES</b>				5. Report Date <b>November 2017</b>	
				6. Performing Organization Code	
7. Author(s) <b>John S. Tomblin, Lamia Salah, Michael Borgman, and Bill Stevenson</b>				8. Performing Organization Report No.	
9. Performing Organization Name and Address <b>National Institute for Aviation Research Wichita State University Wichita, KS 67260</b>				10. Work Unit No. (TRAIS)	
				11. Contract or Grant No.	
12. Sponsoring Agency Name and Address <b>U.S. Department of Transportation FAA Northwest Mountain Regional Office 1601 Lind Ave SW Renton, WA 98057</b>				13. Type of Report and Period Covered <b>Final Report</b>	
				14. Sponsoring Agency Code <b>AIR-100</b>	
15. Supplementary Notes <b>The FAA William J. Hughes Technical Center Aviation Research Division Technical Monitor was Curtis Davies.</b>					
16. Abstract <p>In-service experience has shown that a composite part absorbs as much as 1.2% by weight of moisture throughout its lifetime and may be exposed to maintenance fluids, such as hydraulic fluid, jet fuel (JF), and paint stripper (PS). Leaking hydraulic and fuel lines in aircraft components may contaminate the surrounding composite parts that could possibly require repair at a later date. Damage threats, particularly impact events that result in little or no visual surface indication, are another concern. Damage to a bonded repair is of particular interest, as visible indication of damage may not be present and the resulting damage may be different in size and may exhibit a different morphology, depending on the impact site in the repair. The goal of this report was to investigate the effects of different types of contaminants and impact damage on the ultimate strength and durability of bonded scarf repairs to a laminate substrate. Repair specimens were subjected to impact damage and pre-bond contamination. Five different contaminants were considered in this study, including JF, PS, Skydrol, water, and perspiration. Test results indicate that pre-bond contamination degrades the load carrying capability of a scarf repair and that impact sites in a scarf repair affect the size of the damage produced and the associated residual strength of the damaged repair. This report demonstrates that the integrity of bonded structures and repairs is strongly dependent on the processes used for bonding/repair</p>					
17. Key Words <b>Bonded repair, Composite</b>			18. Distribution Statement <b>This document is available to the U.S. public through the National Technical Information Service (NTIS), Springfield, Virginia 22161. This document is also available from the Federal Aviation Administration William J. Hughes Technical Center at <a href="http://actlibrary.tc.faa.gov">actlibrary.tc.faa.gov</a>.</b>		
19. Security Classif. (of this report) <b>Unclassified</b>		20. Security Classif. (of this page) <b>Unclassified</b>		21. No. of Pages <b>86</b>	22. Price

## ACKNOWLEDGMENTS

The authors would like to dedicate this report to the late Dr. Bill Stevenson for his invaluable contributions to this research effort.

The authors would like to thank Jim Westerman, David Shiflett, and Robert Bohaty from Spirit Aerosystems for their guidance and invaluable support. The authors would also like to acknowledge the efforts of Irish Alcalen for conducting the contact angle experiments, Abhijit Sonambekar for coordinating various tasks of the project, Kim-Leng Poon for machining the samples, and Chaminda Gomes and Ruchira Walimunige for conducting the mechanical tests.

## TABLE OF CONTENTS

	Page
EXECUTIVE SUMMARY	xii
1. INTRODUCTION	1
1.1 The Implementation of Composite Materials in Airframe Structures— Technological Challenges	1
1.2 In-Service Experience with Bonded Structures and Repairs	3
1.3 Adhesion and Bonding in Polymeric Materials and Composites/ Surface Free Energy	5
1.4 Environmental Induced Degradation of Adhesively Bonded Joints	7
2. RESEARCH METHODOLOGY	8
2.1 Research Objectives	8
2.2 Specimen Configuration	9
2.3 Panel Manufacturing/Subpanel Machining and Scarfing	10
2.4 Pre-Bond Contamination Procedure	11
2.5 OEM Repair/Damage Tolerance Coupon Repair Procedure	12
2.6 Field Repair/Contamination Coupon Repair Procedure	13
2.6.1 Tool, Scarfed Panel Preparation	13
2.6.2 Repair Ply Marking	14
2.6.3 Adhesive Film Application/Repair Ply Lay-Up	14
2.6.4 Thermocouple Placement	15
2.6.5 Final Bagging	15
2.7 Impact Procedure	18
2.8 Moisture Equilibrium/Moisture Absorption/Desorption Cycles	27
2.9 Mechanical Testing	28
3. DAMAGE TOLERANCE INVESTIGATION RESULTS	30
3.1 18-Ply Repair Laminate Damage Tolerance Results	31
3.2 48-Ply Repair Laminate Damage Tolerance Results	45
4. CONTAMINATION/WEAK BOND INVESTIGATION RESULTS.	60
4.1 Surface Analysis Prior to Panel Repair	60
4.2 Contamination/Weak Bond Investigation Data Summary	63
5. CONCLUSIONS AND RECOMMENDATIONS	68
6. REFERENCES	71

## LIST OF FIGURES

Figure		Page
1	Composites in commercial transport aircraft	1
2	Design load and damage considerations for durability and design [5]	3
3	Contribution to adhesion: (a) mechanical interlocking, (b) interdiffusion of chains, (c) electrical interactions, and (d) chemical interactions	6
4	Contact angle between the liquid and solid surface	7
5	Local environment of an atom in the bulk of a material, on a plane surface, and on a rough surface	7
6	Repair coupon configuration	9
7	Repair coupon scarf grinding setup	10
8	Machined/scarfed subpanels ready for repair	11
9	Water (moisture conditioning) exposure	11
10	SH exposure	12
11	DVD process diagram	13
12	Scarfed panels cleaned and placed on the repair tool prior to bonding	14
13	Ply location markings/adhesive application prior to repair ply application	14
14	Individual repair ply lay-up procedure	15
15	Thermocouple placement	15
16	Caul sheet placement/repair panels ready for bagging	16
17	Repair panel bagging procedure	16
18	Representative c-scans of panels contaminated with JF prior to repair	16
19	Representative c-scans of panels exposed to PR prior to repair	17
20	Representative c-scans of panels exposed to PS (methylene chloride) prior to repair	17
21	Representative c-scans of panels exposed to SH prior to repair	17
22	Representative c-scans of panels exposed to water prior to repair	18
23	Instron Dynatup	19
24	Damage site for the impact specimens TF (tip far)	20
25	Damage site for the impact specimens TN (tip near)	20
26	Damage site for the impact specimens CN (center)	20
27	Typical force time history for 18-E1-10-TF laminates	21
28	Typical force displacement curve for 18-E1-10-TF laminates	21

29	Typical force time history for 18-E2-20-TF laminates	22
30	Typical force displacement curve for 18-E2-20-TF laminates	22
31	Typical force time history for 48-E1-10-CN laminates	23
32	Typical force displacement curve for 48-E1-10-CN laminates	23
33	Typical force time history for 48-E1-20-TF laminates	24
34	Typical force displacement curve for 48-E1-20-TF laminates	24
35	Typical force time history for 48-E2-20-TN laminates	25
36	Typical force displacement curve for 48-E2-20-TF laminates	25
37	C-Scans of 18-E1-20-CN-RTF/18-E1-20-TF-RTF/18-E1-20-TN-RTA panels	26
38	C-Scans of 48-E2-20-TN-RTA/48-E2-20-TN-RTF panels	26
39	C-Scan of 48-E2-20-TF-RTF panel	26
40	C-Scans of 48-E2-20-CN-RTA/48-E2-20-CN-RTF panels	27
41	Moisture absorption/desorption cycle for 32-ply laminates (parent material)	28
42	The ARAMIS test setup	29
43	Repaired laminates strain gage layout	29
44	Impact data summary for all 18-ply scarf repair specimens	32
45	C-Scans of 18-ply-E1-10-TN-RTA of damage area and depth, respectively: (a) 1.22 in <sup>2</sup> , 0.006 in; (b) 0.94 in <sup>2</sup> , 0.007 in; (c) 2.61 in <sup>2</sup> , 0.006 in	33
46	C-Scans of 18-E1-10-TF-RTA-(1, 2, 3) of damage area and depth, respectively: (a) 2.51 in <sup>2</sup> , 0.0085 in; (b) 2.12 in <sup>2</sup> , 0.01 in; (c) 1.32 in <sup>2</sup> , 0.0105 in	33
47	C-Scans of 18-E1-10-CN-RTA-(1, 2, 3) of damage area and depth, respectively: (a) 1.07 in <sup>2</sup> , 0.0061 in; (b) 1.17 in <sup>2</sup> , 0.006 in; (c) 1.23 in <sup>2</sup> , 0.0065 in	33
48	C-Scans of 18-E2-10-TN-RTA-(1, 2, 3); damage area and depth, respectively: (a) 0.51 in <sup>2</sup> , 0.007 in; (b) 0.66 in <sup>2</sup> , 0.0065 in; (c) 0.62 in <sup>2</sup> , 0.0085 in	33
49	C-Scans of 18-E2-10-TF-RTA-(1, 2, 3) of damage area and depth, respectively: (a) 2.30 in <sup>2</sup> , 0.0075 in; (b) 1.49 in <sup>2</sup> , 0.0075 in; (c) 1.84 in <sup>2</sup> , 0.008 in	34
50	C-Scans of 18-E2-10-CN-RTA-(1, 2, 3) of damage area and depth, respectively: (a) 1.54 in <sup>2</sup> , 0.0095 in; (b) 1.57 in <sup>2</sup> , 0.004 in; (c) 1.60 in <sup>2</sup> , 0.0055 in	34
51	C-Scans of 18-E1-20-TN-RTA-(1, 2, 3) of damage area and depth, respectively: (a) 0.73 in <sup>2</sup> , 0.0065 in; (b) 0.82 in <sup>2</sup> , 0.0065 in; (c) 2.56 in <sup>2</sup> , 0.0075 in	34
52	C-Scans of 18-E1-20-TF-RTA-(1, 2, 3) of damage area and depth, respectively: (a) 0.83 in <sup>2</sup> , 0.0095 in; (b) 1.16 in <sup>2</sup> , 0.0095 in; (c) 0.89 in <sup>2</sup> , 0.0085 in	34

53	C-Scans of 18-E1-20-CN-RTA-(1, 2, 3) of damage area and depth, respectively: (a) 0.92 in <sup>2</sup> , 0.0065 in; (b) 1.39 in <sup>2</sup> , 0.0065 in; (c) 1.02 in <sup>2</sup> , 0.0075 in	35
54	C-Scans of 18-E2-20-TN-RTF-(1, 2, 3) of damage area and depth, respectively: (a) 0.51 in <sup>2</sup> , 0.0095 in; (b) 0.54 in <sup>2</sup> , 0.01 in; (c) 0.67 in <sup>2</sup> , 0.0085 in	35
55	C-Scans of 18-E2-20-TF-RTF-(1, 2, 3) of damage area and depth, respectively: (a) 0.93 in <sup>2</sup> , 0.012 in; (b) 0.74 in <sup>2</sup> , 0.0115 in; (c) 0.52 in <sup>2</sup> , 0.0095 in	35
56	C-Scans of 18-E2-20-CN-RTF-(1, 2, 3) of damage area and depth, respectively: (a) 1.72 in <sup>2</sup> , 0.006 in; (b) 1.29 in <sup>2</sup> , 0.007 in; (c) 1.11 in <sup>2</sup> , 0.006 in	35
57	Representative load vs. displacement curves of damaged 18-ply laminate scarf repairs tested at room temperature (1:10 scarf rate)	36
58	Representative load vs. displacement curves of damaged 18-ply laminate scarf repairs tested at room temperature (1:20 scarf rate)	37
59	Residual strength after damage (static strength) of 18-ply laminate scarf repair configurations tested at room temperature	37
60	Far field parent strain at failure of 18-ply laminate scarf repair configurations	38
61	Y-strain distribution for 18-ply-E1-10-TN-RTA-02 scarf repair specimen	39
62	Y-strain distribution for 18-ply-E2-20-TN-RTA-03 scarf repair specimen	39
63	Y-strain distribution for 18-ply-E1-20-TF-RTA-03 scarf repair specimen	39
64	Y-strain distribution for 18-ply-E2-20-TF-RTA-02 scarf repair specimen	40
65	Y-strain distribution for 18-ply-E1-20-CN-RTA-02 scarf repair specimen	40
66	Y-strain distribution for 18-ply-E2-20-CN-RTA-03 scarf repair specimen	40
67	Failure modes: 18-ply-E1-10-CN-RTA-XX	43
68	Failure modes: 18-ply-E1-20-TF-RTA-XX	43
69	Failure modes: 18-ply-E2-10-CN-RTA-XX	43
70	Failure modes: 18-ply-E2-10-TF-RTA-XX	44
71	Failure modes: 18-ply-E2-20-CN-RTA-XX	44
72	Failure modes: 18-ply-E2-20-TN-RTA-XX	45
73	Impact data summary for all 48-ply scarf repair specimens	46
74	C-scans of 48-E1-10-TN-RTA-(1, 2, 3) of damage area and depth, respectively: (a) 2.1368 in <sup>2</sup> , 0.009 in; (b) 2.054 in <sup>2</sup> , 0.0095 in; (c) 2.22 in <sup>2</sup> , 0.0095 in	46
75	C-scans of 48-E1-10-TF-RTA-(1, 2, 3) of damage area and depth, respectively: (a) 2.152 in <sup>2</sup> , 0.011 in; (b) 2.1564 in <sup>2</sup> , 0.0115 in; (c) 2.0228 in <sup>2</sup> , 0.0105 in	46
76	C-scans of 48-E1-10-CN-RTA-(1, 2, 3) of damage area and depth, respectively: (a) 6.2796 in <sup>2</sup> , 0.0095 in; (b) 5.0008 in <sup>2</sup> , 0.008 in; (c) 4.808 in <sup>2</sup> , 0.012 in	47

77	C-scans of 48-ply-E2-10-TN-RTA of damage area and depth, respectively: (a) 1.91 in <sup>2</sup> , 0.0085 in; (b) 1.88 in <sup>2</sup> , 0.011 in; (c) 1.87 in <sup>2</sup> , 0.0085 in	47
78	C-scans of 48-ply-E2-10-TF-RTA of damage area and depth, respectively: (a) 2.56 in <sup>2</sup> , 0.011 in; (b) 2.92 in <sup>2</sup> , 0.009 in; (c) 1.75 in <sup>2</sup> , 0.013 in	47
79	C-scans of 48-ply-E2-10-CN-RTA damage area and depth, respectively: (a) 7.22 in <sup>2</sup> , 0.008 in; (b) 6.30 in <sup>2</sup> , 0.008 in; (c) 7 in <sup>2</sup> , 0.008 in	47
80	C-scans of 48-E1-20-TN-RTA-(1, 2, 3) of damage area and depth, respectively: (a) 2.8312 in <sup>2</sup> , 0.0105 in; (b) 2.0252 in <sup>2</sup> , 0.01 in; (c) 3.894 in <sup>2</sup> , 0.011 in	48
81	C-scans of 48-E1-20-TF-RTA-(1, 2, 3) of damage area and depth, respectively: (a) 3.4948 in <sup>2</sup> , 0.0105 in; (b) 2.8096 in <sup>2</sup> , 0.012 in; (c) 2.7856 in <sup>2</sup> , 0.012 in	48
82	C-scans of 48-E1-20-CN-RTA-(1, 2, 3) of damage area and depth, respectively: (a) 3.9376 in <sup>2</sup> , 0.008 in; (b) 5.2012 in <sup>2</sup> , 0.0075 in; (c) 3.6064 in <sup>2</sup> , 0.008 in	48
83	C-scans of 48-E2-20-TN-RTA-(1, 2, 3) of damage area and depth, respectively: (a) 2.118 in <sup>2</sup> , 0.01 in; (b) 2.016 in <sup>2</sup> , 0.011 in; (c) 1.914 in <sup>2</sup> , 0.0095 in	48
84	C-scans of 48-E2-20-TF-RTA-(1, 2, 3) of damage area and depth, respectively: (a) 2.326 in <sup>2</sup> , 0.0075 in; (b) 1.968 in <sup>2</sup> , 0.0085 in; (c) 1.602 in <sup>2</sup> , 0.0085 in	49
85	C-scans of 48-E2-20-CN-RTA-(1, 2, 3) of damage area and depth, respectively: (a) 4.9112 in <sup>2</sup> , 0.009 in; (b) 3.7932 in <sup>2</sup> , 0.0095 in; (c) 4.9392 in <sup>2</sup> , 0.0115 in	49
86	Representative load vs. displacement curves of damaged 48-ply laminate scarf repairs tested at room temperature (1:20 scarf rate)	50
87	Representative load vs. displacement curves of damaged 48-ply laminate scarf repairs tested at room temperature (1:10 scarf rate)	50
88	Residual strength after damage (static strength) of 48-ply laminate scarf repair configurations	51
89	Far field parent strain at failure of 48-ply laminate scarf repair configurations	52
90	Y-strain distribution 48-ply-E1-10-TN-RTA-2 scarf repair specimen	53
91	Y-strain distribution 48-ply-E1-10-TF-RTA-01 scarf repair specimen	53
92	Y-strain distribution 48-ply-E1-20-TN-RTA-03 scarf repair specimen	54
93	Y-strain distribution 48-ply-E1-20-TF-RTA-01 scarf repair specimen	54
94	Y-strain distribution 48-ply-E2-10-TN-RTA-2 scarf repair specimen	55
95	Y-strain distribution 48-ply-E2-10-TF-RTA-2 scarf repair specimen	55
96	Y-strain distribution 48-ply-E2-20-CN-RTA-03 scarf repair specimen	56
97	Failure modes: 48-ply-E2-10-TN-RTA	59

98	Failure modes 48-ply-E2-20-CN-RTA	59
99	Failure modes, environmental tests, 48-ply-E2-20-CN/48-ply-E1-10-CN (showing disbond/damage to the bondline due to impact at the center of the specimen)	60
100	Low contact angle	61
101	Medium contact angle	61
102	High contact angle	62
103	Contact angle measurements	63
104	SFE measurements	63
105	Normalized strength of PR- and water-contaminated panels (E1 lay-up)	65
106	Normalized strength of PR- and water-contaminated panels (E2 lay-up)	66
107	Normalized strength of PS-, JF-, and SH-contaminated panels (E1 lay-up)	67
108	Normalized strength of PS-, JF-, and SH-contaminated panels (E2 lay-up)	67
109	Failure modes 32-ply-E1-20-JF-180W/32-ply-E1-20-PR-180W	68
110	Failure modes 32-ply-E1-20-SH-180W/32-ply-E1-20-WA75-180W	68

## LIST OF TABLES

Table		Page
1	Damage tolerance test matrix	31
2	The 18-ply-10 fatigue data summary	41
3	The 18-py-20 fatigue data summary	42
4	The 48-ply-10 fatigue data summary	57
5	The 48-ply-20 fatigue data summary	58
6	Contamination investigation test matrix	60

## LIST OF SYMBOLS AND ACRONYMS

AC	Advisory Circular
CN	Scarf center
DVD	Double vacuum debulking JF Jet fuel
NDI	Non-destructive inspection
OEM	Original equipment manufacturer PR Perspiration
PS	Paint stripper
RH	Relative humidity
RTA	Room temperature ambient static
RTF	Room temperature ambient fatigue
SFE	Surface free energy
SH	Skydrol
S-N	Stress (S) vs. the number of cycles to failure (N)
TF	Tip of the scarf from the far side
TN	Tip of the scarf from the near side
TTU	Through-transmission ultrasonics
$T_g$	Glass transition temperature
WA0	Conditioned to 100% moisture equilibrium, then dried back until all moisture was removed
WA25	Conditioned to 100% moisture equilibrium, then dried back to 25% moisture equilibrium (i.e., approximately 0.25% moisture weight percent)
WA50	Conditioned to 100% moisture equilibrium, then dried back to 50% moisture equilibrium (i.e., approximately 0.5% moisture weight percent)
WA75	Conditioned to 100% moisture equilibrium, then dried back to 75% moisture equilibrium (i.e., approximately 0.75% moisture weight percent)

## EXECUTIVE SUMMARY

The use of fiber-reinforced composites in aircraft structural components has increased significantly in the last few decades because of their improved specific strength and stiffness and superior corrosion resistance and fatigue performance with respect to their metal counterparts. When implemented adequately in aircraft components, these materials have the potential to improve airline profitability in terms of lower operating and maintenance costs. With the migration of these new materials from secondary components to primary flight-critical structural elements, new challenges associated with their repair are continually arising and increasing in complexity. Rigorous material, structural, and process substantiation are crucial to ensure the structural integrity of these components.

In-service experience has shown that a composite part absorbs as much as 1.2% by weight of moisture throughout its lifetime. The amount of moisture absorbed is dependent on the material resin system and the environmental conditions to which the part is subjected. Leaking hydraulic and fuel lines in aircraft components may contaminate the surrounding composite parts that could possibly require repair at a later date. Impact damage to a bonded repair may occur with no visible indication of damage/compromised structural integrity. The resulting damage may be different in size and morphology depending on the impact site in the repair.

The objective of this research program was to determine the ultimate strength and durability of bonded scarf repairs of solid laminates subjected to impact damage and pre-bond contamination. Repair data were generated for repair systems representative of factory and field repairs. The factory repairs were used as a baseline for the damage tolerance investigation, whereas the field repairs were used as a baseline for the contamination investigation. Five different contaminants were used for the purpose of the contamination investigation: jet fuel (JF), paint stripper (PS), Skydrol (SH), water (WA75, WA50, WA25, WA0), and perspiration (PR). The JF and SH panels were soaked in the contaminants for 30 days; PR (salt water) was applied to the surface prior to bonding; PS panels were exposed to the contaminant for 6 days; and water panels were exposed to moisture at 85% relative humidity at a temperature of 180°F until moisture equilibrium was achieved. Once 100% moisture equilibrium was achieved (referred to as saturation), panels were subsequently dried to achieve %saturation levels of 75%, 50%, and 25%.

Coupons used for the purpose of the damage tolerance investigation were repaired using the double vacuum debulking process, in which the repair patch was consolidated prior to bonding it to the cured scarfed parent. All repair specimens were impacted at three different impact sites in the scarf region: the tip of the scarf from the far side, the tip of the scarf from the near side, and at the center of the scarf. Test results indicate that pre-bond contamination degrades the load carrying capability of a scarf repair and that impact sites in a scarf repair affect the size of the damage produced and the associated residual strength of the damaged repair. This study demonstrates that the integrity of bonded structures and repairs is strongly dependent on the processes used for bonding/repair.

## 1. INTRODUCTION

### 1.1 THE IMPLEMENTATION OF COMPOSITE MATERIALS IN AIRFRAME STRUCTURES—TECHNOLOGICAL CHALLENGES

The use of fiber-reinforced composites in aircraft structural components has increased significantly in the last few decades because of their improved specific strength and stiffness. Composite materials have the ability to be tailored to the design requirements in various loading directions and their manufacturability allows the possibility of building a part in a single integral shell. Composites have superior corrosion resistance and fatigue endurance compared to their metal counterparts. These features offer the potential for significant weight savings and lower maintenance and operating costs, which can be translated into long-term, more cost-efficient airframes. Manufacturing cost advantages can accrue because of the reduced part count and assembly costs can become lower because composite materials can be molded into aerodynamically efficient complex contours and can be co-cured or co-bonded [1].

Numerous general aviation airframes are using composite materials, including the Cirrus SR22, the Bombardier's new C-Series family (20% composite), the Mitsubishi's new regional jet, and Bombardier's Learjet 85 [1]. Similarly, the use of composite materials in military applications started with the U.S. Navy F-14 and the U.S. Airforce F-15 fighters and has steadily increased with the F-18, the F-22 (at least 33% composites), the B2 stealth bomber, and the V-22 (50% composite weight percent). Figure 1 shows the increased composite structural weight percent in commercial airframes in the last four decades.

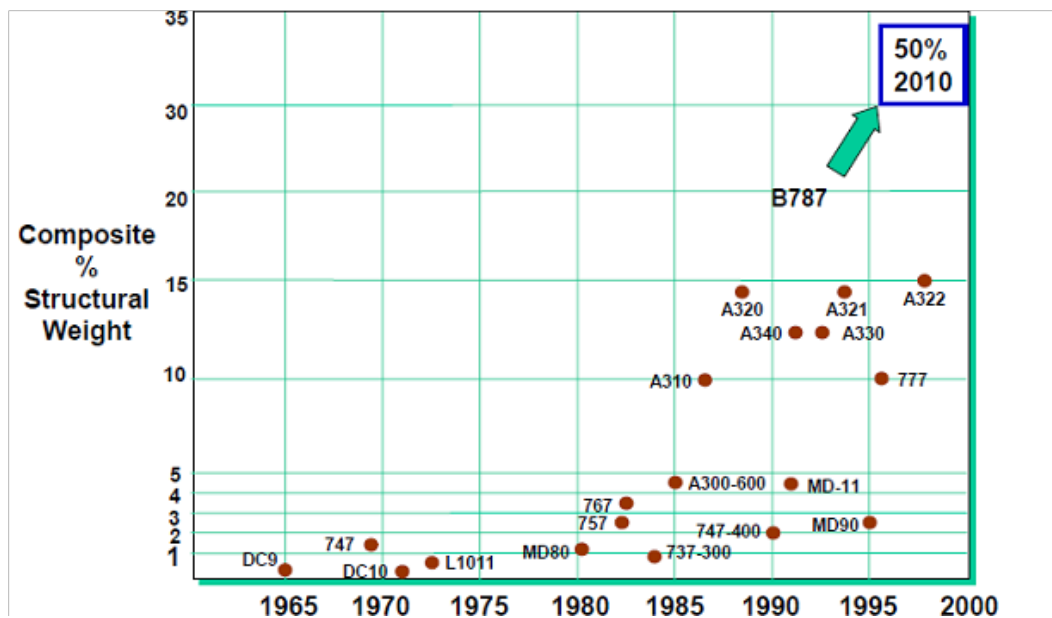
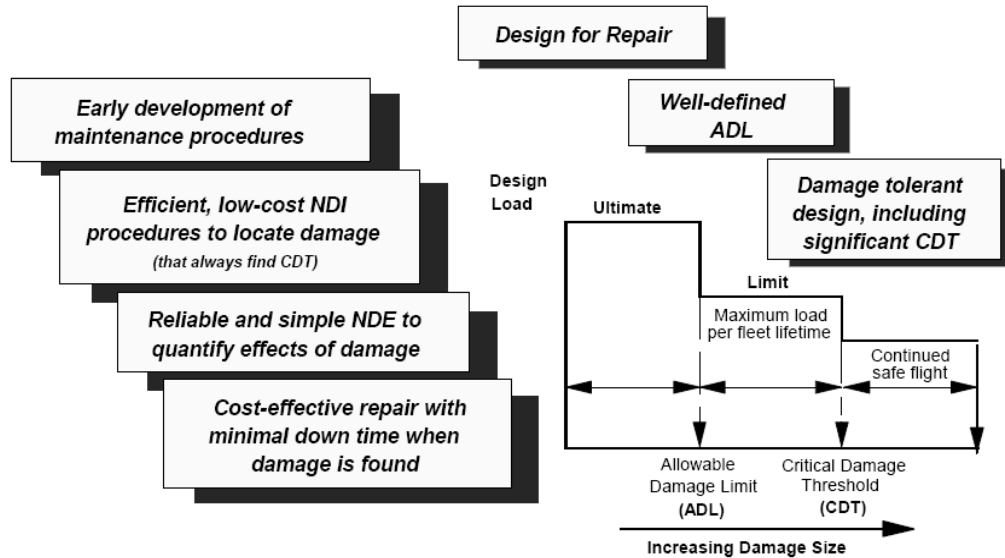


Figure 1. Composites in commercial transport aircraft [1]

To capitalize on the performance benefits that composite materials offer and to enable the continued expansion in the use of these materials in aircraft components, numerous technological challenges have to be overcome in the areas of material fabrication and processes, analysis

methods, structural health monitoring, lightning strike protection, recycling and repair methods, and standardization [2]. To be used in airframe structures, it is necessary that composite components demonstrate equivalent levels of safety, damage tolerance, and durability with respect to their metallic counterparts [2]. With the more recent migration of these new materials from secondary components to primary flight-critical structural elements, challenges associated with the repair of these structures are continually arising and increasing in complexity. Rigorous material, structural, and process substantiation and validation are crucial to ensure the structural integrity of bonded structures and repairs.

Durability, repairability, and maintainability are key elements in the effective design and implementation of composite materials in aircraft structural components [3]. Durability implies that the composite component should maintain its structural integrity in terms of strength, stiffness, and environmental resistance throughout its lifetime. Repairability requires the development of repair philosophies during the design phase that will restore the structure to its original strength and design functionality. This should address the key challenges associated with damage and defect assessment, approved repair materials and design data, process specification, and repair implementation; it should also consider both the factory environment and the in-service maintenance environment. Whereas the parent material, typically autoclave processed, may be used in original equipment manufacturer (OEM) factory repairs, the operators may not be able to use the autoclave processed parent material in depot repairs. Out-of-autoclave systems have to be used for most depot repairs, thus substantiation has to be performed during the design phase to qualify the most suitable materials/systems for repair. It should be stressed that repairability has to be addressed during design so that the choice of parent substrate will dictate the requirements for the repair materials to be used. Material compatibility, mechanical capability, and adequate choice of repair systems (material and adhesive) are critical to producing a structurally sound durable bonded repair. In addition to the importance of choosing the proper material systems for repair, it is also essential to understand the ultimate strength and durability of the given repair under the specified design conditions and the most critical factors affecting the static performance and the long-term durability of the repaired component. This implies the development of a repair allowable database that defines repair materials and processes for a given parent structure/system and the strength and fatigue capability under the specified design conditions. For optimum repair performance, rigorous repeatable procedures specific to the given parent structure/repair systems must be developed, validated, and implemented. Maintainability is also a key element that should be incorporated during design. Simple assemblies and easy access to equipment without the necessity of removing large components can significantly reduce the occurrence of damage and, thus, the need for repairing these structures. The following should be defined during the design phase (see figure 2): (1) maintenance procedures that clearly define the allowable damage limit (ADL) and the critical damage threshold (CDT) for the structure [4]; (2) the qualified repair materials, specifications, and methods; (3) the tooling materials; and (4) efficient and reliable non-destructive inspection (NDI) and repair methods.



**Figure 2. Design load and damage considerations for durability and design [5]**

## 1.2 IN-SERVICE EXPERIENCE WITH BONDED STRUCTURES AND REPAIRS

A repair has the objective of restoring a damaged structure to an acceptable capability in terms of strength, durability, stiffness, functional performance, safety, cosmetic appearance, or service life. The design assessment of a repair for a given loading condition involves: (1) the selection of a repair concept, (2) the choice of the appropriate repair materials and processes, and (3) the specification of the detailed configuration and size of the repair [5]. Current regulations pertaining to bonded joints stipulate the following:

- Title 14 Code of Federal Regulations 23.573 states “the failure of which would result in catastrophic loss of the airplane, the limit load capacity must be substantiated by one of the following methods...”
- Advisory Circular (AC) 20-107B [6] (Proof of structure—Static) states “the effects of repeated loading and environmental exposure which may result in material property degradation should be addressed in the static strength evaluation.”
- AC 20-107B (Proof of Structure—Fatigue and Damage Tolerance) states: “Such evaluation must show that catastrophic failure due to fatigue, environmental effects, manufacturing defects, or accidental damage will be avoided throughout the operational life of the aircraft...”
- AC 20-107B (Proof of Structure, Continued Airworthiness) states “Of particular safety concerns are the issues associated with bond material capabilities, bond surface preparation, cure thermal management...”

A repaired structure must restore the certification basis of the original construction; the repaired part must be capable of sustaining limit load without permanent deformation and ultimate load without catastrophic failure [7]. The repaired part must also be durable (i.e., it must sustain its service loads for periods exceeding the expected life of the aircraft) and damage tolerant).

Deficiencies in the current methodology for certification of bonded structures and repairs have been identified and a more rigorous approach has been advocated [7]. In addition to static, fatigue endurance, and damage tolerance substantiation during certification, the proposed approach promotes the substantiation and validation of the bonding process to demonstrate the environmental durability of the bonded structure.

Adhesively bonded repairs have significant advantages over bolted repairs. Adhesively bonded repairs can restore a composite structure's original strength, are more fatigue resistant because of the absence of stress concentrations that occur at fasteners, and are significantly lighter than bolted repairs because of the absence of fastener hardware. Adhesively bonded repairs are very efficient compared to mechanically fastened repairs, have demonstrated to be a cost effective technology to support aging aircraft [8], and have shown, in some cases, to be the sole alternative to retiring aircraft components [9].

Adhesively bonded repairs have limitations because a bonded joint is a single joint; thus, there is no redundancy in the load path [7, 10, and 11]. Furthermore, adhesively bonded repair load carrying capabilities are dependent on the adhesive properties, which vary with temperature. Therefore, it is very important to ensure that the repair adhesive is capable of maintaining adequate strength and durability across service environments and temperatures. Moreover, there are no NDI methods that can provide assurance of absolute bond integrity. The current methods cannot assess the quality of the bonded repair, more specifically, the integrity of the repair interface. As a consequence, a deficient or degraded repair may not be detected until it actually fails or disbonds, leading to a possible catastrophic failure of the repaired part. Adhesively bonded repairs are process dependent and, therefore, repair technicians and mechanics must have adequate training to ensure that the bonding process is successfully completed and to ensure the repeatability and structural integrity of the bond [12]. Training should address the general procedures and fundamentals associated with processing bonded composite repairs, but also the specifics and the differences between the various systems (e.g., pressure, drying, and debulking requirements). Repair processes have to be adequately and effectively validated and a repair quality management structure should be established to ensure the structural integrity and repeatability of these bonded repairs [7].

In-service experience with bonded repairs to metallic airframes has demonstrated outstanding performance in which reliable processes have been used in the implementation of these repairs [13], but also numerous in-service failures have been caused by the use of deficient processes [14 and 15]. A survey of defects reported by the Royal Australian Air Force showed that adhesive bond failures accounted for 53% of the deficiencies reported. Most failures reported can be attributed to adhesion failures due to bond interfacial degradation [15]. Rigorous surface preparation yielding a clean, chemically active interface resistant to environmental degradation is key to ensuring the long-term durability of bonded repairs.

Three main failure modes in bonded structures include adhesion, cohesion, and a mix mode that consists of both adhesion and cohesion. Adhesion failures are caused by a deficient process due to pre-bond contamination, interfacial degradation during service, or inadequate cure parameters/heat application during cure. The classic example is the formation of hydrated oxides at the surface of aluminum interfaces causing progressive degradation of the chemical bonds

leading to interfacial failures, sometimes occurring even without the presence of any flight loads. The adhesion failure is characterized by a failure of the interface in which the entire adhesive layer is present on only one of the fractured surfaces; a cohesion failure is an adhesive present on both fractured surfaces; a mixed-mode failure is when both cohesion and adhesion failures can be identified [16]. Cohesion failures can be attributed to poor design such as residual thermal stresses, stiffness mismatch between adherends, poor selection of repair materials, or inadequate repair overlap. Cohesion failures may occur because of porous bondlines resulting from the curing process/adhesive exposure to pre-bond moisture. Close examination of an in-service failure of a sandwich component showed extensive micro-voiding in the cell area of the bond and in the fillet area between the core and the adhesive [16]. Mixed mode failures result from the progressive decay of the interfacial bonds. As the bond degrades, the plane of failure shifts from the plane of the adhesive carrier to the interface [16].

### 1.3 ADHESION AND BONDING IN POLYMERIC MATERIALS AND COMPOSITES/ SURFACE FREE ENERGY

To understand bond formation and subsequent degradation, it is necessary to understand the mechanism(s) of adhesion. “Adhesion is the phenomenon of binding together the surfaces of condensed (either liquid or solid) phases brought into contact with each other” [17]. Adhesives are materials used to bond together two substrates and prevent them from separation [18]. Adhesives must wet the surface that they are in contact with (i.e., the adhesives must spread onto the surface and achieve a very low contact angle with respect to the wetted surface). Furthermore, they must harden to a cohesively strong solid. Adhesives either contain polymers or form polymers during the bonding process. Polymers are identical chemical units joined together by covalent bonds and may be linear, branched, or cross linked. The resulting bulk polymer structure is completely random and does not follow a specific order; it is amorphous. All structural adhesives are cross linked to eliminate creep deformation [18 and 19].

Epoxy resins are thermosetting polymers widely used in structural adhesives and matrix resins for composites, but they can also be used as surface coatings. Cross linking occurs primarily by the reaction of epoxide groups, molecules containing a three-membered ring consisting of one oxygen atom and two carbon atoms. Four mechanisms, involving both physical and chemical interactions working alone or together are used to describe the theory of adhesion: mechanical interlocking, interdiffusion, electrostatic attractions, and chemical interactions, with the last being the most widely accepted [20]. Interdiffusion of long-chain molecules occurs when two polymers are placed in close contact at temperatures above their glass transition temperature ( $T_g$ ) and depends on the degree of compatibility of the polymers. Chemical interactions between two bodies involve the contribution of different intermolecular and interatomic forces: van der waal forces and the formation of true chemical bonds, mainly ionic, covalent, or hydrogen bonds (shown in figure 3).

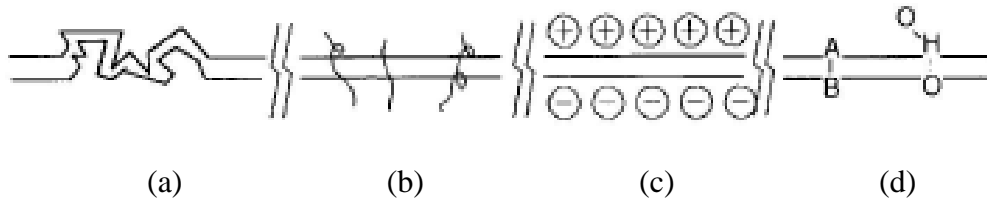


**Figure 3. Contribution to adhesion: (a) mechanical interlocking, (b) interdiffusion of chains, (c) electrical interactions, and (d) chemical interactions [20]**

The mechanical properties of composites are directly related to the interfacial characteristics between the fibers and the matrix and, more specifically, the chemical interactions between the resin and the reinforcing fibers. Optimal adhesion requires complete wetting of the fibers by the resin during the manufacturing process. Coupling agents are used with glass fibers to produce a more chemically reactive interface. Carbon fibers are typically subjected to oxidative treatments to chemically activate their surfaces. This process allows the removal of the fiber outer layer and the formation of oxygen-containing surface groups favorable to adhesion with the matrix resin [19]. Optimum interfacial properties between the parent substrate, adhesive, and repair are key to adequate adhesion and integrity of the bonded structure.

For structural applications, good strength, stiffness, and fracture toughness properties are necessary to meet damage tolerance requirements. Fracture toughness is the amount of energy absorbed during fracture. Optimal interfacial strength between the fiber and the matrix is necessary to achieve a good compromise between the requirements for structural stiffness, strength, and fracture resistance needed to meet damage tolerance requirements. Good interfacial adhesion is required to prevent fibers from buckling, but a very high interfacial strength implies a lower fracture toughness [19]. When a weak interface exists between the fibers and the matrix, a crack propagating through the matrix causes the interface to disbond and is subsequently deflected along the weak interface. As a result, the crack tip driving force is reduced, thus, increasing the fracture toughness of the material. When a strong interface exists between the fibers and the matrix, a crack propagating through the matrix yields a fiber fracture and redistributes the load to the surrounding matrix, thus, increasing the stress intensity ahead of the crack tip and reducing the fracture toughness of the material [21].

All adhesive bonds form by placing an adhesive that is liquid at the time of wetting on a solid interface. Wetting or spreading of a liquid along a liquid/solid interface occurs when the energy of the system is minimized as the liquid and its components interact [22]. This system is typically characterized by the angle (known as contact angle) formed by the liquid drop onto the solid, as shown in figure 4. Surface free energy (SFE) is the excess energy present in a surface as a result of the force imbalance between molecules at that surface. As shown in figure 5 [23], a molecule in the bulk phase is subjected to a symmetrical force field, but this is not the case for a molecule at the material interface yielding an interfacial energy as a result of this force imbalance [17, 24, and 25]. Surface energy  $\gamma_{sv}$  [22] is defined as the total SFE ( $G$ ) per unit area

(A) at constant temperature ( $T$ ), pressure ( $P$ ), and moles ( $n$ ):

$$\gamma_{sv} = \left( \frac{\partial G}{\partial A} \right)_{T, P, n} \quad (1)$$

Surface and interfacial energies are related by the Young Equation as follows:

$$\gamma_{sv} - \gamma_{sl} = \gamma_{lv} \cos \theta \quad (2)$$

In figure 5, *SV*, *LV*, and *SL* refer to the solid/vapor, liquid/vapor surfaces, and the solid/liquid interface, respectively.

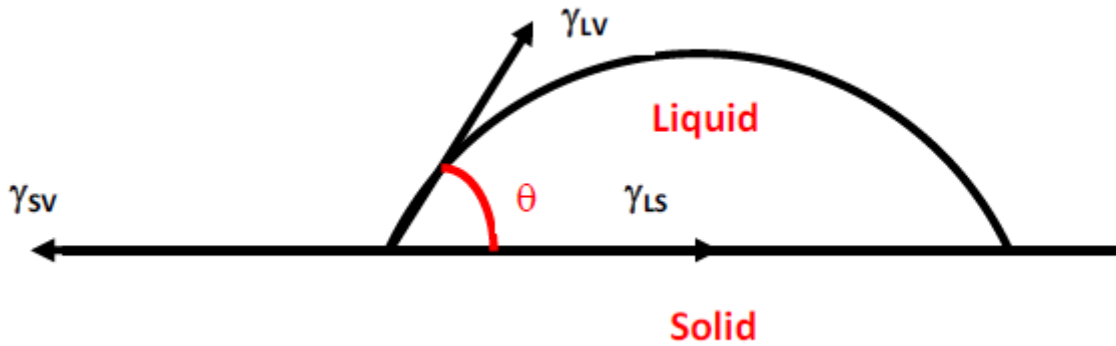


**Figure 4. Contact angle between the liquid and solid surface**

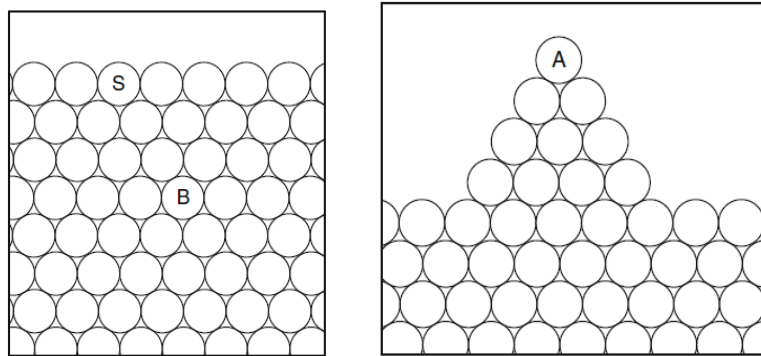


**Figure 5. Local environment of an atom in the bulk of a material, on a plane surface, and on a rough surface**

#### 1.4 ENVIRONMENTAL INDUCED DEGRADATION OF ADHESIVELY BONDED JOINTS

To utilize the full potential of composite structures, it is necessary to understand their response when subjected to environmental exposure. To characterize a material's hygrothermal effects, the following parameters must be known: the temperature and moisture distributions (assuming fickian diffusion at low temperatures and humidity and non-Fickian diffusion at elevated temperatures and moisture levels), the maximum moisture content, the diffusivity, and the hygrothermal stresses and strains [24]. It should be noted that environmental cycling is typically associated with increased moisture uptakes with data varying for different materials, if not

contradictory [24, 25]. Some systems may show significant degradation with hygrothermal cycling and, for others, minimal or no deterioration is observed.

The absorption of water in polymeric materials is a function of free volume, which is a direct function of molecular packing, and the polymer-water affinity. The degree of cure of a polymer affects its crosslink density and, therefore, the amount of free volume in the network. An imperfect state of cure yields a relatively loose network structure with a higher free volume and thus, a higher moisture uptake [26]. The absorption of water in adhesively bonded joints may either affect the interface or the bulk adhesive properties by one or more of the following: polymer plasticization, a reversible process that decreases the  $T_g$  of the polymer, irreversible changes to the polymer molecular network, degradation of the adhesive/adherend interface, or swelling [27].

The effects of moisture uptake on the polymer properties depend on its chemical network as well as its crosslink density and, therefore, its degree of cure [25]. In high-temperature curing of bonded repairs and joints, pre-bond moisture may cause one or more of the following: inhibit the formation of chemical bonds at the adherend/adhesive interface, interfere with the cross-linking of the adhesive during cure, or cause porosity and micro-voiding in the adhesive bondline [28]. Environmental durability is crucial in ensuring the structural integrity and continuing airworthiness of bonded repairs and structures [29]. Because the short-term strength demonstrated by a bond does not necessarily translate into its long-term durability, current certification requirements concentrating solely on static strength and fatigue endurance may not guarantee continued airworthiness for bonded repairs and structures [29].

## 2. RESEARCH METHODOLOGY

### 2.1 RESEARCH OBJECTIVES

The long-term durability and damage tolerance of adhesively bonded structures and repairs are key elements in the acceptance and implementation of bonded technology by OEMs and operators in primary structural applications. Rigorous repair processes are crucial in the environmental resistance and the long-term durability of bonded structures and repairs. Interfacial degradation of bonded structures is the main failure mode reported in the literature. It occurs when the chemical bonds between the substrate and the adhesive resulting from a defective process are gradually weakened as the bond interface is subjected to mechanical loading and environmental exposure or when the bonded component is subjected to impact damage causing interfacial disbonds, adherend matrix cracking, and fiber fracture.

Numerous articles have been written on the effects of inadequate bond processes and subsequent bond failures on adhesively bonded structures and repairs to metallic substrates [11, 14, and 15]. Most failures reported are interfacial failures resulting from a deficient bonding process yielding weak bonds susceptible to environmental degradation that decay over time and may disbond even in the absence of flight loads [16]. The problem is further exacerbated by the lack of inspection methods to interrogate the structural integrity of degraded interfaces and to detect these weak bonds. Thus, it is essential to understand the fundamental requirements for the formation of durable bonds and the factors inhibiting the formation of strong chemical bonds that may result in a premature failure of the bonded structure.

In-service experience has shown that a composite part will absorb as much as 1.2% by weight of moisture throughout its lifetime [30 and 31] and may be exposed to maintenance fluids such as hydraulic fluid, jet fuel (JF), and paint stripper (PS). Leaking hydraulic and fuel lines may contaminate the surrounding composite part, which may need to be repaired later. Impact damage threats, particularly impact events that result in little or no visual surface indication, are another concern. Damage to a bonded repair is of particular interest as no visible indication of damage may be present and the resulting damage may be different in size and morphology depending on the impact site in the repair. This report investigated the effects of different types of contaminants and impact damage on the ultimate strength and durability of bonded scarf repairs to a laminate substrate.

The objective of this research program was to substantiate the ultimate strength and durability of bonded scarf repairs applied to solid laminates subjected to impact damage and pre-bond contamination.

## 2.2 SPECIMEN CONFIGURATION

Baseline repair data were generated for repair systems that were representative of factory and field repairs. The factory repairs were used as a baseline for the damage tolerance investigation, whereas the field repairs were used as a baseline for the contamination investigation. Variables considered included different substrate moduli, repair materials, scarf ratios, laminate thicknesses, and environmental conditions. The coupon configuration chosen for the study was a 4-inch-wide single scarf joint, as shown in figure 6.

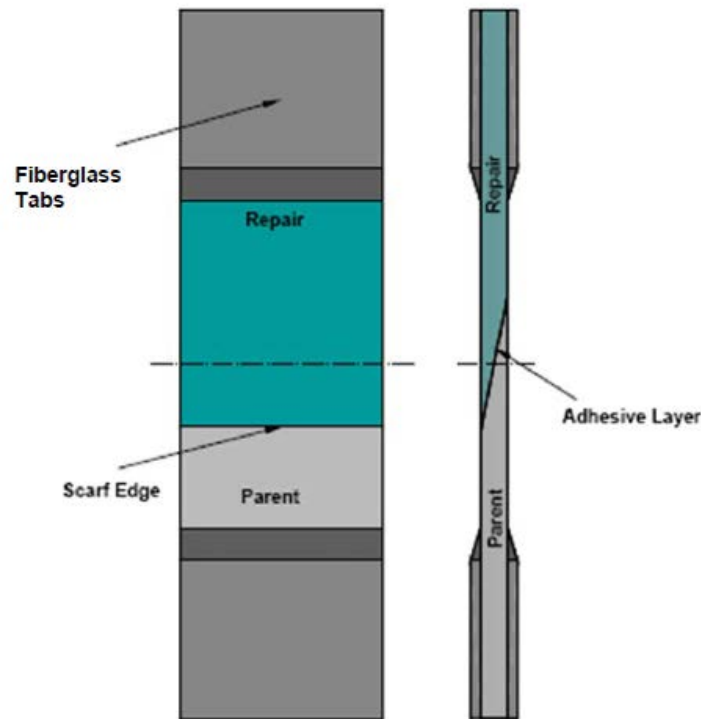


**Figure 6. Repair coupon configuration**

### 2.3 PANEL MANUFACTURING/SUBPANEL MACHINING AND SCARFING

Panels of different thicknesses and substrate moduli were manufactured by the OEM. All parent panels were cured in an autoclave at 350°F at 85 psi. After fabrication, the test panels were inspected using through-transmission ultrasonics (TTU) and pulse echo equipment according to OEM procedures to ensure the manufacturing integrity of the panels and to detect any flaws induced during fabrication. An aluminum oxide grinding wheel with a fixture set to the target scarf angle was used for machining the coupons, as shown in figure 7. All grinding was

conducted using a coolant to avoid ply delamination and to ensure proper dust collection. The scarfed surface prepared for bonding was solvent wiping using acetone. Figure 8 shows scarfed panels ready for repair.



**Figure 7. Repair coupon scarf grinding setup**

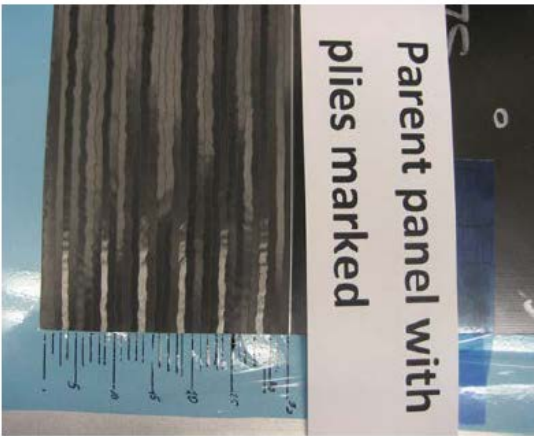


**Figure 8. Machined/scarfed subpanels ready for repair**

#### 2.4 PRE-BOND CONTAMINATION PROCEDURE

Five different contaminants were used for the contamination investigation: (1) JF (JP-8, MIL-T-83133), (2) PS (Methylene Chloride ASTM D4701), (3) Skydrol (SH) (Skydrol LD-4), (4) water, and (5) perspiration (PR). The JF and SH panels were soaked in the contaminants for 30 days, PR (34g/L salt water ASTM D1141 equivalent) was applied to the surface prior to bonding, PS panels were exposed to the contaminant for 6 days, and water panels were exposed to moisture at 85%RH at a temperature of 180°F until moisture equilibrium was achieved. Once 100% moisture equilibrium was achieved (referred to as 100% saturation), panels were subsequently dried to achieve %saturation levels of 75%, 50%, and 25%. Figures 9 and 10 show examples of the contamination procedure for water- and SH-contaminated panels, respectively.



**Figure 9. Water (moisture conditioning) exposure**

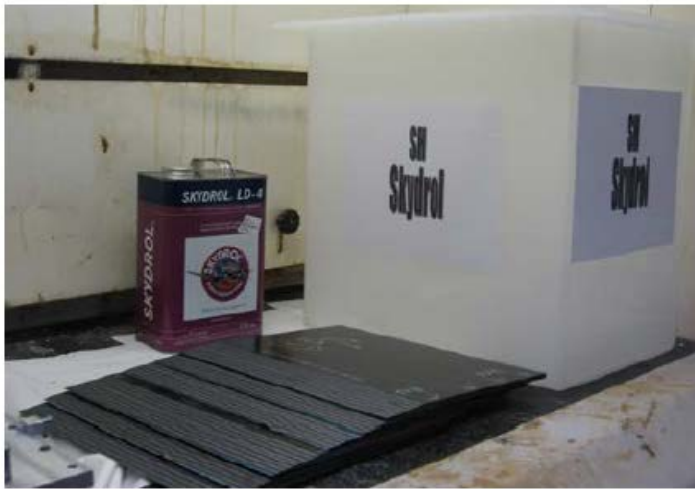


**Figure 10. SH exposure**

## 2.5 OEM REPAIR/DAMAGE TOLERANCE COUPON REPAIR PROCEDURE

All coupons used for the damage tolerance investigation were repaired using the double vacuum debulking (DVD) process. The DVD process was used to consolidate the repair patch prior to bonding it to the cured scarfed parent. Repair plies were assembled so that the repair ply matched the orientation of the parent laminate. The main advantage of the DVD process was that the B-staged, partially cured patch could be cured under vacuum without the use of pressure. The repair patch consolidation was prepared as shown in figure 11. The purpose of the outer bag over the flexible inner bag was to relieve the clamping pressure on the patch caused by the inner bag. The vacuum level in the two chambers could be operated independently. Because the outer chamber was rigid, the net effect on the two vacuum chambers was that no pressure was applied over the patch area, allowing trapped air and volatiles to diffuse out as the resin viscosity decreased. The outer vacuum was then vented to allow full compaction by the inner bag. This method has been shown by the U.S. Navy to produce low porosity patches as compared to a typical single bag [32 and 33].

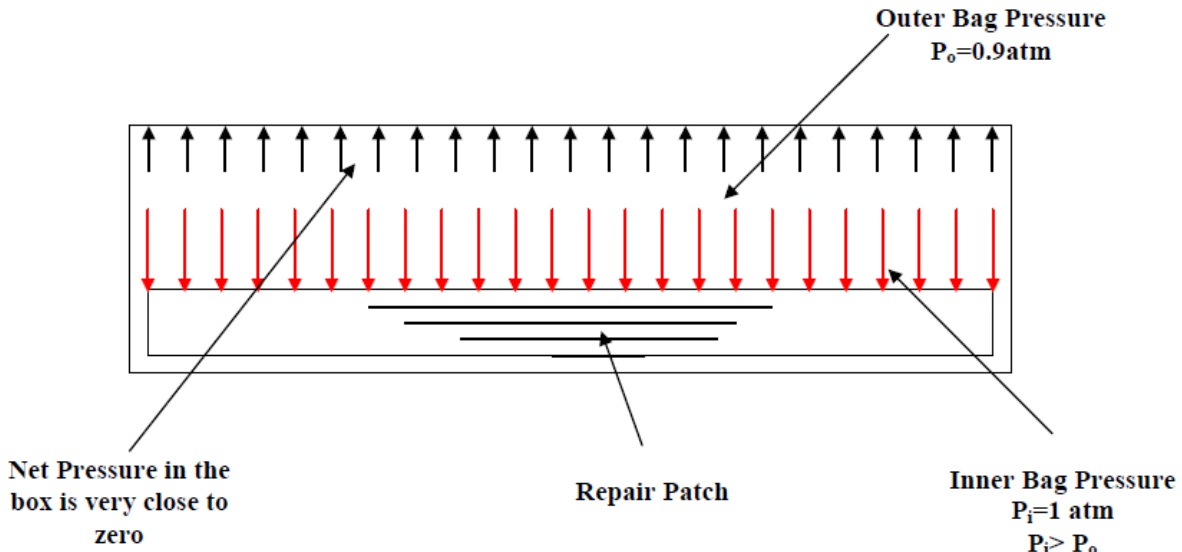


**Figure 11. DVD process diagram**

All repair plies were consolidated in the DVD box at 220°F for 1 hour. The consolidated patch was subsequently bonded to the parent laminate using film adhesive according to the OEM-recommended cure cycle.

## 2.6 FIELD REPAIR/CONTAMINATION COUPON REPAIR PROCEDURE

After exposure to contamination, the scarfed panels were solvent cleaned per the OEM-recommended procedure in preparation for repair. The effects of solvent wiping on the residual contamination were not investigated in this study. The repair procedure is shown in figures 12–17.

### 2.6.1 Tool, Scarfed Panel Preparation

A sheet of non-perforated separator film was secured to the tool using tape. The separator film was secured so that it extended beyond the footprint of the parent panel and the repair, as shown in figure 12. A 1-inch margin was left on each side of the tool near the edge for sealant tape application. The parent panels were then placed on the tool (figure 12) and secured with tape (flashbreaker 1R) to prevent the panels from moving during repair. The panels were then cleaned using acetone applied to a lint-free cloth. It should be noted that the solvent should never be sprayed directly onto the surface, but onto the cloth first and then the wet (solvent) cloth should be used subsequently to clean the surface.

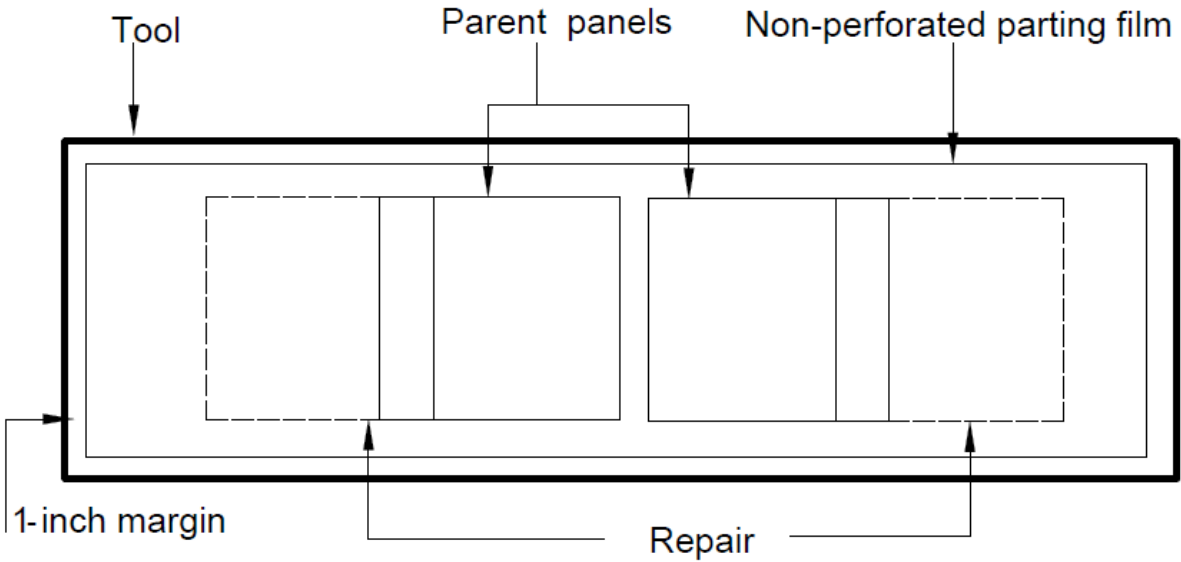


**Figure 12. Scarfed panels cleaned and placed on the repair tool prior to bonding**

### 2.6.2 Repair Ply Marking

Using a black Sharpie® marker, the lines of all plies were extended from the scarf onto the parting film for a length of one inch on both sides of the panel, as shown in figure 13. These markings were used to align the repair plies during the lay-up. The repair kits were taken out of the freezer at least 12 hours prior to use and allowed to reach room temperature prior to repair. Kits were labeled according to the corresponding parent panel identification.

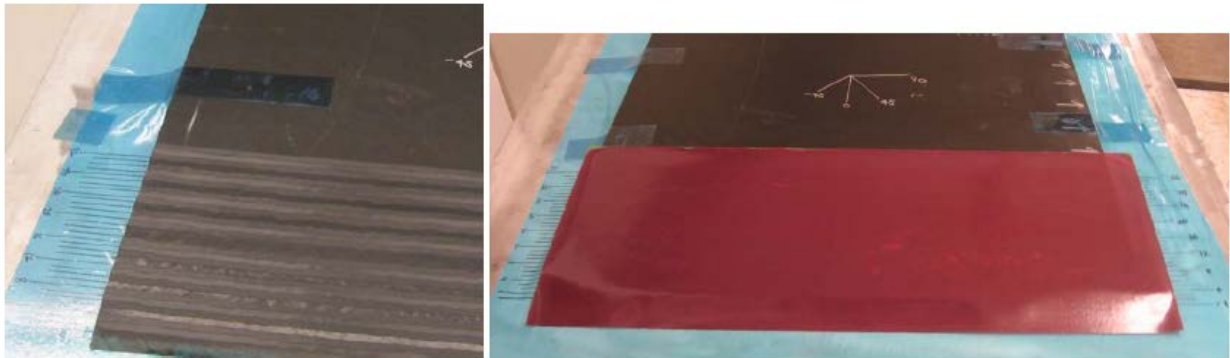


**Figure 13. Ply location markings/adhesive application prior to repair ply application**

### 2.6.3 Adhesive Film Application/Repair Ply Lay-Up

The adhesive backing film was then removed and the adhesive applied onto the scarf region, as shown in figure 13. The repair plies were then carefully aligned using the extended scarf lines previously drawn and laid up following the parent stacking sequence as specified in the repair lay-up sheet, as shown in figures 14 and 15.

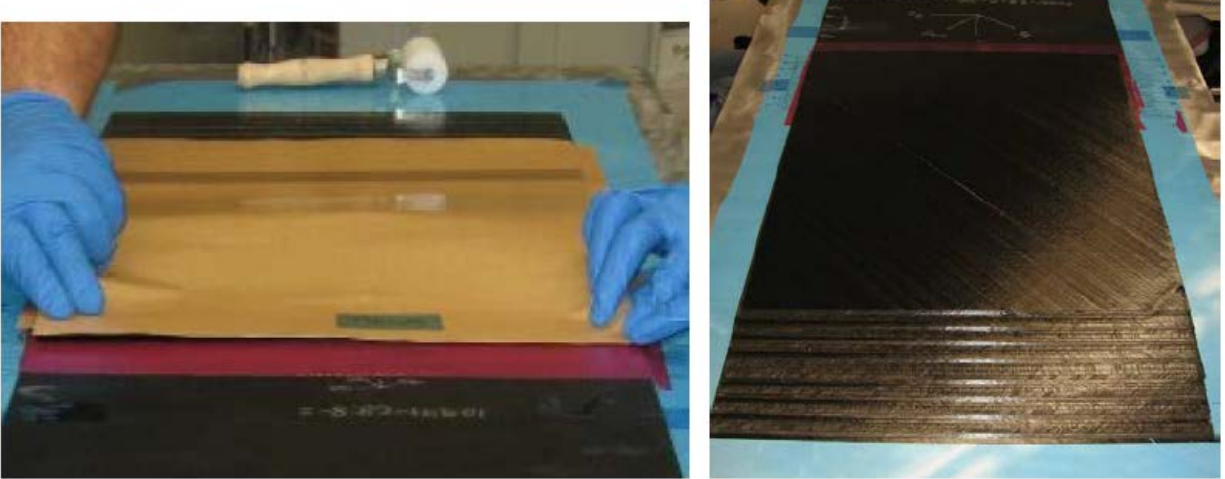


**Figure 14. Individual repair ply lay-up procedure**

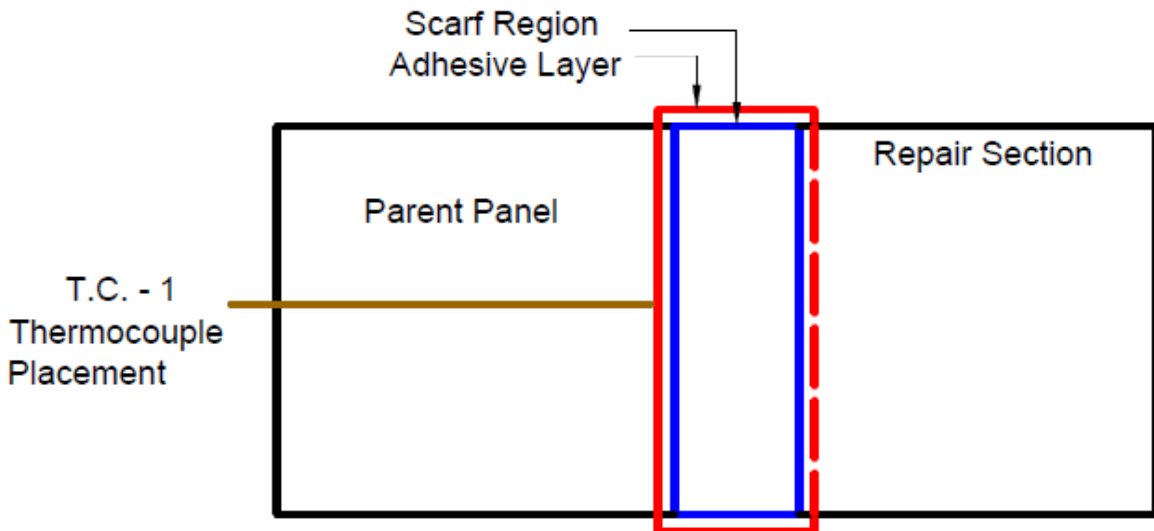


**Figure 15. Thermocouple placement**

#### 2.6.4 Thermocouple Placement

One thermocouple was placed on each repair panel, secured to the tool using tape, and labeled according to figure 15.

#### 2.6.5 Final Bagging

A layer of separator film was placed over the repaired panels and secured with approved tape. Caul plates were placed on the repair panels, as shown in figure 16. The assembly was then bagged, as shown in figure 17, to ensure that no wrinkles were apparent on the bag around the vacuum port or on the repair and that there was no evidence of pinching/squeezing at the edge of the laminates. A vacuum leak was then performed to ensure that the maximum vacuum loss did not exceed 2" Hg in 5 minutes.

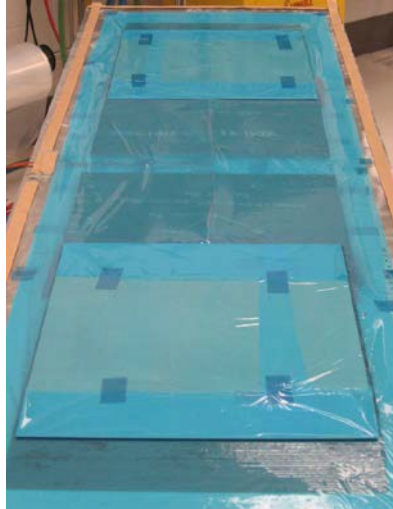


**Figure 16. Caul sheet placement/repair panels ready for bagging**

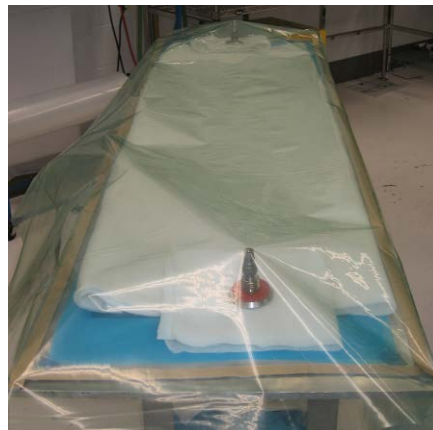


**Figure 17. Repair panel bagging procedure**

NDI using TTU was conducted on the repaired panels and showed variability in the repaired laminates with the porosity/consolidation levels, as shown in figures 18–22.

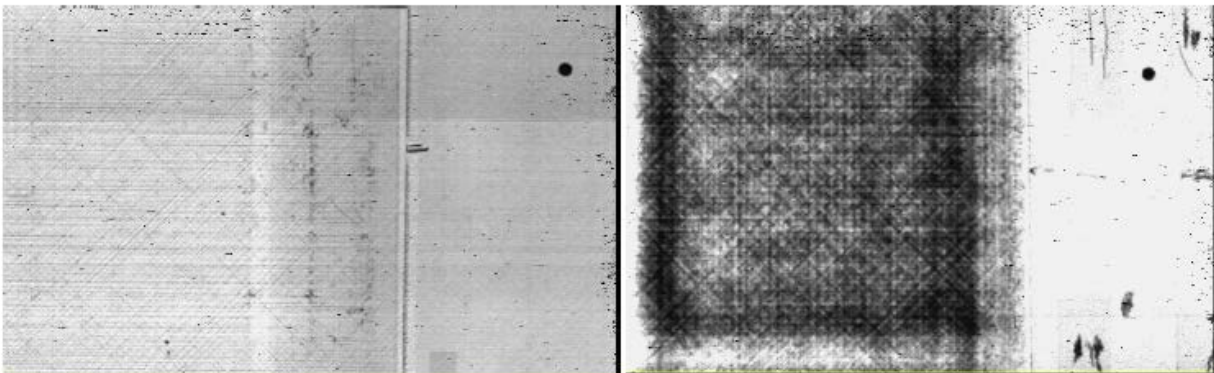


**Figure 18. Representative c-scans of panels contaminated with JF prior to repair**

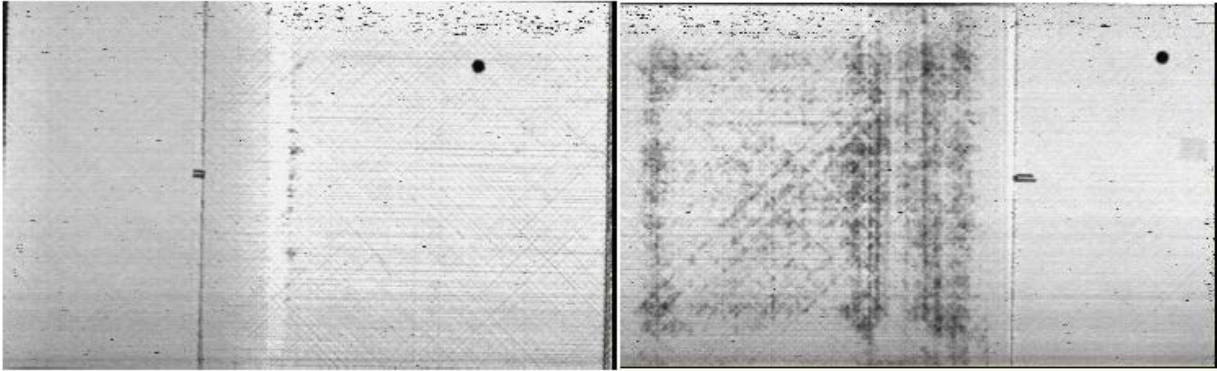


**Figure 19. Representative c-scans of panels exposed to PR prior to repair**

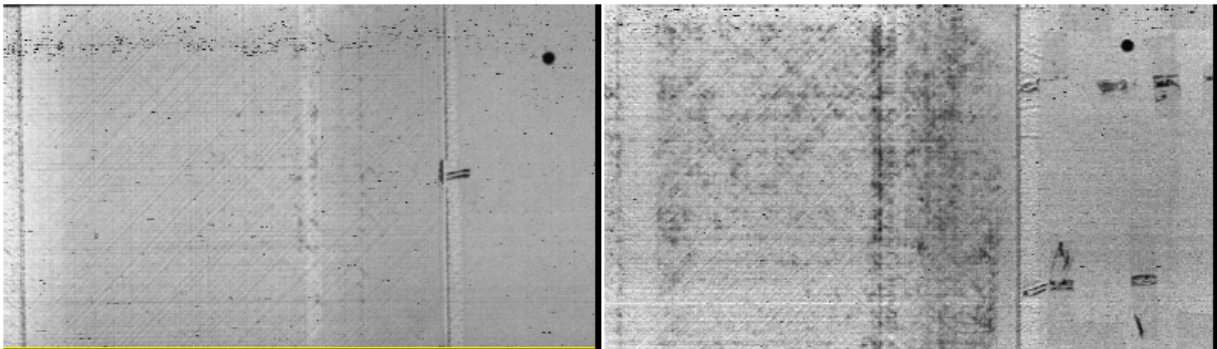


**Figure 20. Representative c-scans of panels exposed to PS (methylene chloride) prior to repair**

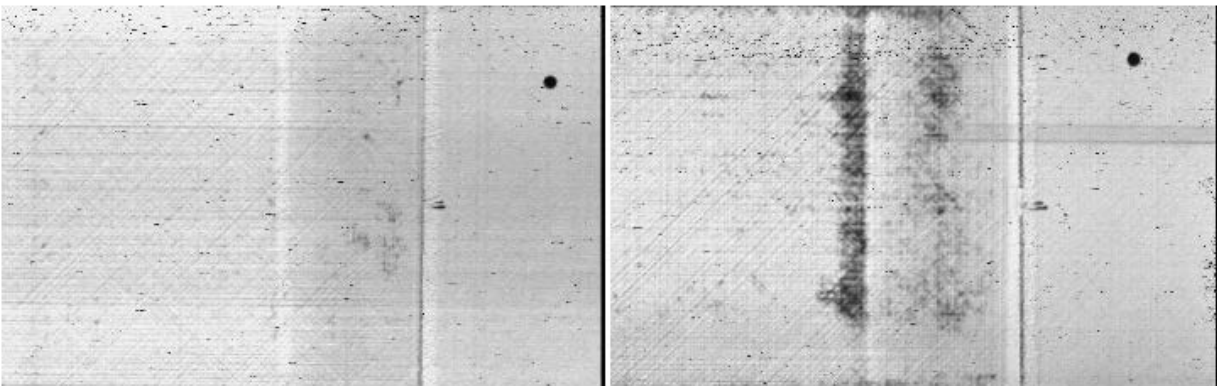


**Figure 21. Representative c-scans of panels exposed to SH prior to repair**

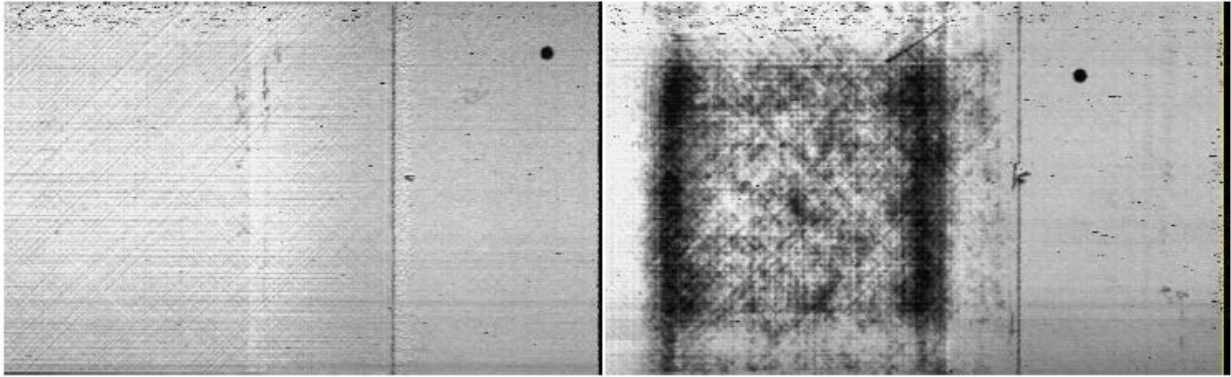


**Figure 22. Representative c-scans of panels exposed to water prior to repair**

## 2.7 IMPACT PROCEDURE

An Instron<sup>®</sup> Dynatup<sup>®</sup> 8250 Drop Weight Impact Tester, configured with a 5000-lb piezoelectric load cell and a 1.2" diameter impactor, was used to inflict the damage on the repair coupons, as shown in figure 23. The test machine consisted of a frame, two guide columns, a hoist motor, a drop weight mechanism, a control pendant, and accessories. The machine can be operated in gravity-assisted or pneumatic mode. In gravity-assisted mode, the maximum velocity that can be achieved is 12.7 ft/sec, whereas in pneumatic modes, velocities up to 44 ft/sec can be achieved. The test machine has variable impactor weights: 5.5, 10, 25, 50, 75 and 100 lbs, as well as variable impactor end geometries and a maximum drop height of 46" to accommodate different specimen tup selections and specimen thicknesses. In gravity-assisted mode, a maximum impact energy of 223 ft-lb can be achieved, whereas in pneumatic mode, a maximum impact energy of 326 ft-lb can be achieved.



**Figure 23. Instron Dynatup**

All 18-ply and 48-ply repair specimens were impacted at different locations in the repair scarf region, as shown in figures 24–26. Three different impact sites were considered: (1) at the tip of the scarf from the far side (TF), (2) at the tip of the scarf from the near side (TN), and (3) at the scarf center (CN). The intent was to investigate the potential differences in residual strength resulting from different impact sites.

Several iterations were conducted to determine the energy level that would result in a dent depth of 0.01" on both the 18-ply and 48-ply specimens. An impact energy of 200 in-lb was used for the 18-ply specimens and 400 in-lb was used for the 48-ply specimens. This corresponds to energy levels of approximately 1390 in-lb/in for the 18-ply specimens and 1080 in-lb/in for the 48-ply specimens. Damage was inflicted at the panel level using a 4" x 6" test section. The impact velocity was maintained at a nominal value of 103 in/sec, which corresponds to a drop height of 14" for the 18-ply repaired laminates. For the 48-ply repaired laminates, the impact velocity was maintained at a nominal value of 140 in/sec, which corresponds to a drop height of 26". All repaired panels were inspected using TTU and were subsequently tabbed prior to machining and testing.

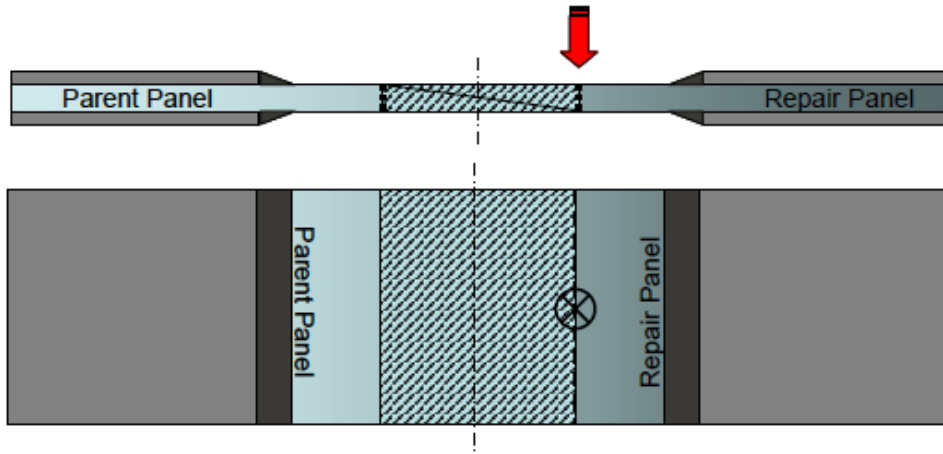


**Figure 24. Damage site for the impact specimens TF (tip far)**

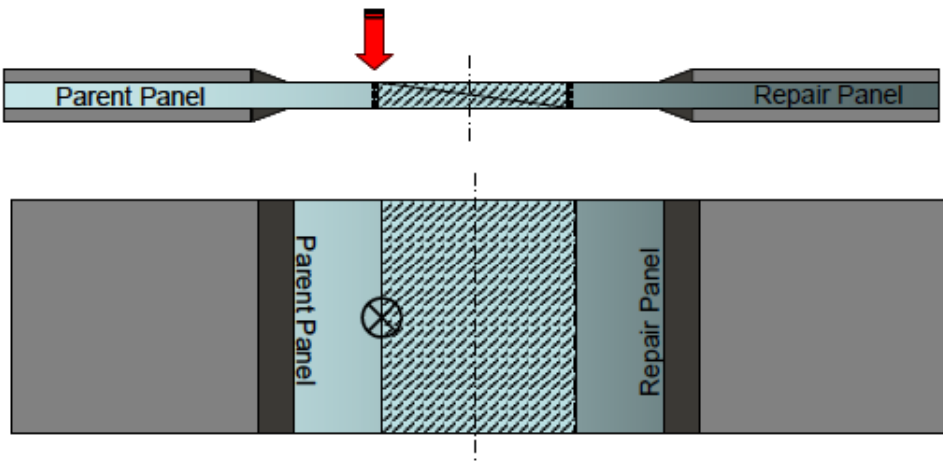


**Figure 25. Damage site for the impact specimens TN (tip near)**

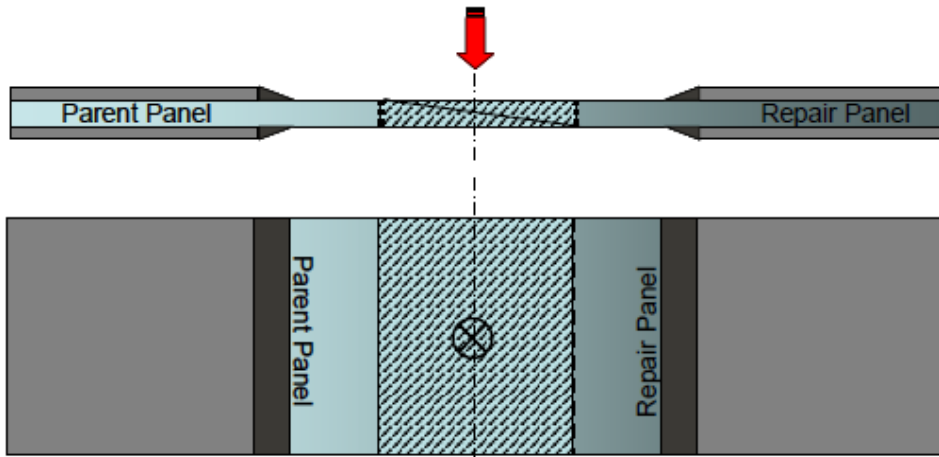


**Figure 26. Damage site for the impact specimens CN (center)**

Typical force time histories and force displacement curves for 18-ply and 48-ply specimens are shown in figures 27–36.

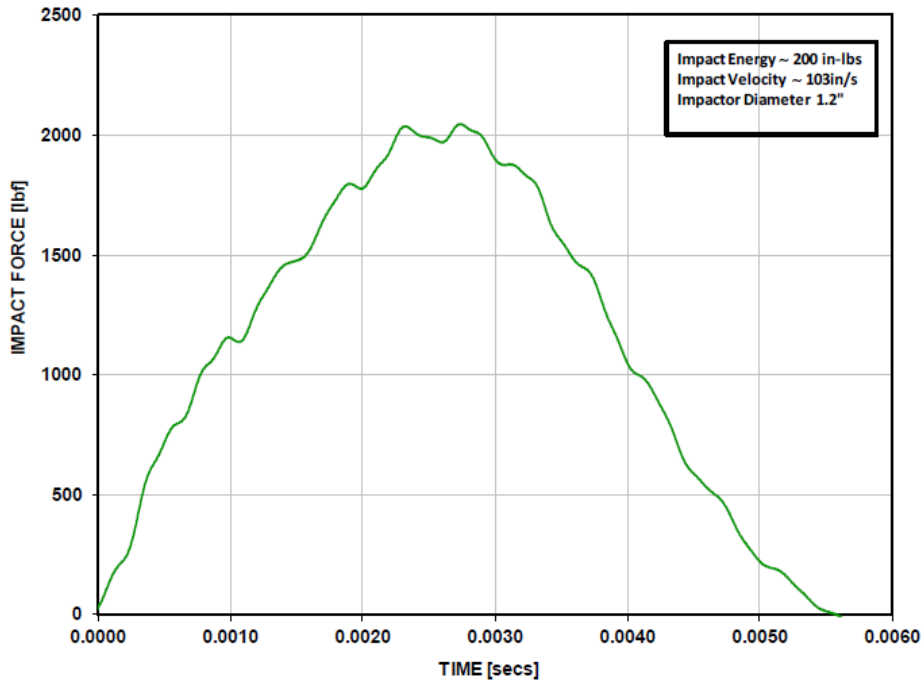


**Figure 27. Typical force time history for 18-E1-10-TF laminates**

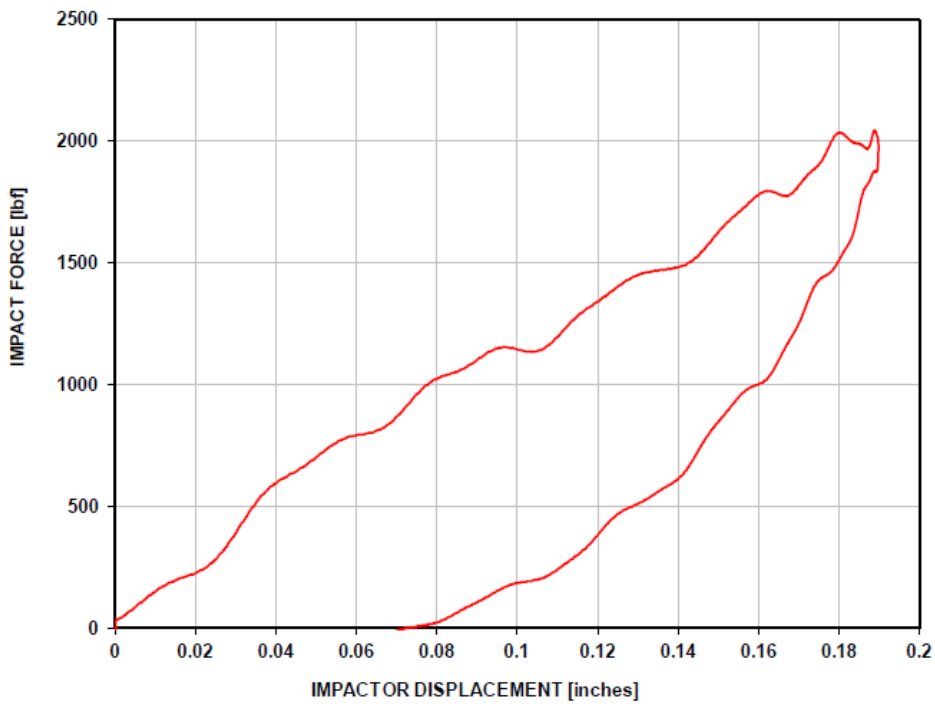


**Figure 28. Typical force displacement curve for 18-E1-10-TF laminates**

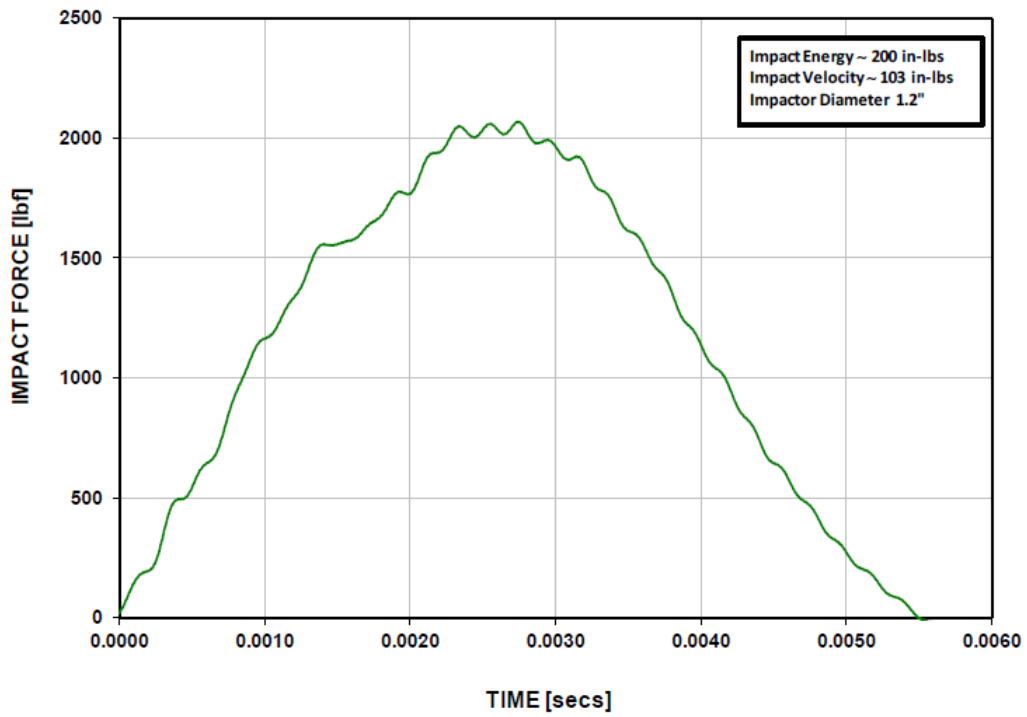


**Figure 29. Typical force time history for 18-E2-20-TF laminates**

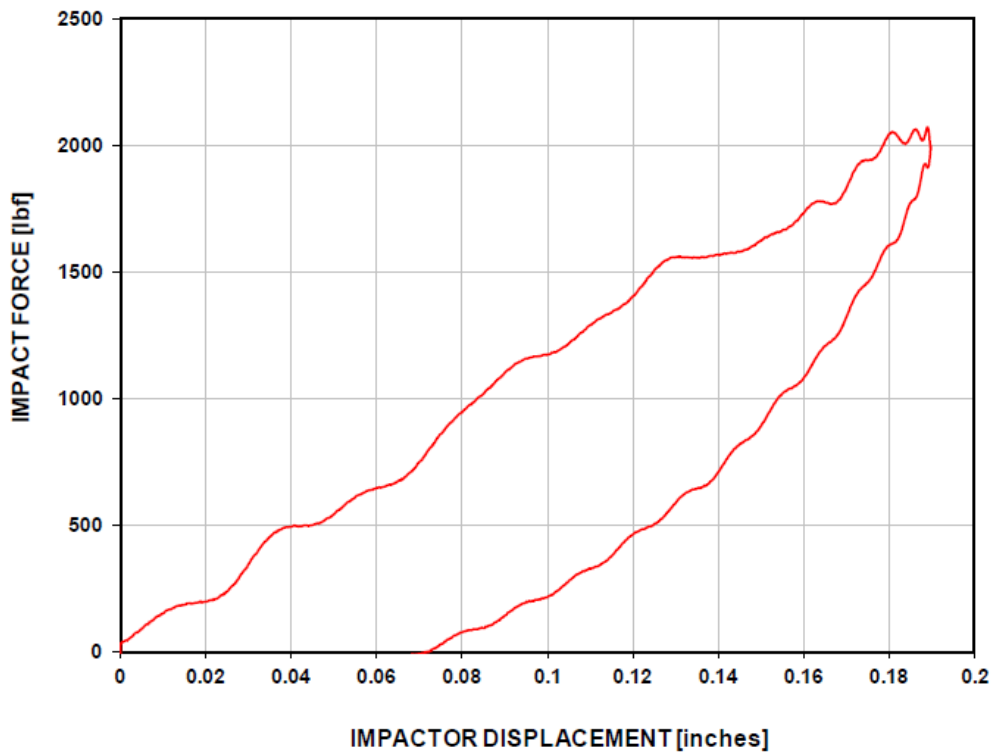


**Figure 30. Typical force displacement curve for 18-E2-20-TF laminates**

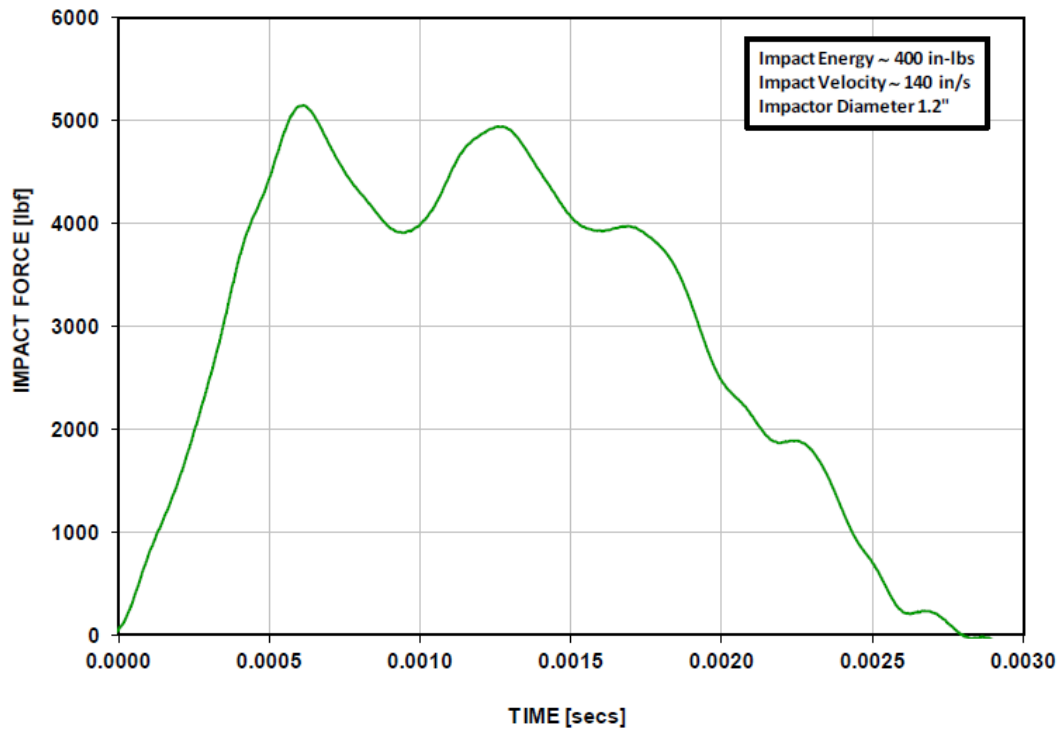


**Figure 31. Typical force time history for 48-E1-10-CN laminates**

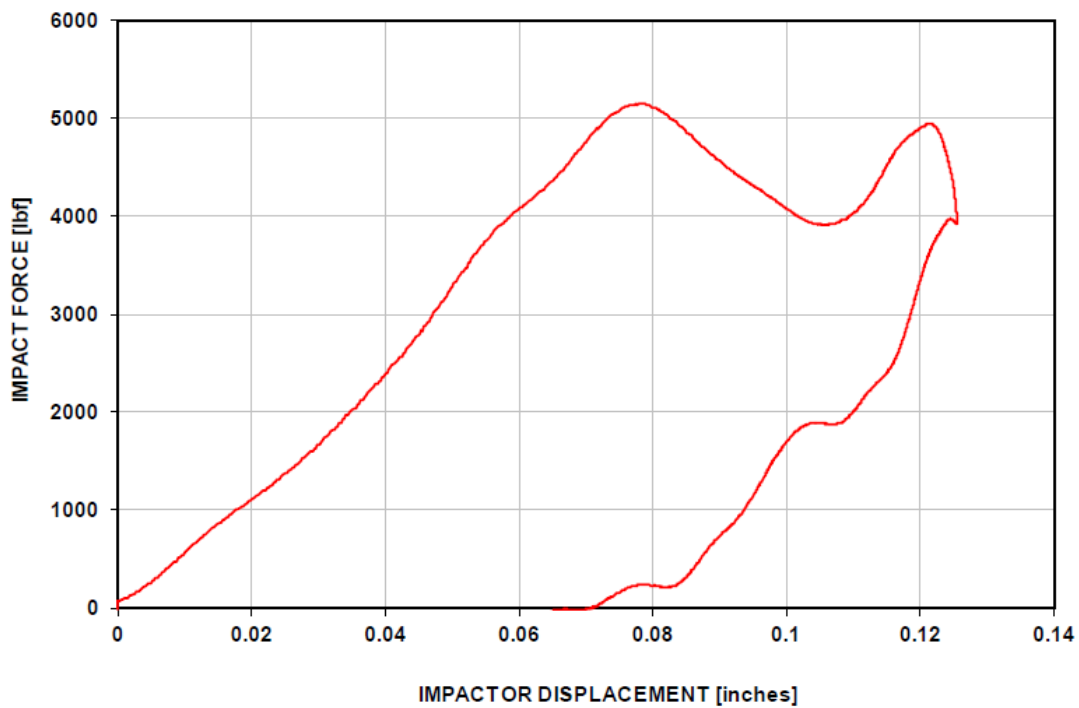


**Figure 32. Typical force displacement curve for 48-E1-10-CN laminates**

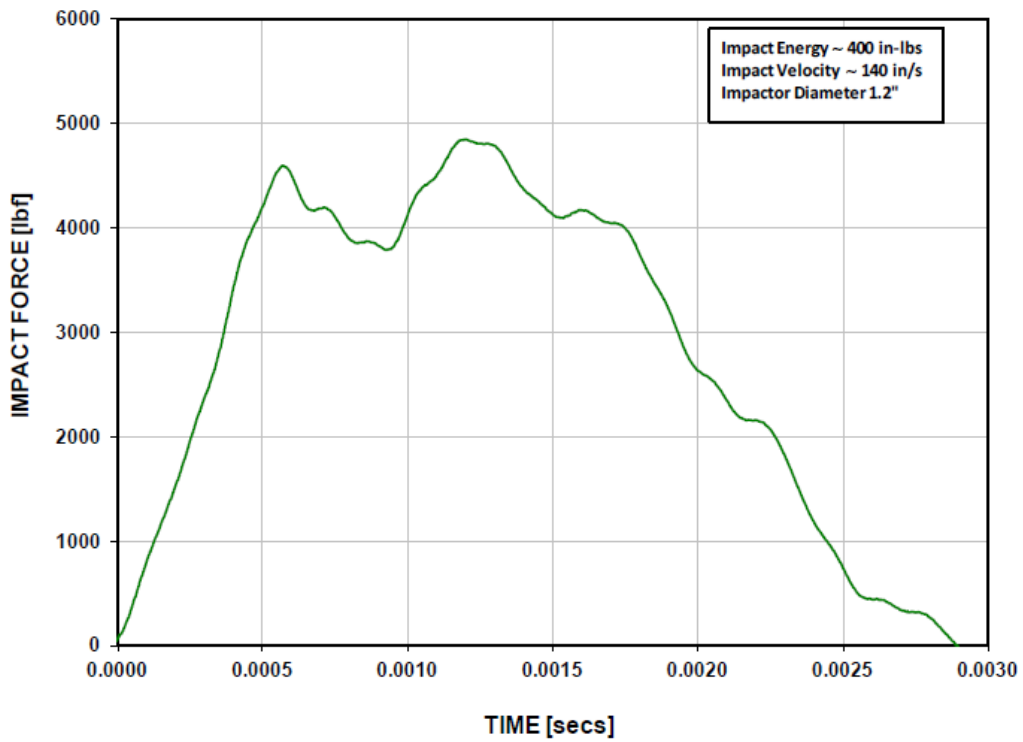


**Figure 33. Typical force time history for 48-E1-20-TF laminates**

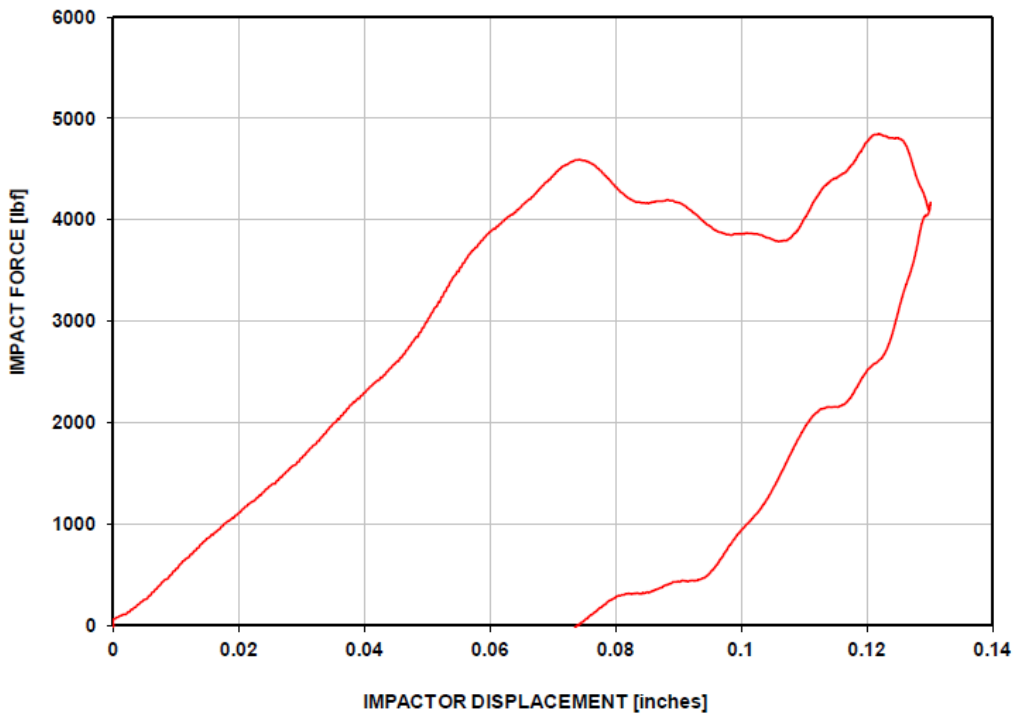


**Figure 34. Typical force displacement curve for 48-E1-20-TF laminates**

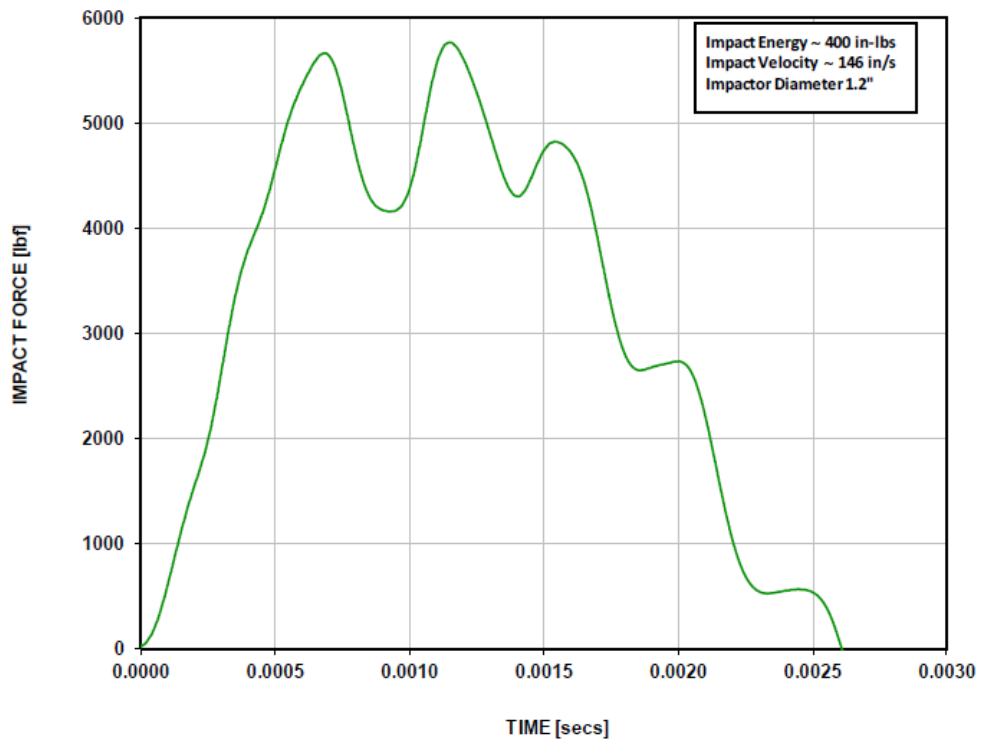


Figure 35. Typical force time history for 48-E2-20-TN laminates

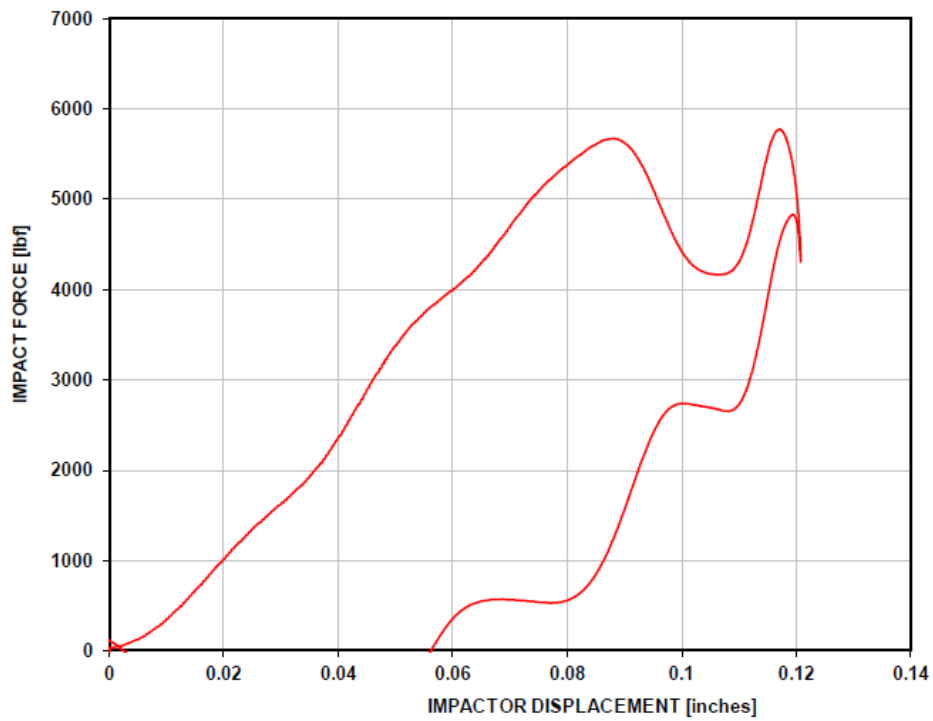
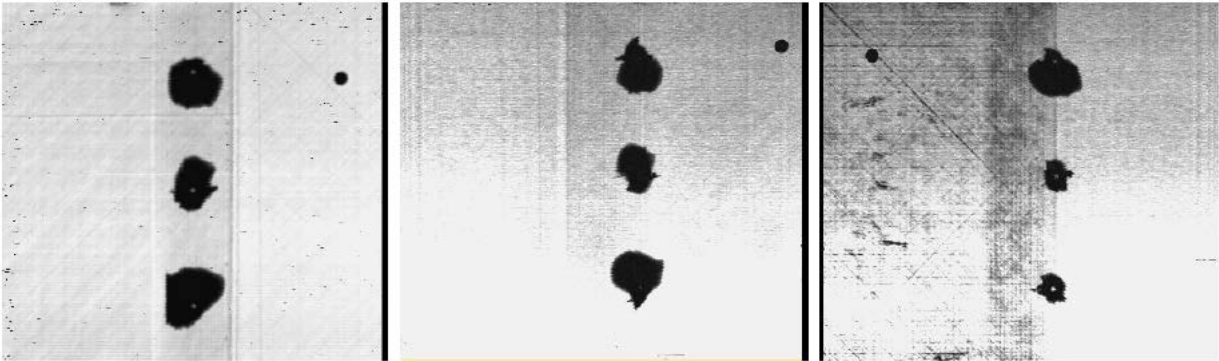
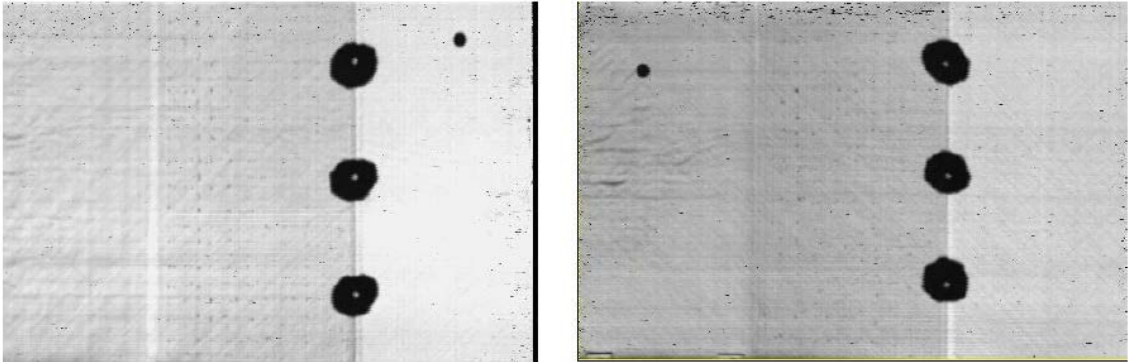


Figure 36. Typical force displacement curve for 48-E2-20-TF laminates

Figures 37–40 show typical C-Scans of the repaired panels prior to machining them into individual specimens. It should be noted that the variability in the planar damage area resulted from varying impact sites.



**Figure 37. C-Scans of 18-E1-20-CN-RTF/18-E1-20-TF-RTF/18-E1-20-TN-RTA panels**



**Figure 38. C-Scans of 48-E2-20-TN-RTA/48-E2-20-TN-RTF panels**

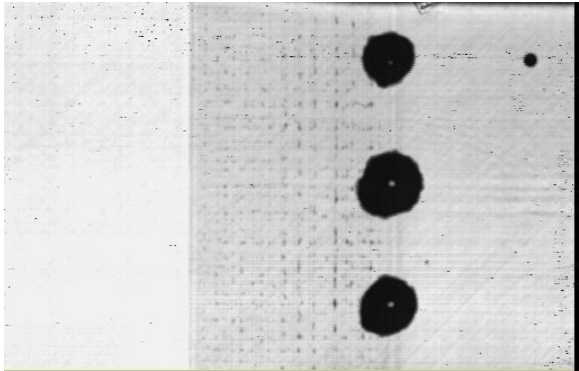


**Figure 39. C-Scan of 48-E2-20-TF-RTF panel**

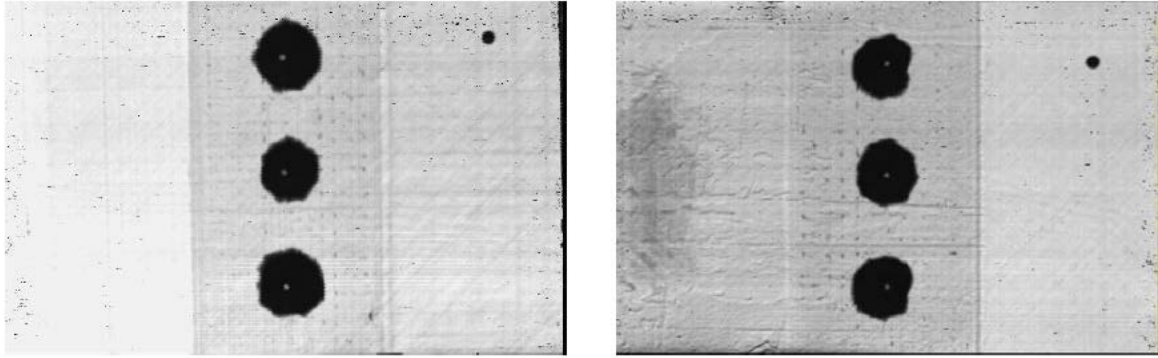


**Figure 40. C-Scans of 48-E2-20-CN-RTA/48-E2-20-CN-RTF panels**

## 2.8 MOISTURE EQUILIBRIUM/MOISTURE ABSORPTION/DESORPTION CYCLES

All wet conditioned samples were exposed to elevated temperature and humidity conditions to establish moisture equilibrium of the material. Specimens were exposed to  $85\% \pm 5\%$  relative humidity and  $180^{\circ}\text{F} \pm 5^{\circ}\text{F}$  until an equilibrium moisture weight gain of traveler or witness coupons was achieved. ASTM D5229 procedure C was used as a guideline for environmental conditioning and moisture absorption.

Effective moisture equilibrium was achieved when the average moisture content of the traveler specimen changed by less than 0.02% for two consecutive readings within a span of  $7 \pm 0.5$  days and was expressed by:

$$\frac{W_i - W_{i-1}}{W_b} < 0.02\% \quad (3)$$

where,

$W_i$  = weight at current time

$W_{i-1}$  = weight at previous time

$W_b$  = baseline weight prior to conditioning

Once the traveler coupons passed the criteria for two consecutive readings, the samples were removed from the environmental chamber and kept in a sealed bag until they were ready for mechanical testing.

For the samples exposed to water (water contaminated samples)—referred to as WA0, WA25, WA50, and WA75—moisture equilibrium was achieved by exposing these samples to  $85\% \pm 5\%$  relative humidity and  $180^{\circ}\text{F} \pm 5^{\circ}\text{F}$  until equilibrium moisture gain was achieved ( $\sim 1\%$  total percent moisture weight gain referred to as 100% moisture equilibrium). These samples were then dried to achieve  $\sim 0.75\%$ ,  $0.5\%$ ,  $0.25\%$  moisture weight percent referred to as 75%, 50%, and 25% moisture equilibrium, shown in figure 41. Once the desired moisture levels were achieved, the samples were removed from the chamber and repaired as per the procedure specified in section 2.5.

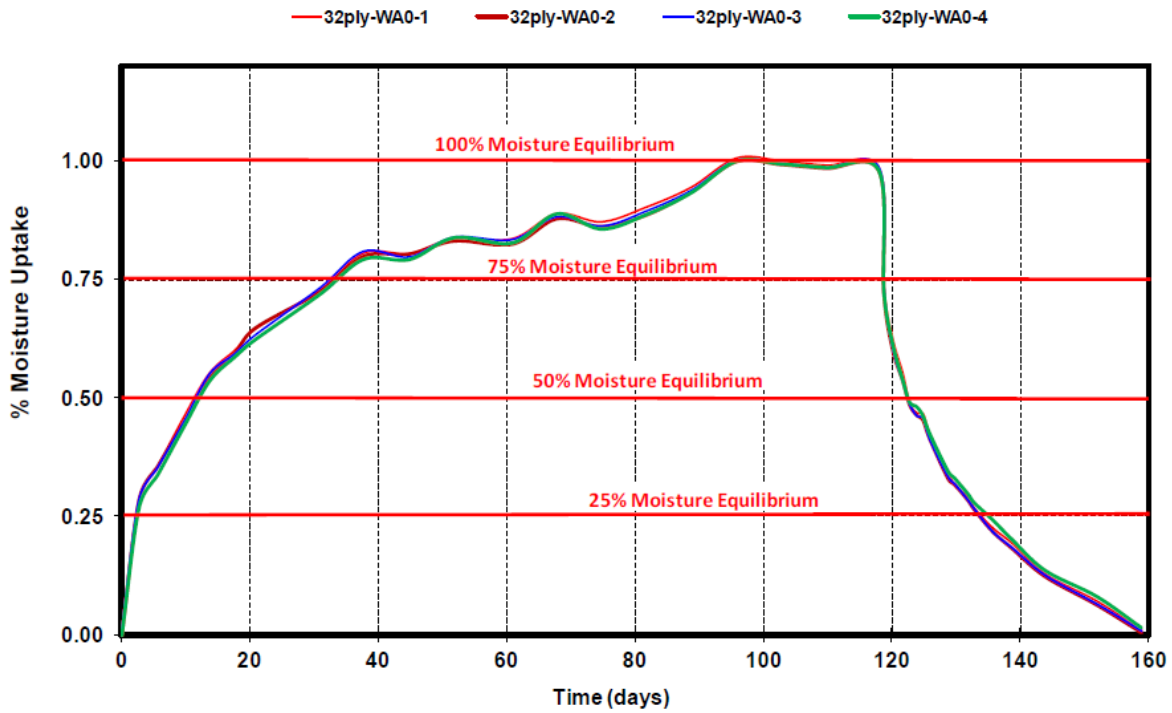


**Figure 41. Moisture absorption/desorption cycle for 32-ply laminates (parent material)**

## 2.9 MECHANICAL TESTING

Several MTS/Instron servo-hydraulic machines (55 kip and 110 kip) were used for loading the repaired laminate coupons. Figure 42 shows the laminate repair test setup. All static tests were conducted under displacement control at a rate of 0.05 in/min to induce specimen failure within 6 minutes. The tests were controlled using the MTS Teststar IIm control system and MTS Multi-Purpose Testware computer software or Instron control systems with National Instruments Labview data acquisition system. Coupons were tested at room temperature ambient static (RTA). Strain data were collected using strain gages (CEA-06-250UN-120) for all conditions per the layout shown in figure 43. For room temperature testing, in addition to strain gages, the photogrammetry system was used to map strain distributions within the specimens, as shown in figure 42. All specimens were checked for dimensional and machining integrity prior to testing. Measurements documented included specimen thickness, length, and width. Data documented during the tests included test rate, specimen load, actuator displacement, and strain data.



The ARAMIS system, shown in figure 42, is a non-contact, three-dimensional digital correlation measuring system that uses a pair of very high-resolution cameras arranged to form an angle of 20° to 60° with respect to the object of interest to monitor strain concentrations in a test article. A random pattern is applied to the surface of the structure prior to loading. This pattern consists of a combination of light and dark areas with a 50:50 ratio. The pattern should show a distinct contrast with respect to the surface so that matching of the pixels in the image can be performed correctly. The size of the pattern should be small enough to allow the use of a fine grid of facets and large enough to solve the project in a reasonable amount of time.

The sensor is calibrated before taking measurements. Different calibration panels with varying sizes from 10 x 8 mm<sup>2</sup> to 1200 x 960 mm<sup>2</sup> are available. Different parameters defining the size and type of lenses and also the size of the calibration panel are entered prior to performing the calibration process. The calibration object is then positioned the same distance from both cameras, so that the angle formed at the intersection of the calibration panel is between 20° and 60°. First, a picture of the calibration object is taken at different angles and distances from the cameras. Then, the software analyzes the views from both cameras and ensures that every point in the left view is found in the right view, within a certain tolerance.

Once the calibration is completed correctly, the structural test is ready to be carried out. The test coupon is placed at the exact same distance as the calibration panel. A reference picture is taken prior to loading. The ARAMIS system assigns reference coordinates to every pixel in the image. Pictures of the structure are recorded at different load levels. The ARAMIS system compares every picture to the previous one and registers any changes in the displacements and rotations. Given the displacements' and rotations' values, strains can be calculated. ARAMIS provides a variety of ways for post-processing the data (e.g., two-dimensional or three-dimensional maps of the displacements, strains, and stresses displayed as a function of spatial position, or both). Section plots can also be obtained showing the distribution of displacements, stresses, or strains in a particular section of the test coupon. Therefore, regions with high-stress concentrations can be identified and thoroughly characterized.

All fatigue tests, which was denoted RTF, were conducted under room temperature ambient condition at constant amplitude load control with a 2-Hz frequency. All fatigue coupons were subjected to 165,000 cycles at a constant predetermined far-field strain and tested for residual strength after cyclic loading if no fatigue failures occurred.

### 3. DAMAGE TOLERANCE INVESTIGATION RESULTS

All testing conducted for the purpose of the repair damage tolerance investigation was performed according to the test matrix outlined in table 1. A total of 144 static and cyclic specimens was used for the investigation. Variables investigated included two different scarf rates (1:10 and 1:20), two different thicknesses (18-ply and 48-ply panels), and two different substrate moduli (E1 and E2), in which E1 is a quasi-isotropic lay-up (25/50/25 or equivalent) and E2 is a stiffer lay-up (with 33% of 0 degree plies). The 1:20 scarf repairs have a 28 in<sup>2</sup> scarf bond area whereas the 1:10 scarf repairs have a 14 in<sup>2</sup> scarf bond area (or half the bond area). All testing was conducted at RTA.

**Table 1. Damage tolerance test matrix**

Plies	Modulus	Scarf Rate	Test Condition	Impact Site		
				TN	TF	CN
18	E1	10	RTA	3	3	3
			RTF	3	3	3
		20	RTA	3	3	3
			RTF	3	3	3
	E2	10	RTA	3	3	3
			RTF	3	3	3
		20	RTA	3	3	3
			RTF	3	3	3
48	E1	10	RTA	3	3	3
			RTF	3	3	3
		20	RTA	3	3	3
			RTF	3	3	3
	E2	10	RTA	3	3	3
			RTF	3	3	3
		20	RTA	3	3	3
			RTF	3	3	3

### 3.1 18-PLY REPAIR LAMINATE DAMAGE TOLERANCE RESULTS

Figure 44 shows a summary of C-Scan damage areas for all 18-ply scarf repairs after impacts. Figures 45–56 are representative C-Scan images obtained for all specimens subsequently tested at room temperature. If one disregards the high scatter for all 18-ply-E1 substrate specimens, the same energy level inflicted at different sites in the repair yielded comparable average planar damage areas for all 1:10 specimens (figure 44). A close examination of the C-scans shows a large scatter in the damage areas obtained for identical samples impacted with the same energy level. The corresponding damage areas represent 41%, 39%, and 43% of the joint overlap area for the 18-ply-E1-10-TN, 18-ply-E1-10-TF, and 18-ply-E1-10-CN configurations, respectively.

For all 18-ply-E1-20 substrate specimens, increasing damage size was observed for the TN, TF, and CN configurations, with the center impacts yielding the most severe damage. For the 1:20 configurations, the average damage areas correspond to 15%, 17%, and 19% of the joint area for the 18-ply-E1-20-TN, 18-ply-E1-20-TF, and 18-ply-E1-20-CN configurations, respectively. Comparing the 1:10 and 1:20 configurations with the same substrate E1, figure 44 shows that the larger repairs (i.e., 1:20 configurations) was less damaged under the same energy level applied.

For all 18-ply-E2 substrate specimens considered, regardless of scarf ratio, the TN impacts yielded the smallest damage areas, followed by the TF impacts and the CN impacts. The same energy level inflicted at different sites in the repair yielded different damage sizes with the

impacts inflicted at the CN being the most severe. Comparing the 1:10 configurations to the 1:20 configurations for the same substrate (18-ply-E2), the data show that the same energy level inflicted on the same location in two joints of different sizes yielded a smaller damage area for the larger repair. The damage areas for the 1:10 configurations correspond to 13%, 32%, and 37% of the joint area for 18-ply-E2-10-TN, 18-ply-E2-10-TF, and 18-ply-E2-10-CN, respectively. For the 1:20 configurations, the damage areas correspond to 6%, 13%, and 15% of the joint area for 18-ply-E2-20-TN, 18-ply-E2-20-TF, and 18-ply-E2-20-CN, respectively. Based on the impact data generated for the 18-ply repaired laminates, it can be concluded that for the substrate and repair systems under investigation with the corresponding configurations, the larger repairs (1:20) appeared to be more damage tolerant than the smaller repairs (1:10).

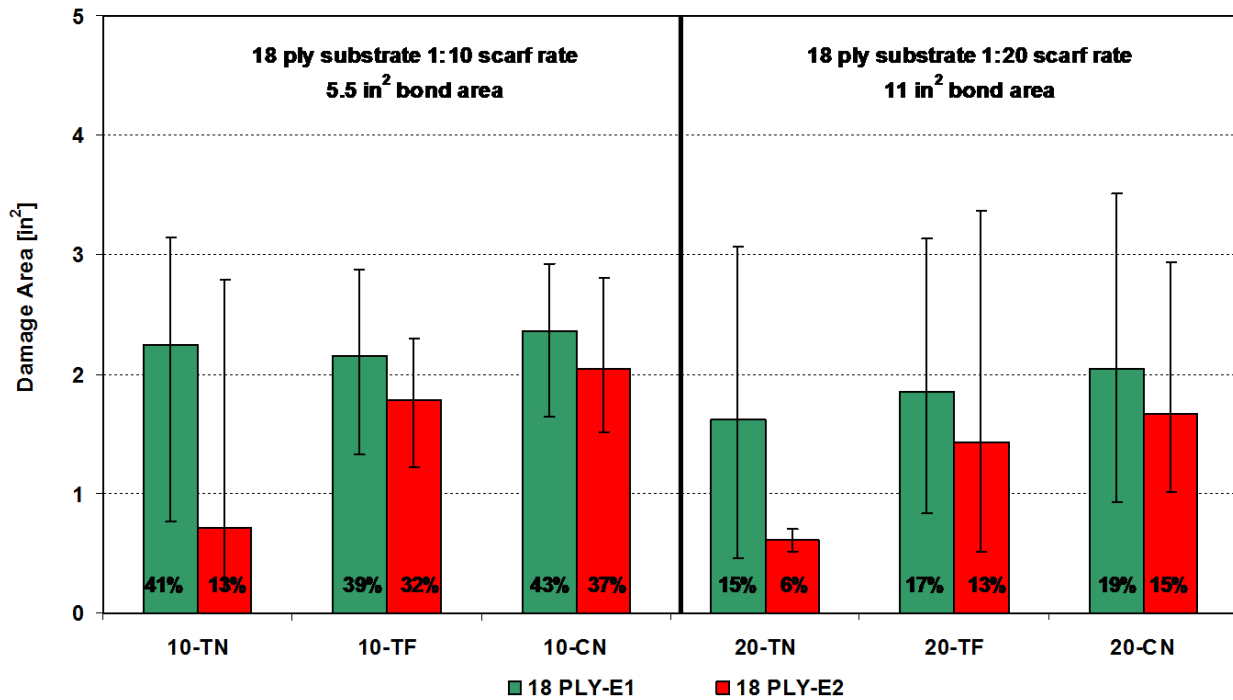
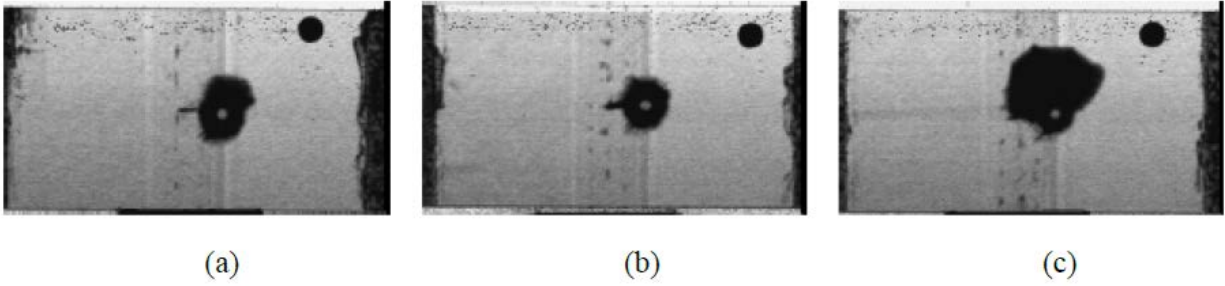
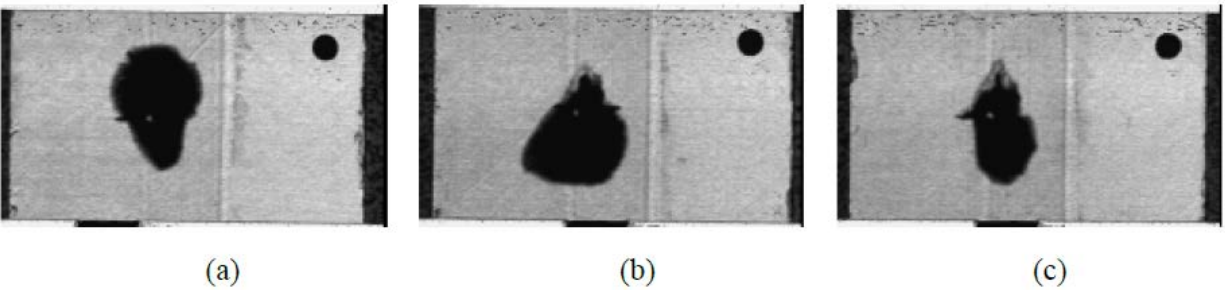


Figure 44. Impact data summary for all 18-ply scarf repair specimens



**Figure 45. C-Scans of 18-ply-E1-10-TN-RTA of damage area and depth, respectively: (a) 1.22 in<sup>2</sup>, 0.006 in; (b) 0.94 in<sup>2</sup>, 0.007 in; (c) 2.61 in<sup>2</sup>, 0.006 in**



**Figure 46. C-Scans of 18-E1-10-TF-RTA-(1, 2, 3) of damage area and depth, respectively: (a) 2.51 in<sup>2</sup>, 0.0085 in; (b) 2.12 in<sup>2</sup>, 0.01 in; (c) 1.32 in<sup>2</sup>, 0.0105 in**

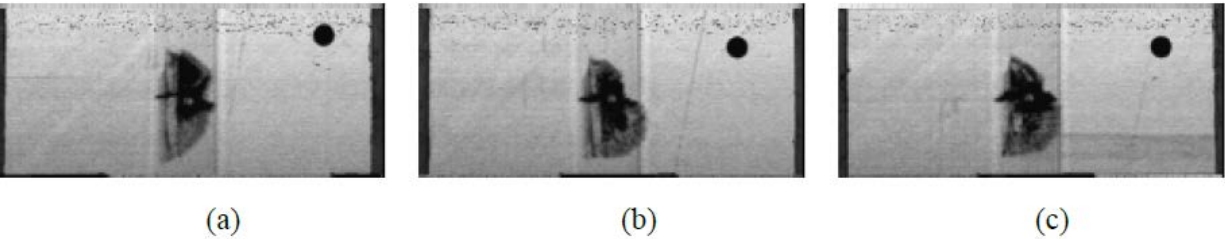


**Figure 47. C-Scans of 18-E1-10-CN-RTA-(1, 2, 3) of damage area and depth, respectively: (a) 1.07 in<sup>2</sup>, 0.0061 in; (b) 1.17 in<sup>2</sup>, 0.006 in; (c) 1.23 in<sup>2</sup>, 0.0065 in**

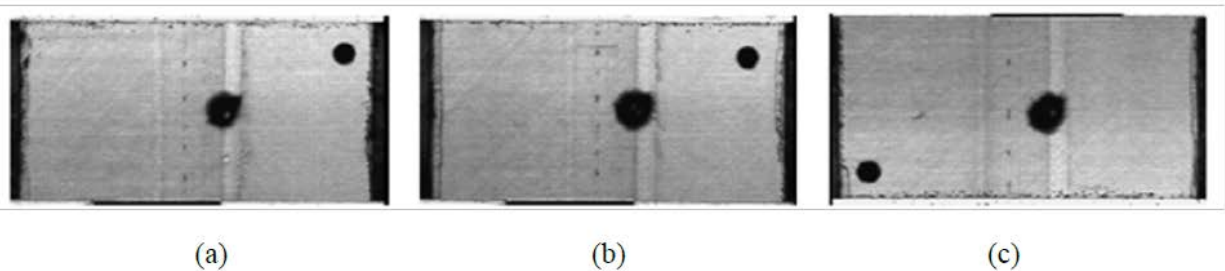


**Figure 48. C-Scans of 18-E2-10-TN-RTA-(1, 2, 3); damage area and depth, respectively: (a) 0.51 in<sup>2</sup>, 0.007 in; (b) 0.66 in<sup>2</sup>, 0.0065 in; (c) 0.62 in<sup>2</sup>, 0.0085 in**

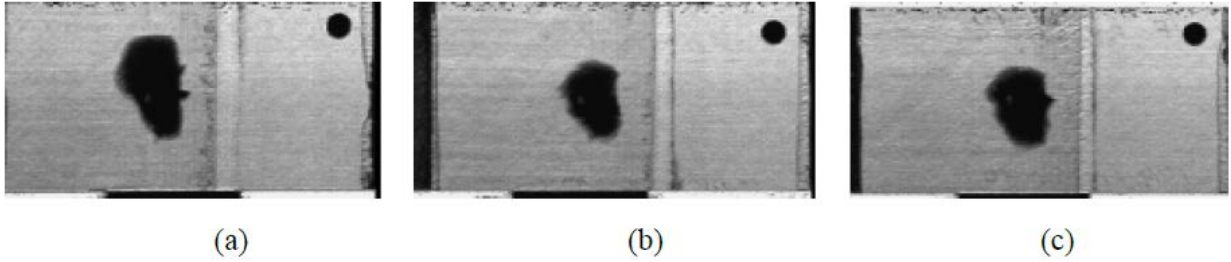


**Figure 49. C-Scans of 18-E2-10-TF-RTA-(1, 2, 3) of damage area and depth, respectively:  
 (a) 2.30 in<sup>2</sup>, 0.0075 in; (b) 1.49 in<sup>2</sup>, 0.0075 in; (c) 1.84 in<sup>2</sup>, 0.008 in**

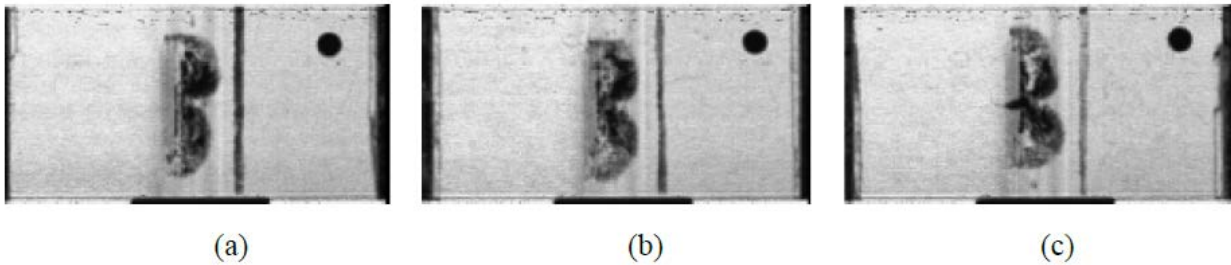


**Figure 50. C-Scans of 18-E2-10-CN-RTA-(1, 2, 3) of damage area and depth, respectively:  
 (a) 1.54 in<sup>2</sup>, 0.0095 in; (b) 1.57 in<sup>2</sup>, 0.004 in; (c) 1.60 in<sup>2</sup>, 0.0055 in**

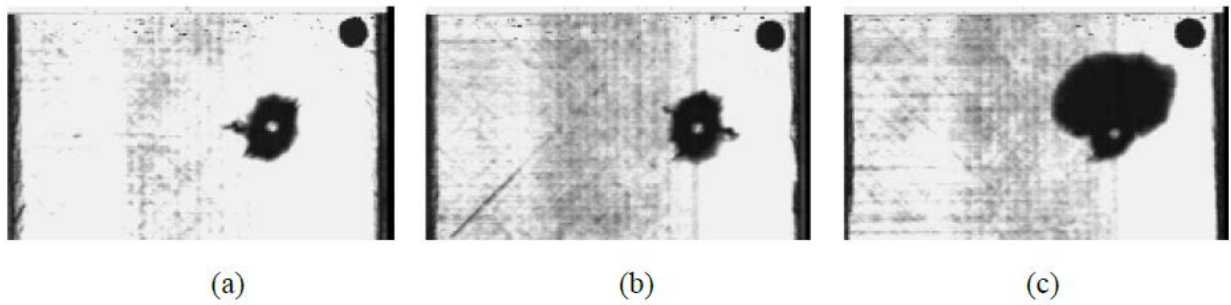


**Figure 51. C-Scans of 18-E1-20-TN-RTA-(1, 2, 3) of damage area and depth, respectively:  
 (a) 0.73 in<sup>2</sup>, 0.0065 in; (b) 0.82 in<sup>2</sup>, 0.0065 in; (c) 2.56 in<sup>2</sup>, 0.0075 in**

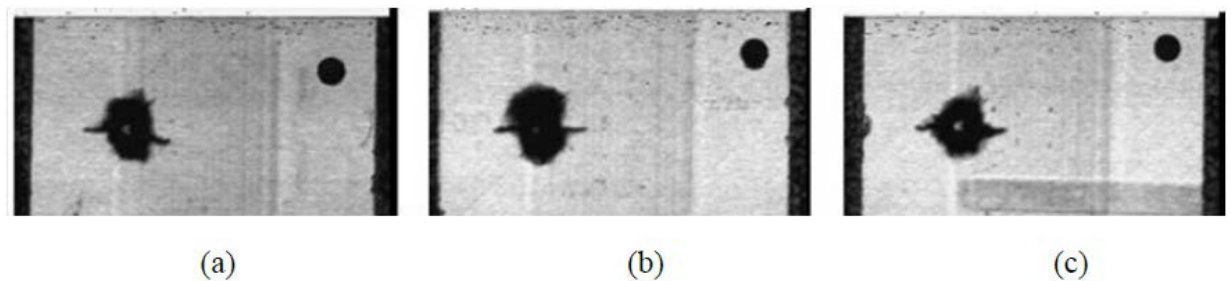


**Figure 52. C-Scans of 18-E1-20-TF-RTA-(1, 2, 3) of damage area and depth, respectively:  
 (a) 0.83 in<sup>2</sup>, 0.0095 in; (b) 1.16 in<sup>2</sup>, 0.0095 in; (c) 0.89 in<sup>2</sup>, 0.0085 in**

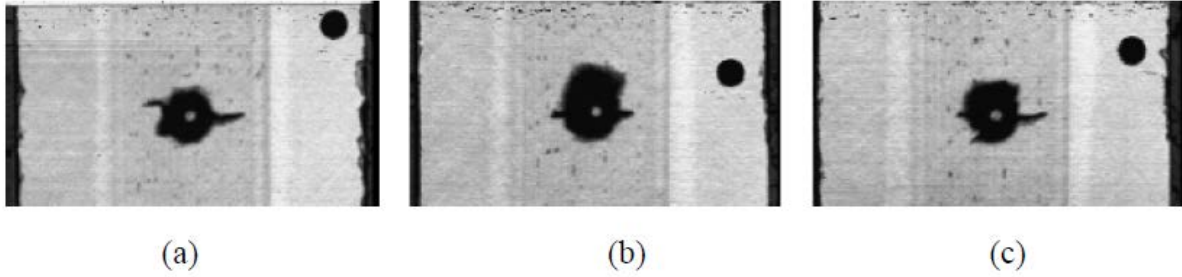


**Figure 53. C-Scans of 18-E1-20-CN-RTA-(1, 2, 3) of damage area and depth, respectively:  
 (a) 0.92 in<sup>2</sup>, 0.0065 in; (b) 1.39 in<sup>2</sup>, 0.0065 in; (c) 1.02 in<sup>2</sup>, 0.0075 in**

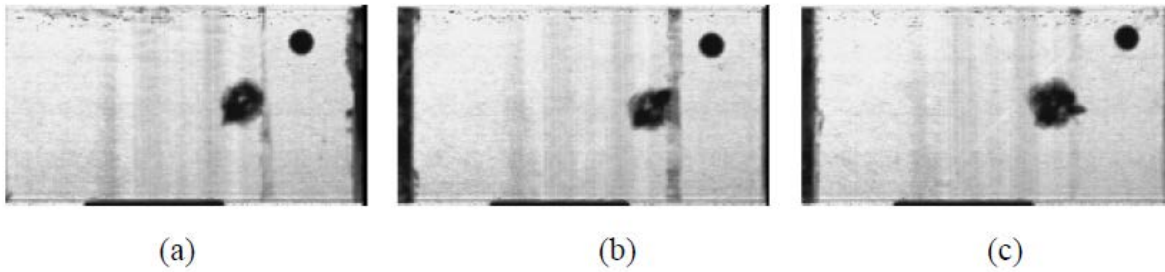


**Figure 54. C-Scans of 18-E2-20-TN-RTF-(1, 2, 3) of damage area and depth, respectively:  
 (a) 0.51 in<sup>2</sup>, 0.0095 in; (b) 0.54 in<sup>2</sup>, 0.01 in; (c) 0.67 in<sup>2</sup>, 0.0085 in**

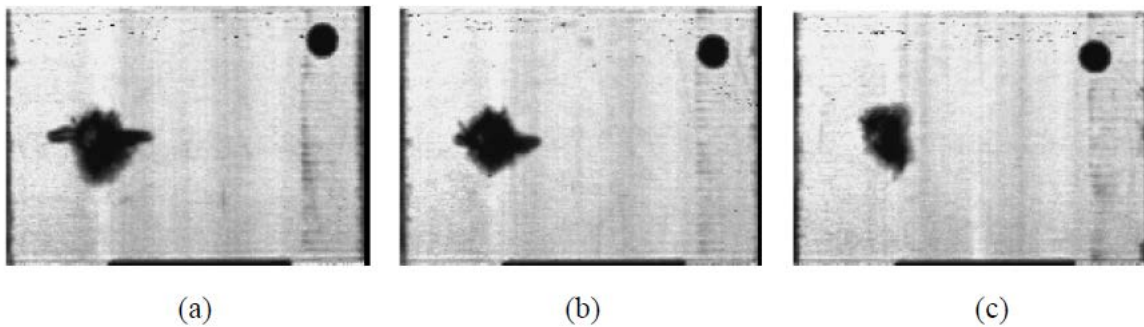


**Figure 55. C-Scans of 18-E2-20-TF-RTF-(1, 2, 3) of damage area and depth, respectively:  
 (a) 0.93 in<sup>2</sup>, 0.012 in; (b) 0.74 in<sup>2</sup>, 0.0115 in; (c) 0.52 in<sup>2</sup>, 0.0095 in**

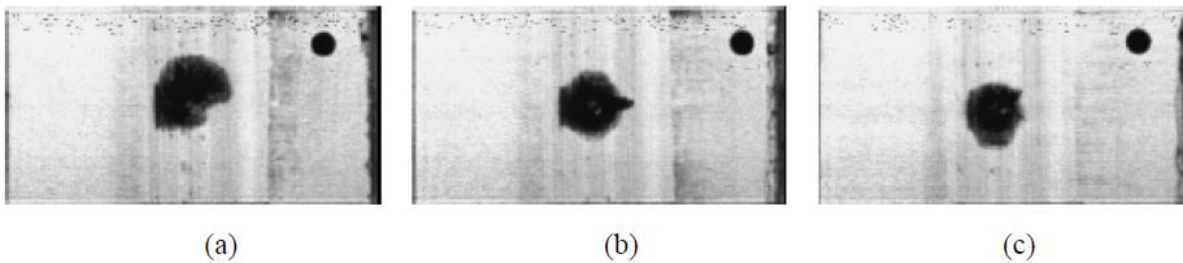


**Figure 56. C-Scans of 18-E2-20-CN-RTF-(1, 2, 3) of damage area and depth, respectively:  
 (a) 1.72 in<sup>2</sup>, 0.006 in; (b) 1.29 in<sup>2</sup>, 0.007 in; (c) 1.11 in<sup>2</sup>, 0.006 in**

Figures 57 and 58 show representative load displacement curves of damaged 18-ply scarf repairs tested at room temperature. Figure 59 shows the failure loads obtained for all static samples tested at room temperature. These samples were impacted at three different sites in the scarf joints (the TN, the TF, and the CN) using the same energy level, with the intent to induce a barely visible impact damage with a corresponding dent depth of 0.01". The results clearly show that the residual strength of a damaged scarf joint depends on the damage location in the joint.

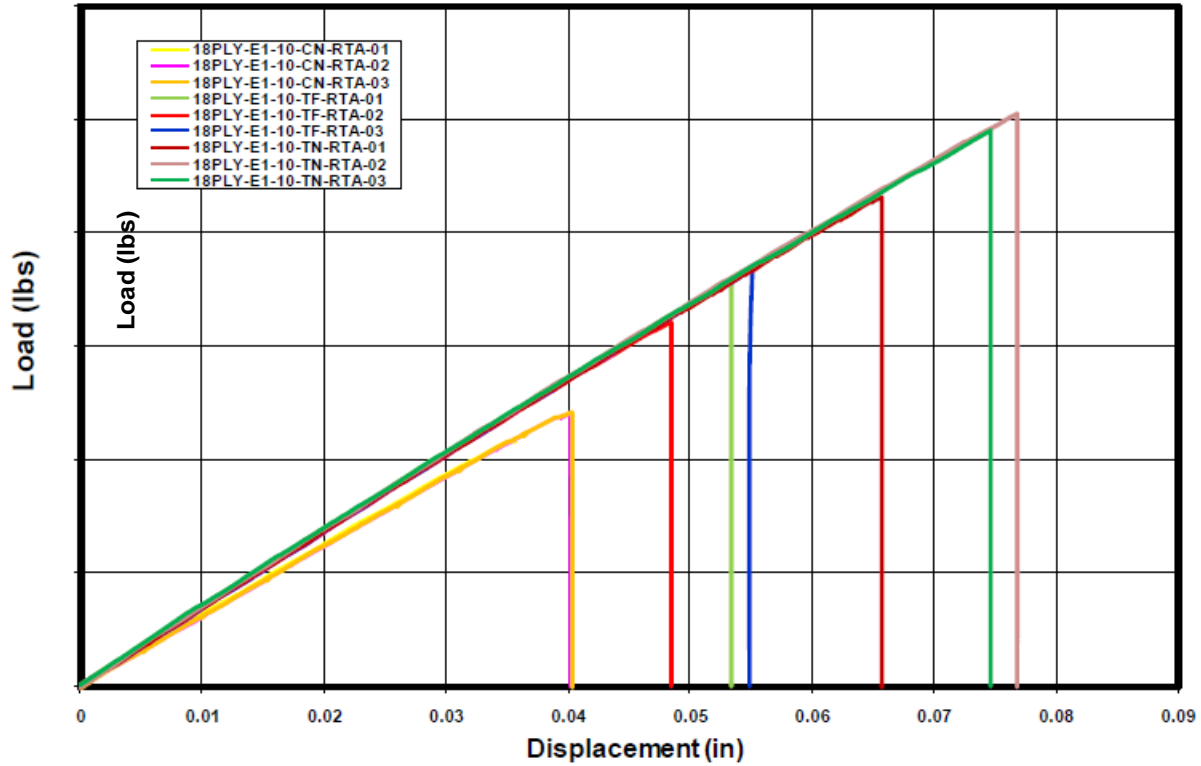


**Figure 57. Representative load vs. displacement curves of damaged 18-ply laminate scarf repairs tested at room temperature (1:10 scarf rate)**

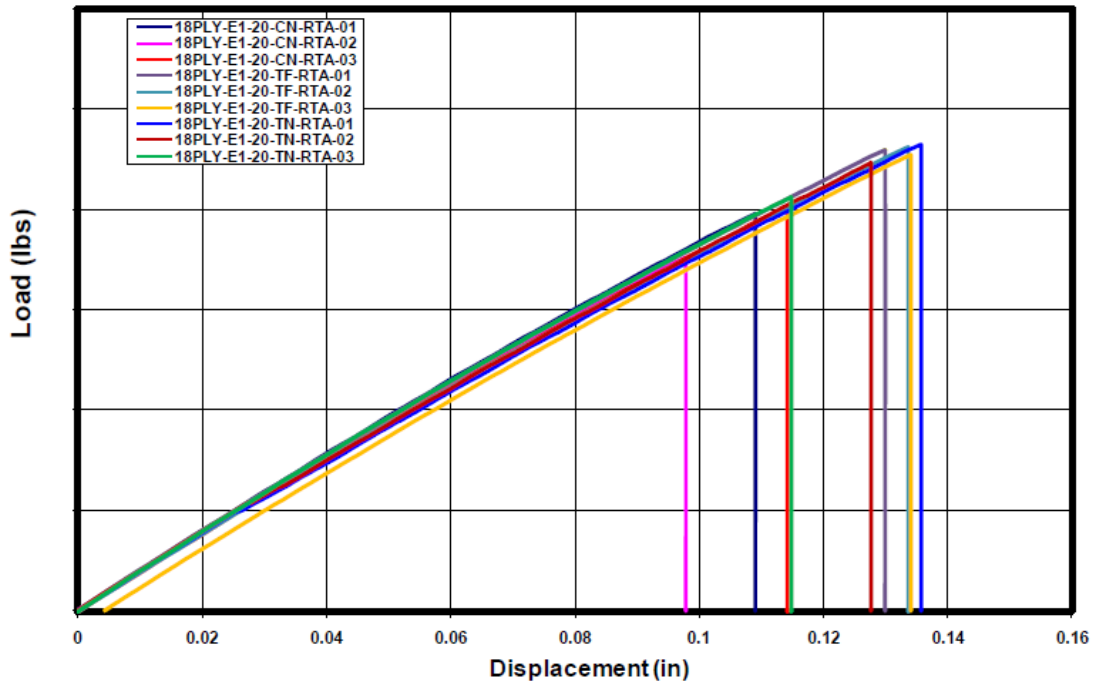


Figure 58. Representative load vs. displacement curves of damaged 18-ply laminate scarf repairs tested at room temperature (1:20 scarf rate)

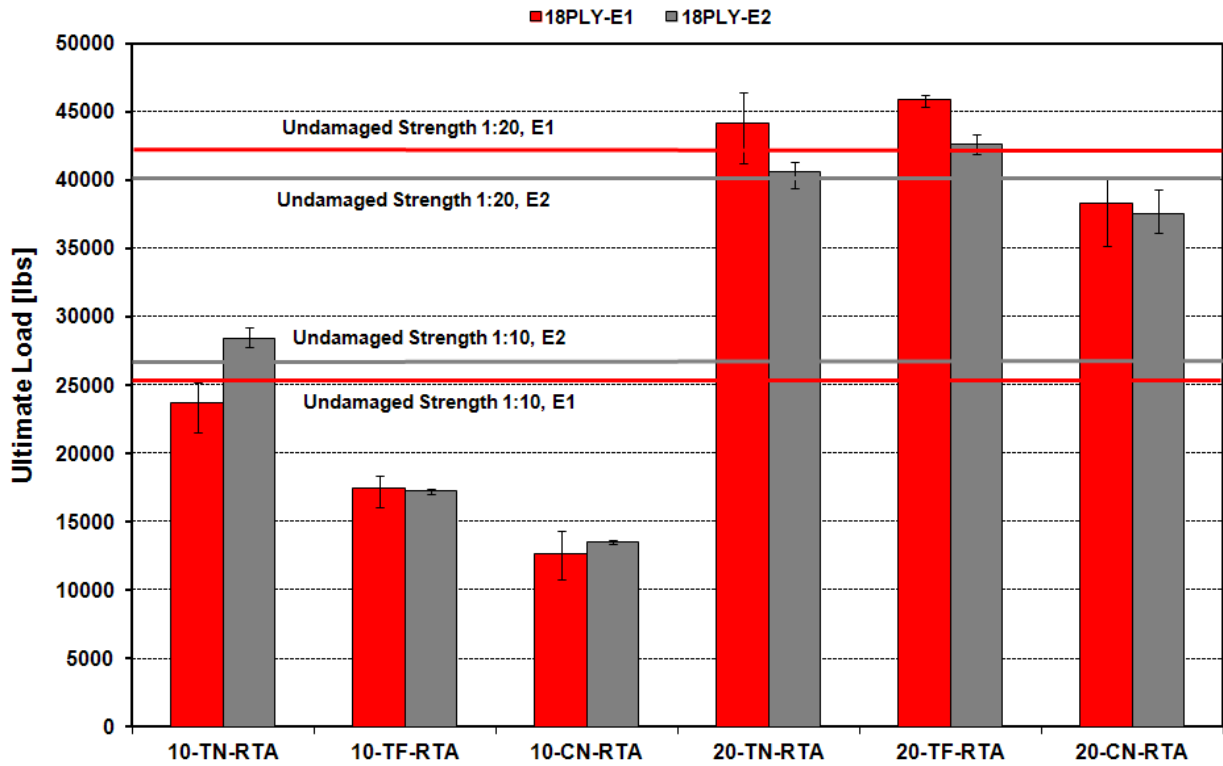
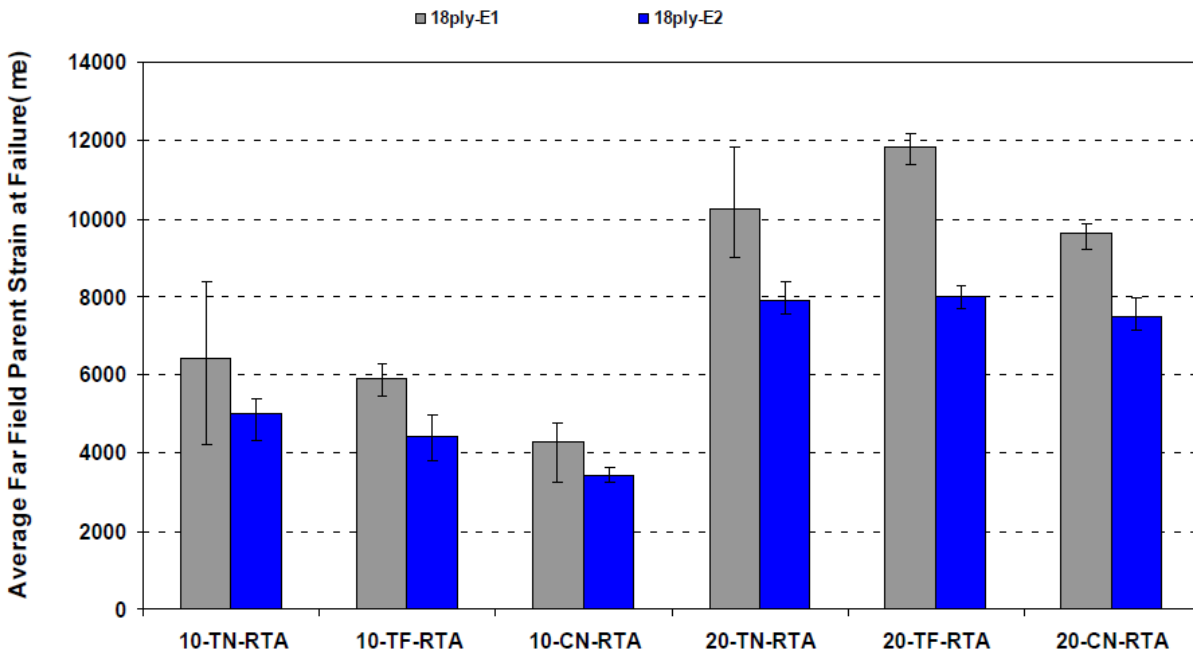


Figure 59. Residual strength after damage (static strength) of 18-ply laminate scarf repair configurations tested at room temperature

The ultimate loads of the 18-ply damaged scarf repairs are compared to those of undamaged repairs. For the 1:10 scarf rate configurations, the TN specimens yielded the highest residual strength, followed by the TF specimens, and the CN specimens yielded the lowest residual strength. For the 1:20 scarf rate configurations, the TF specimens had the highest residual strength, followed by the TN specimens, and the CN specimens yielded the lowest residual strength. The strength degradation observed for the 1:10 scarf repairs was more severe than that observed for the 1:20 scarf repair samples. For the same impact energy level inflicted on the 1:10 and 1:20 scarf repairs, the percentage of residual structurally sound bond area in the joint was higher for the larger scarf repairs (1:20).

Figure 60 shows the far field parent ultimate strains obtained for all 18-ply static samples tested at room temperature. The 18-ply-E1-10 configurations yielded average ultimate parent far field strains of 6415 $\mu\epsilon$ , 5915 $\mu\epsilon$ , and 4278 $\mu\epsilon$  for the TN, TF, and CN specimens, respectively. Similarly, the 18-ply-E2-10 configurations yielded average ultimate parent far field strains of 4994 $\mu\epsilon$ , 4405 $\mu\epsilon$ , and 3445 $\mu\epsilon$  for the TN, TF, and CN specimens, respectively. The 18-ply-E1-20 configurations yielded average ultimate parent far field strains of 10253 $\mu\epsilon$ , 11824 $\mu\epsilon$ , and 9606 $\mu\epsilon$  for the TN, TF, and CN specimens, respectively. Similarly, the 18-ply-E2-20 configurations yielded average ultimate parent far field strains of 7884 $\mu\epsilon$ , 7979 $\mu\epsilon$ , and 7501 $\mu\epsilon$  for the TN, TF, and CN specimens, respectively. The larger repairs (1:20) had a higher strain to failure than the smaller repairs (1:10), and the softer substrate (E1) yielded higher strains to failure than the stiffer substrate (E2).



**Figure 60. Far field parent strain at failure of 18-ply laminate scarf repair configurations**

Figures 61–66 show representative y-strain maps and corresponding longitudinal y-strain section plots lengthwise through the center of specimens impacted at the TN, TF, and CN, respectively. The impact site created a stress riser at the damage location, which appears to be the locus of failure initiation, as shown in the figures.

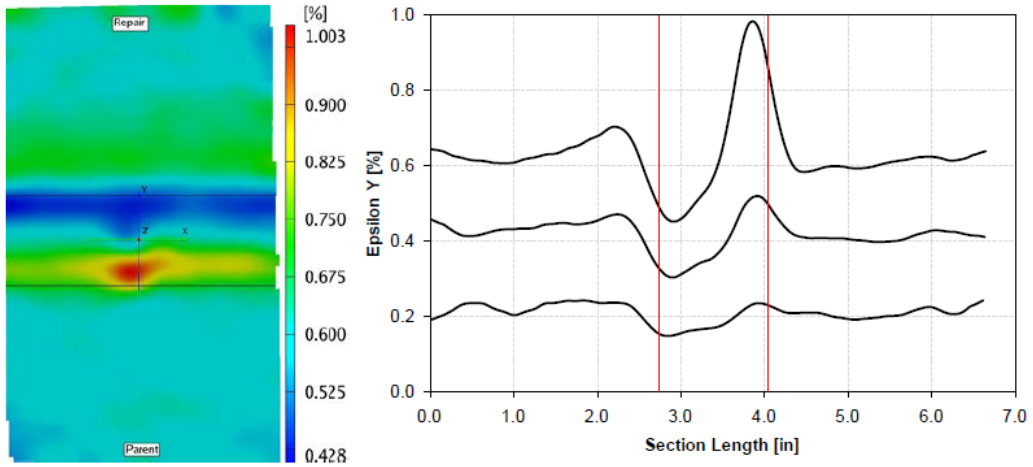


Figure 61. Y-strain distribution for 18-ply-E1-10-TN-RTA-02 scarf repair specimen

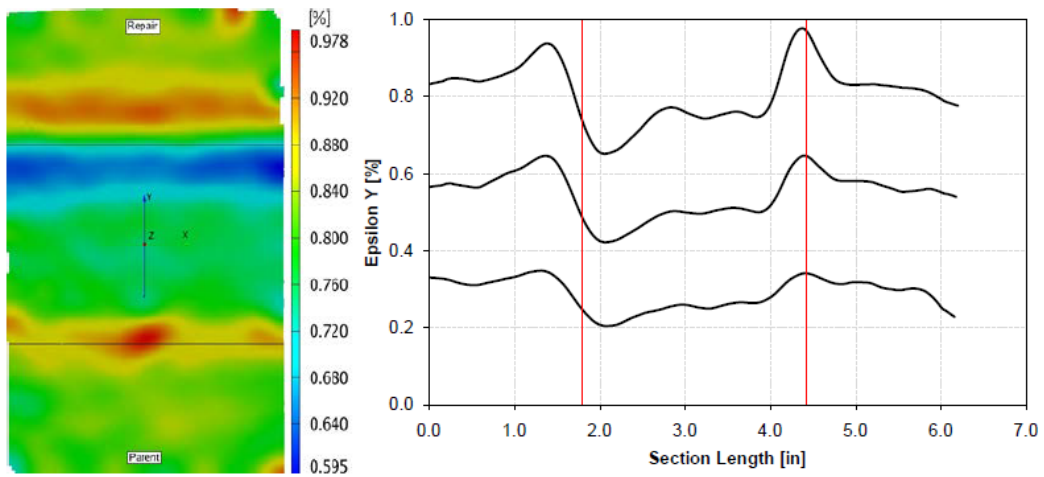


Figure 62. Y-strain distribution for 18-ply-E2-20-TN-RTA-03 scarf repair specimen

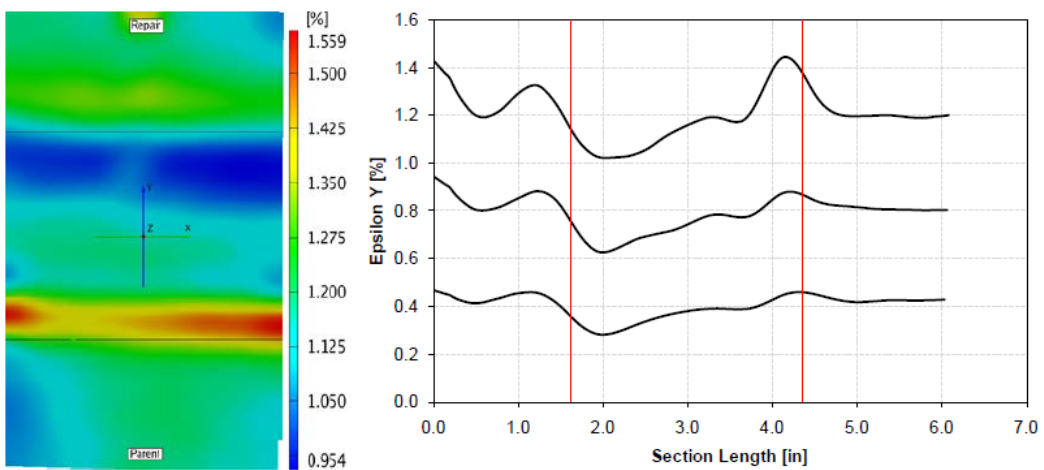
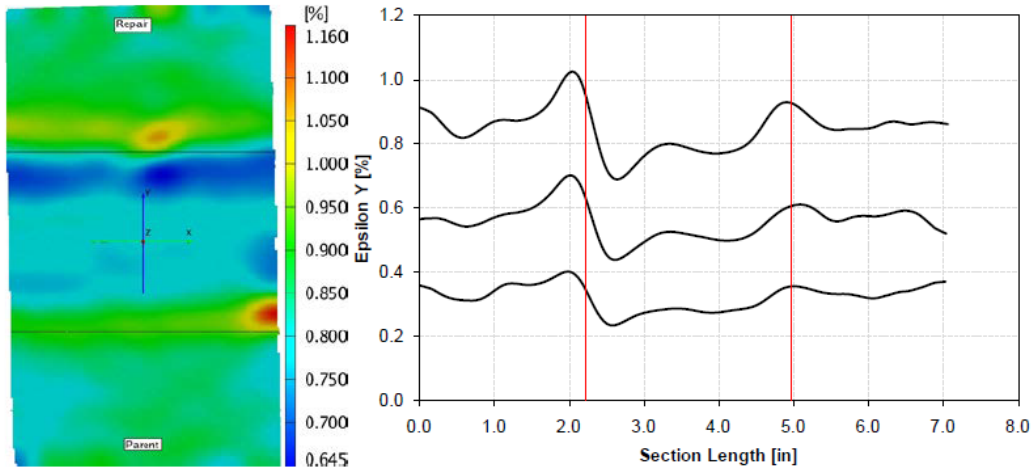
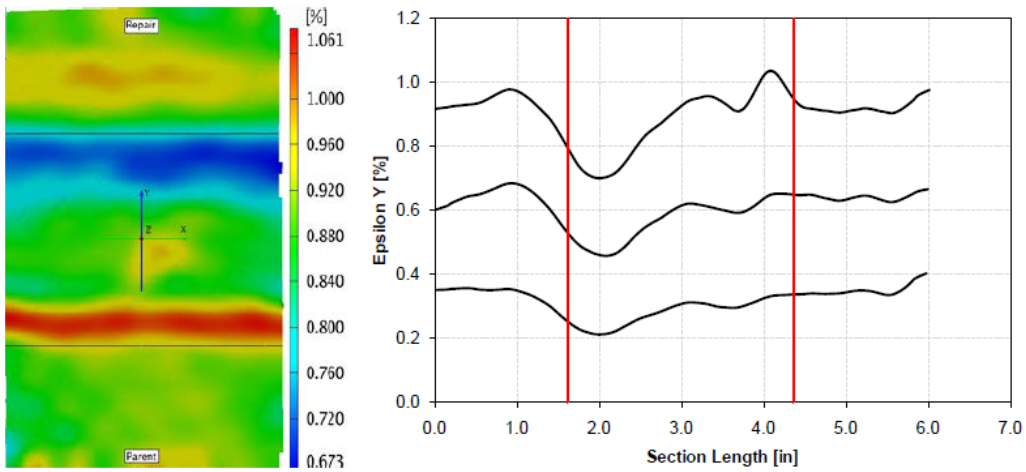


Figure 63. Y-strain distribution for 18-ply-E1-20-TF-RTA-03 scarf repair specimen



**Figure 64. Y-strain distribution for 18-ply-E2-20-TF-RTA-02 scarf repair specimen**



**Figure 65. Y-strain distribution for 18-ply-E1-20-CN-RTA-02 scarf repair specimen**

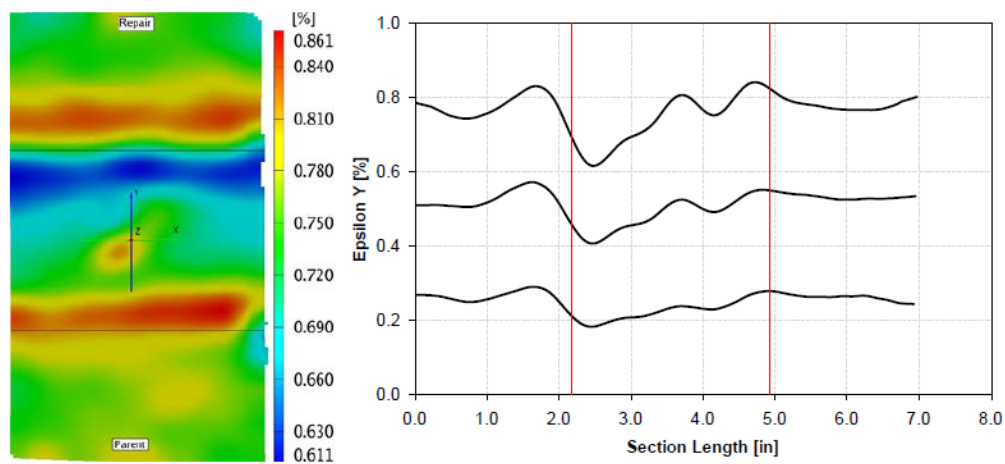


**Figure 66. Y-strain distribution for 18-ply-E2-20-CN-RTA-03 scarf repair specimen**

Cyclic testing was conducted on 1:10 and 1:20 specimens impacted at all three damage sites in the scarf repair TN, TF, and CN to interrogate the fatigue life of these repairs for a given stress level corresponding to a target far field strain level. The target fatigue life was 165,000 cycles and fatigue data are shown in tables 2 and 3. It should be noted that because of the limited number of samples, an S-N curve demonstrating the fatigue capability of these damaged repairs could not be established. The 18-ply-E1-10 specimens survived 165,000 cycles at a load level equivalent to 1750 $\mu\epsilon$ , 750 $\mu\epsilon$ , and 500 $\mu\epsilon$  for TN, TF, and CN configurations, respectively. Similarly, the 18-ply-E2-10 specimens survived 165,000 cycles at a load level equivalent to 1000 $\mu\epsilon$  and 750 $\mu\epsilon$  for TN and TF configurations, respectively. More extensive testing would need to be performed to assess fatigue capability with damage.

**Table 2. The 18-ply-10 fatigue data summary**

Panel Name	Specimen #	Frequency (Hz)	Number of Cycles	Fatigue Strain (microstrain)
18PLY-E1-10-TN-RTF	1	2	70,248	2000
	2	2	165,000	1500
	3	2	165,000	1750
18PLY-E1-10-TF-RTF	1	2	158	2000
	2	2	126,038	1000
	3	2	165,000	750
18PLY-E1-10-CN-RTF	1	2	5225	1000
	2	2	165,000	500
	3	2	129,227	750
18PLY-E2-10-TN-RTF	1	2	333	3000
	2	2	102,368	2000
	3	2	165,000	1000
18PLY-E2-10-TF-RTF	1	2	165,000	750
	2	2	165,000	500
	3	2	24,357	1000
18PLY-E2-10-CN-RTF	1	2	36,922	500
	2	2	22,559	500
	3	2	580	1000

**Table 3. The 18-ply-20 fatigue data summary**

Panel Name	Specimen #	Frequency (Hz)	Number of Cycles	Fatigue Strain (microstrain)
18PLY-E1-20-TN-RTF	1	2	83,284	3000
	2	2	85,947	3000
	3	2	77,873	3000
18PLY-E1-20-TF-RTF	1	2	165,000	3000
	2	2	165,000	3000
	3	2	165,000	3000
18PLY-E1-20-CN-RTF	1	2	6422	3000
	2	2	21,228	3000
	3	2	72,334	3000
18PLY-E2-20-TN-RTF	1	2	13,595	3000
	2	2	11,882	3000
	3	2	22,991	3000
18PLY-E2-20-TF-RTF	1	2	4708	3000
	2	2	10,442	3000
	3	2	10,468	3000
18PLY-E2-20-CN-RTF	1	2	11,708	3000
	2	2	11,947	3000
	3	2	21,855	3000

All 18-ply-E1-20 specimens were cycled at a load equivalent to 3000 $\mu\epsilon$  far field and the resulting average cycles to failure were 82,368 cycles, 165,000 cycles (specimens did not fail), and 33,328 cycles for the TN, TF, and CN, respectively. All 18-ply-E2-20 specimens were cycled at a load equivalent to 3000 $\mu\epsilon$  far field, and the resulting average cycles to failure were 16,156 cycles, 8539 cycles, and 15,170 cycles for the TN, TF, and CN, respectively. The cyclic data showed a reduction in the fatigue life (165,000 cycles for the undamaged scarf repairs) due to the inflicted damage.

Failure modes were very consistent for all specimens tested at room temperature and all specimens failed in the scarf joint. The dominant failure mode was a cohesive failure of the adhesive mainly in the 45 and 0 plies and a 90 ply peel/tension failure as shown in figures 67–72. For the specimens impacted at the CN, damage/disbond in the bondline was observed after failure.



**Figure 67. Failure modes: 18-ply-E1-10-CN-RTA-XX**

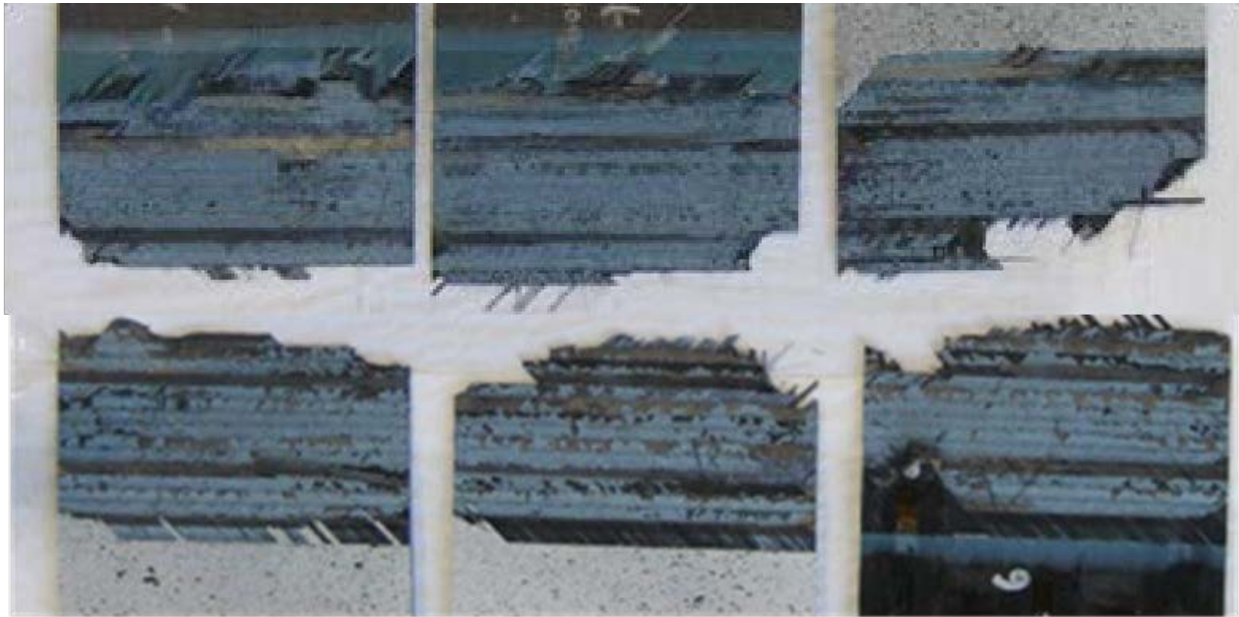


**Figure 68. Failure modes: 18-ply-E1-20-TF-RTA-XX**

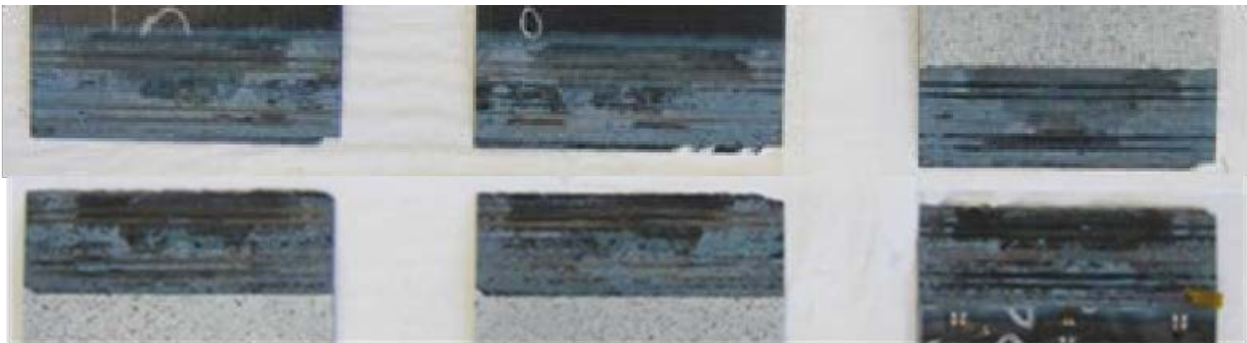


**Figure 69. Failure modes: 18-ply-E2-10-CN-RTA-XX**



**Figure 70. Failure modes: 18-ply-E2-10-TF-RTA-XX**

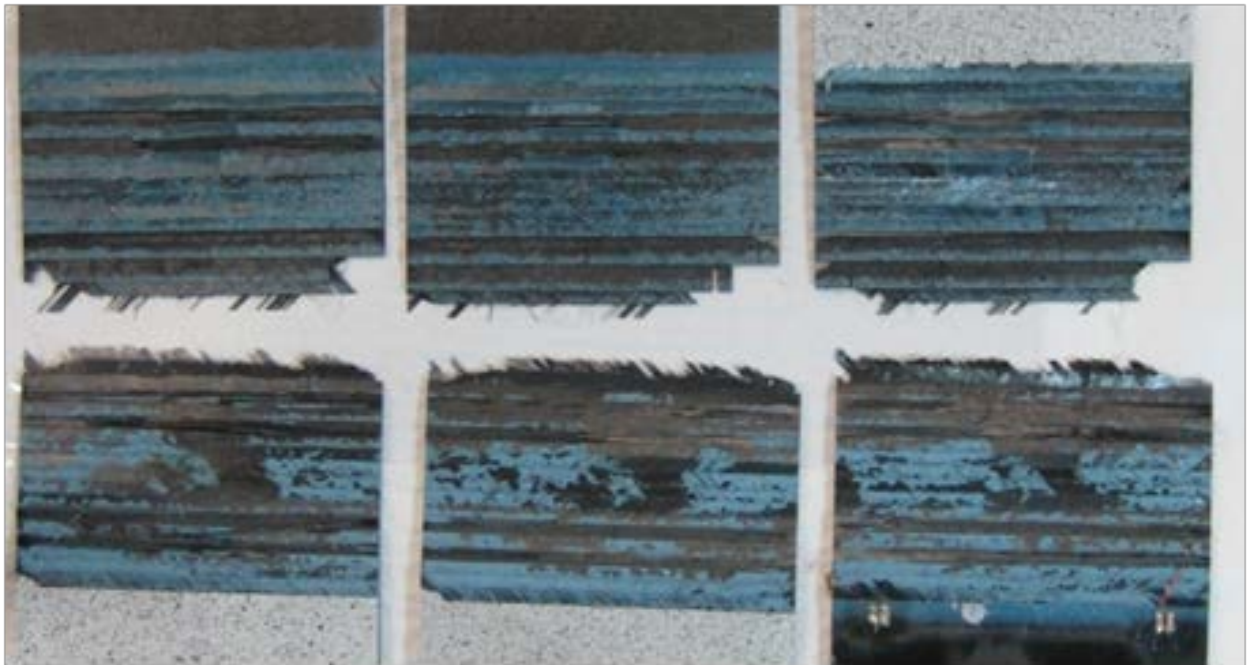


**Figure 71. Failure modes: 18-ply-E2-20-CN-RTA-XX**



**Figure 72. Failure modes: 18-ply-E2-20-TN-RTA-XX**

### 3.2 48-PLY REPAIR LAMINATE DAMAGE TOLERANCE RESULTS

Figure 73 shows C-Scan planar damage areas for all 48-ply scarf repairs after impact. Figures 74–85 are representative C-Scan images obtained for all specimens subsequently tested at room temperature. As shown in figure 73, for both substrate moduli considered and regardless of scarf ratio, the TN impacts yielded the smallest damage areas followed by the TF impacts and the CN impacts. The same energy level inflicted at different sites in the repair yielded different damage sizes, with the impacts inflicted at the CN being the most severe. A close examination of the C-scans shows a large scatter in the damage areas obtained for identical samples impacted with the same energy level.

Comparing average damage areas, the TN and TF impacts yielded comparable damage areas for both 1:10 to 1:20 scarf ratios. The TN impact yielded 17% and 15% bond damaged area for the 48-ply-E1-10-TN and 48-ply-E2-10-TN specimens, respectively, and 9% and 7% damaged bond area for the 48-ply-E1-20-TN and 48-ply-E2-20-TN, respectively. The TF impact yielded 17% and 18% damage at the scarf overlap area for the 48-ply-E1-10-TF and 48-ply-E2-10-TF specimens, respectively, and 11% and 10% damage at the scarf overlap area for the 48-ply-E1-20-TF and 48-ply-E2-20-TF, respectively. The CN impact yielded 32% and 40% damage at the scarf overlap area for the 48-ply-E1-10-CN and 48-ply-E2-10-CN specimens, respectively, and 14% and 15% damage at the scarf overlap area for the 48-ply-E1-20-CN and 48-ply-E2-20-CN, respectively.

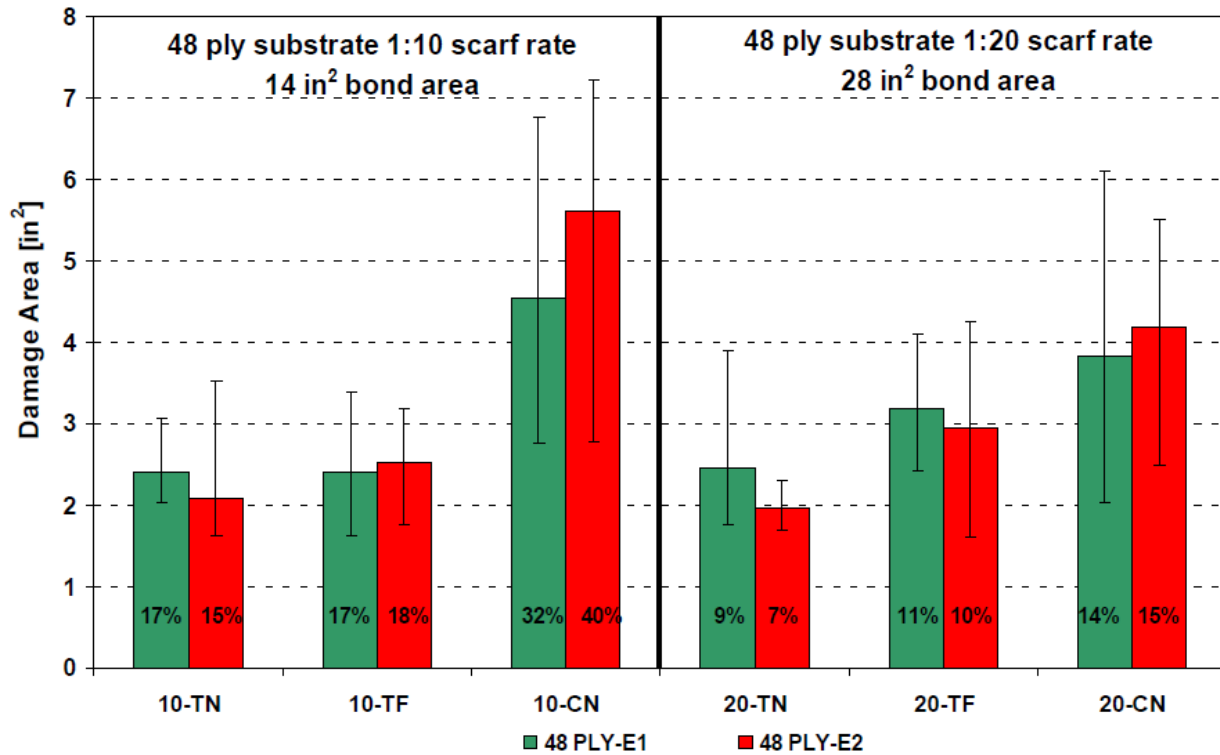


Figure 73. Impact data summary for all 48-ply scarf repair specimens

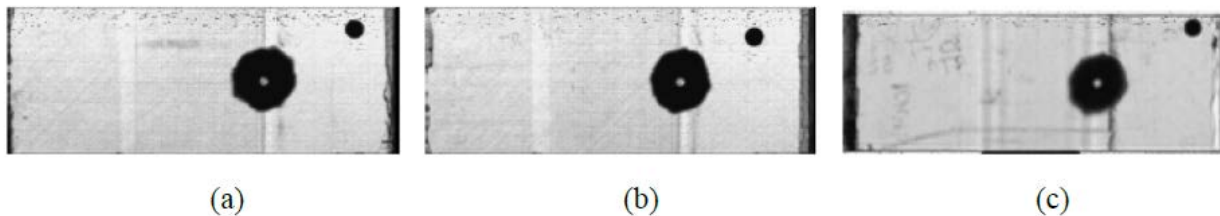


Figure 74. C-scans of 48-E1-10-TN-RTA-(1, 2, 3) of damage area and depth, respectively:  
 (a) 2.1368 in<sup>2</sup>, 0.009 in; (b) 2.054 in<sup>2</sup>, 0.0095 in; (c) 2.22 in<sup>2</sup>, 0.0095 in

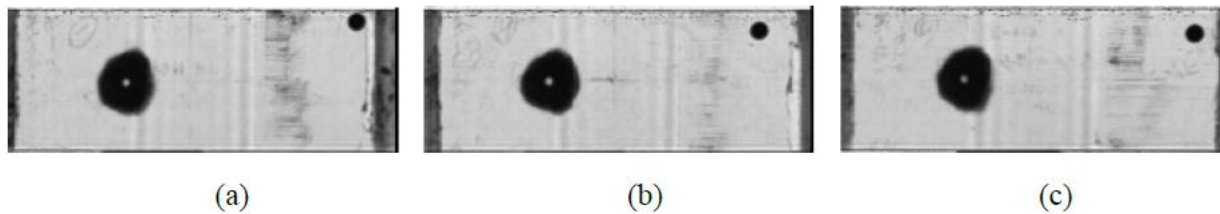
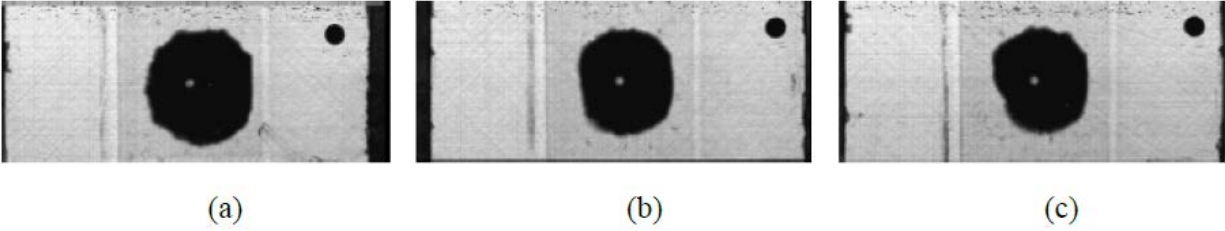
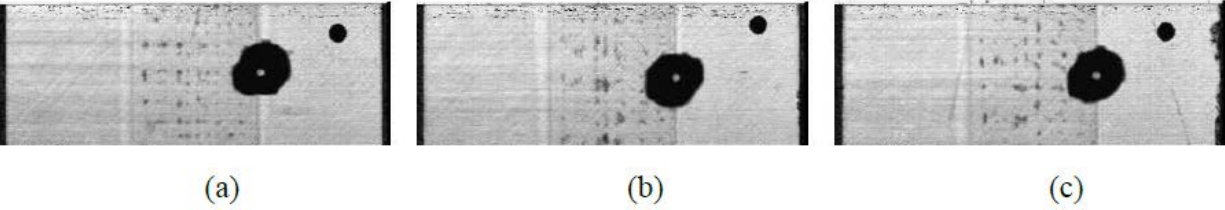


Figure 75. C-scans of 48-E1-10-TF-RTA-(1, 2, 3) of damage area and depth, respectively:  
 (a) 2.152 in<sup>2</sup>, 0.011 in; (b) 2.1564 in<sup>2</sup>, 0.0115 in; (c) 2.0228 in<sup>2</sup>, 0.0105 in



**Figure 76. C-scans of 48-E1-10-CN-RTA-(1, 2, 3) of damage area and depth, respectively: (a) 6.2796 in<sup>2</sup>, 0.0095 in; (b) 5.0008 in<sup>2</sup>, 0.008 in; (c) 4.808 in<sup>2</sup>, 0.012 in**



**Figure 77. C-scans of 48-ply-E2-10-TN-RTA of damage area and depth, respectively: (a) 1.91 in<sup>2</sup>, 0.0085 in; (b) 1.88 in<sup>2</sup>, 0.011 in; (c) 1.87 in<sup>2</sup>, 0.0085 in**

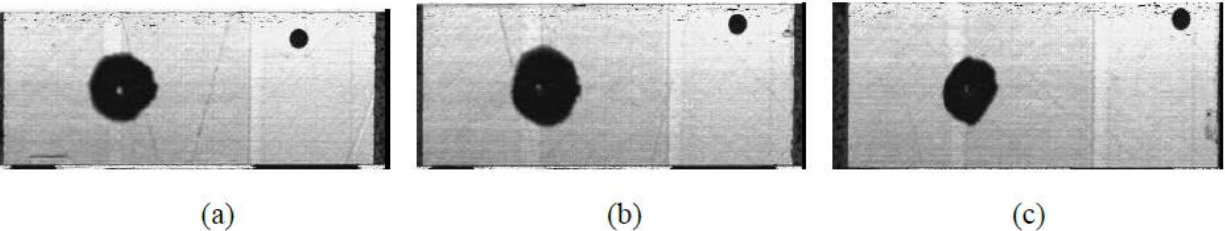


**Figure 78. C-scans of 48-ply-E2-10-TF-RTA of damage area and depth, respectively: (a) 2.56 in<sup>2</sup>, 0.011 in; (b) 2.92 in<sup>2</sup>, 0.009 in; (c) 1.75 in<sup>2</sup>, 0.013 in**

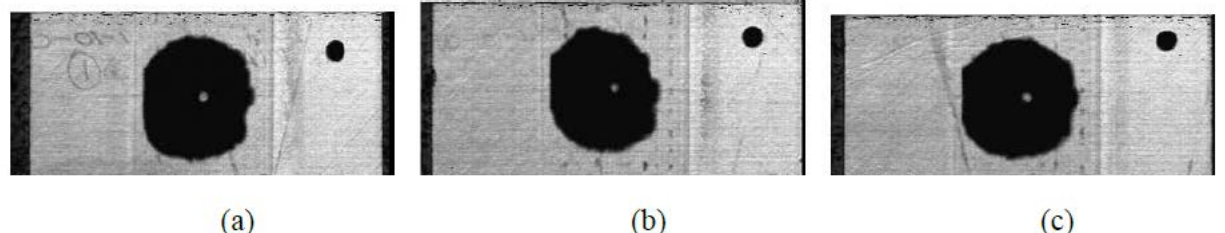


**Figure 79. C-scans of 48-ply-E2-10-CN-RTA damage area and depth, respectively: (a) 7.22 in<sup>2</sup>, 0.008 in; (b) 6.30 in<sup>2</sup>, 0.008 in; (c) 7 in<sup>2</sup>, 0.008 in**

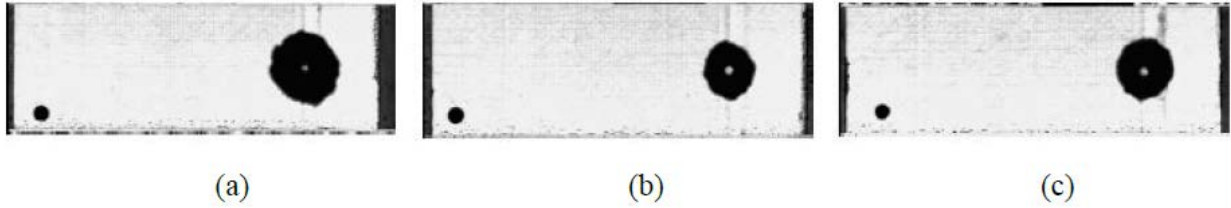


**Figure 80. C-scans of 48-E1-20-TN-RTA-(1, 2, 3) of damage area and depth, respectively:  
 (a) 2.8312 in<sup>2</sup>, 0.0105 in; (b) 2.0252 in<sup>2</sup>, 0.01 in; (c) 3.894 in<sup>2</sup>, 0.011 in**

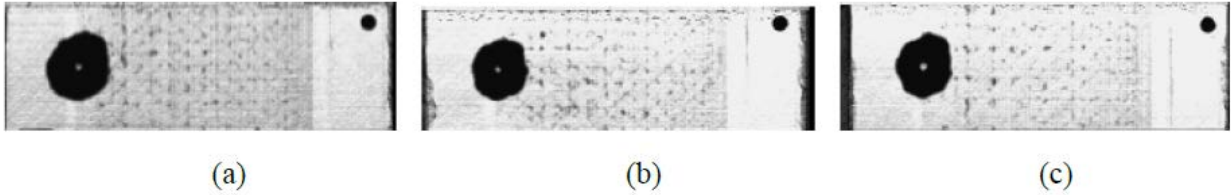


**Figure 81. C-scans of 48-E1-20-TF-RTA-(1, 2, 3) of damage area and depth, respectively:  
 (a) 3.4948 in<sup>2</sup>, 0.0105 in; (b) 2.8096 in<sup>2</sup>, 0.012 in; (c) 2.7856 in<sup>2</sup>, 0.012 in**

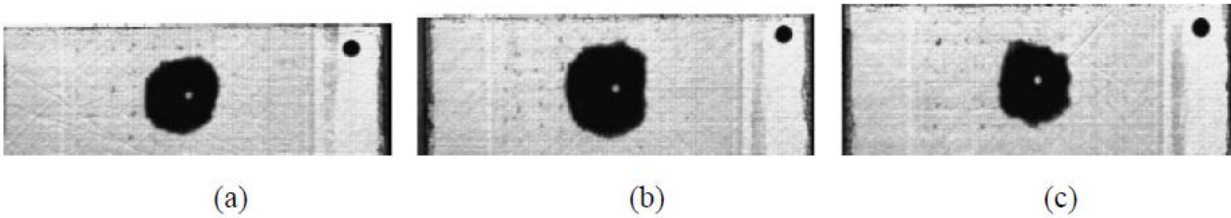


**Figure 82. C-scans of 48-E1-20-CN-RTA-(1, 2, 3) of damage area and depth, respectively:  
 (a) 3.9376 in<sup>2</sup>, 0.008 in; (b) 5.2012 in<sup>2</sup>, 0.0075 in; (c) 3.6064 in<sup>2</sup>, 0.008 in**

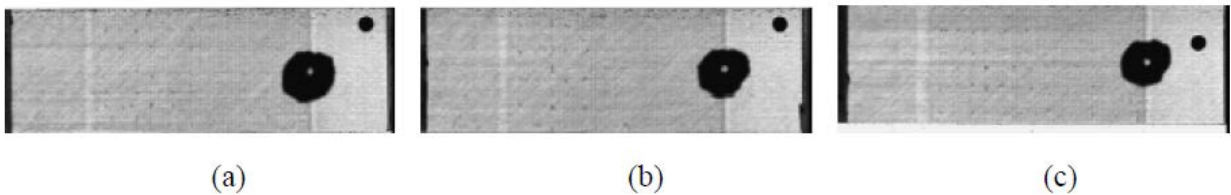


**Figure 83. C-scans of 48-E2-20-TN-RTA-(1, 2, 3) of damage area and depth, respectively:  
 (a) 2.118 in<sup>2</sup>, 0.01 in; (b) 2.016 in<sup>2</sup>, 0.011 in; (c) 1.914 in<sup>2</sup>, 0.0095 in**

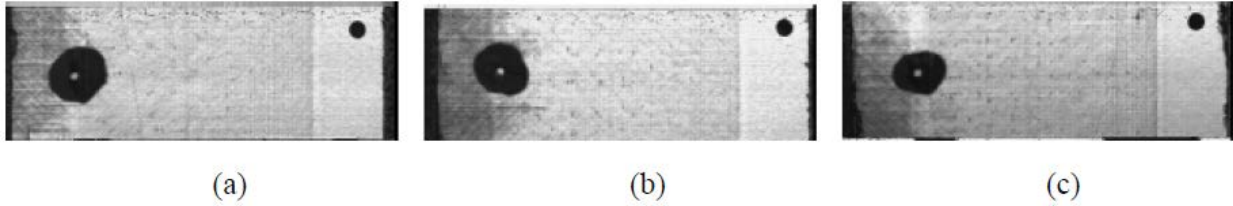


**Figure 84. C-scans of 48-E2-20-TF-RTA-(1, 2, 3) of damage area and depth, respectively:  
 (a) 2.326 in<sup>2</sup>, 0.0075 in; (b) 1.968 in<sup>2</sup>, 0.0085 in; (c) 1.602 in<sup>2</sup>, 0.0085 in**

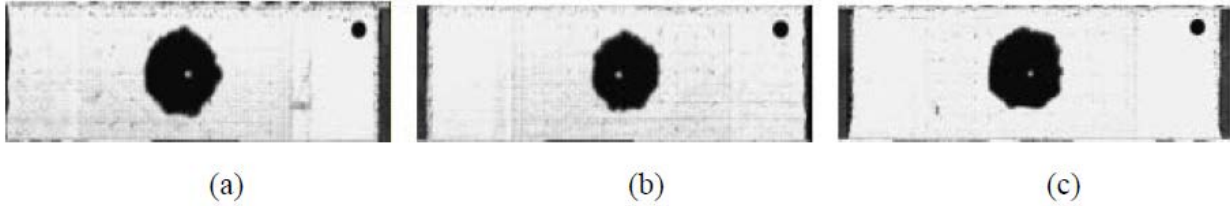


**Figure 85. C-scans of 48-E2-20-CN-RTA-(1, 2, 3) of damage area and depth, respectively:  
 (a) 4.9112 in<sup>2</sup>, 0.009 in; (b) 3.7932 in<sup>2</sup>, 0.0095 in; (c) 4.9392 in<sup>2</sup>, 0.0115 in**

Figures 86 and 87 show representative load displacement curves of damaged 48-ply scarf repairs tested at room temperature. Figure 88 shows a summary of the failure loads obtained for all damaged static samples tested at room temperature. These samples were impacted at three different sites in the scarf joints (at the TN, the TF, and the CN) using the same energy level, with the intent to induce a barely visible impact damage with a corresponding dent depth of 0.01". The results clearly show that the residual strength of a damaged scarf joint depends on the damage location in the joint.

The ultimate loads of the damaged scarf repairs were compared to those of pristine, undamaged repairs. The failure load values shown in figure 88 correlated very well with the C-Scan data summarized in figure 73; the specimens with the largest damage yielded the lowest residual strength. The 48-ply-TN specimens produced the highest residual strength regardless of scarf/repair size (smallest damage area), followed by the TF specimens, with the CN specimens yielding the lowest strengths (largest damage area). The magnitude of the strength degradation observed for the 1:10 scarf repairs was more severe than that observed for the 1:20 scarf repair samples. For the same impact energy level inflicted on the 1:10 and 1:20 scarf repairs, the percentage of residual structurally sound bonded area around the damage was higher for the larger scarf repairs (1:20).

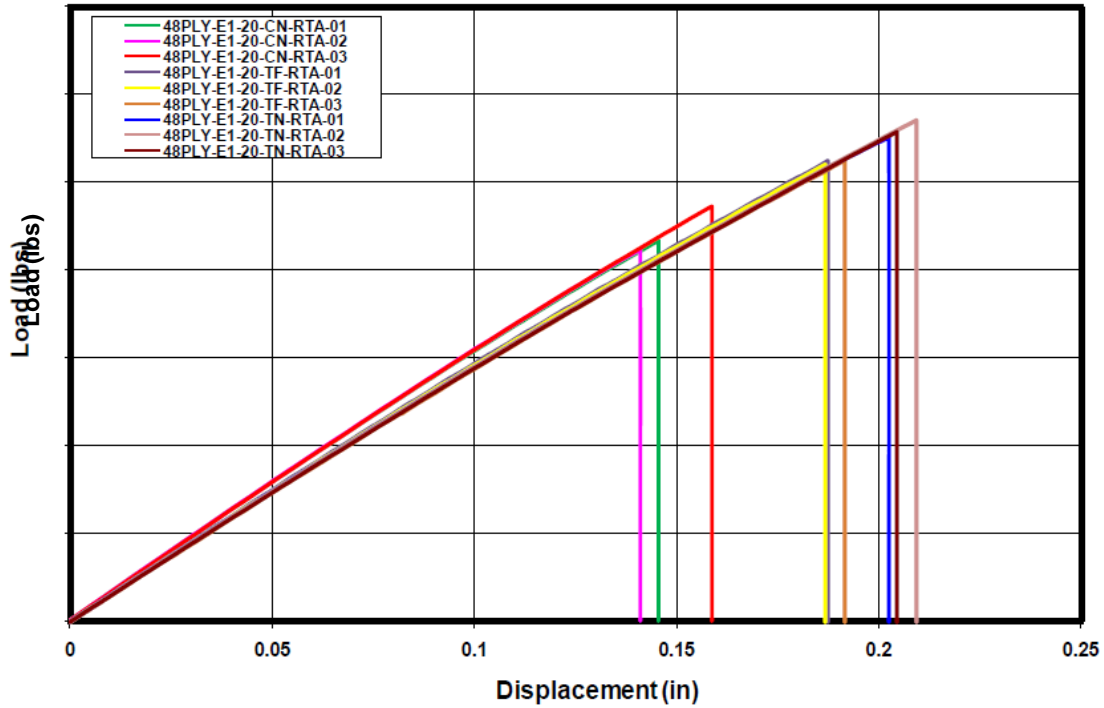


Figure 86. Representative load vs. displacement curves of damaged 48-ply laminate scarf repairs tested at room temperature (1:20 scarf rate)

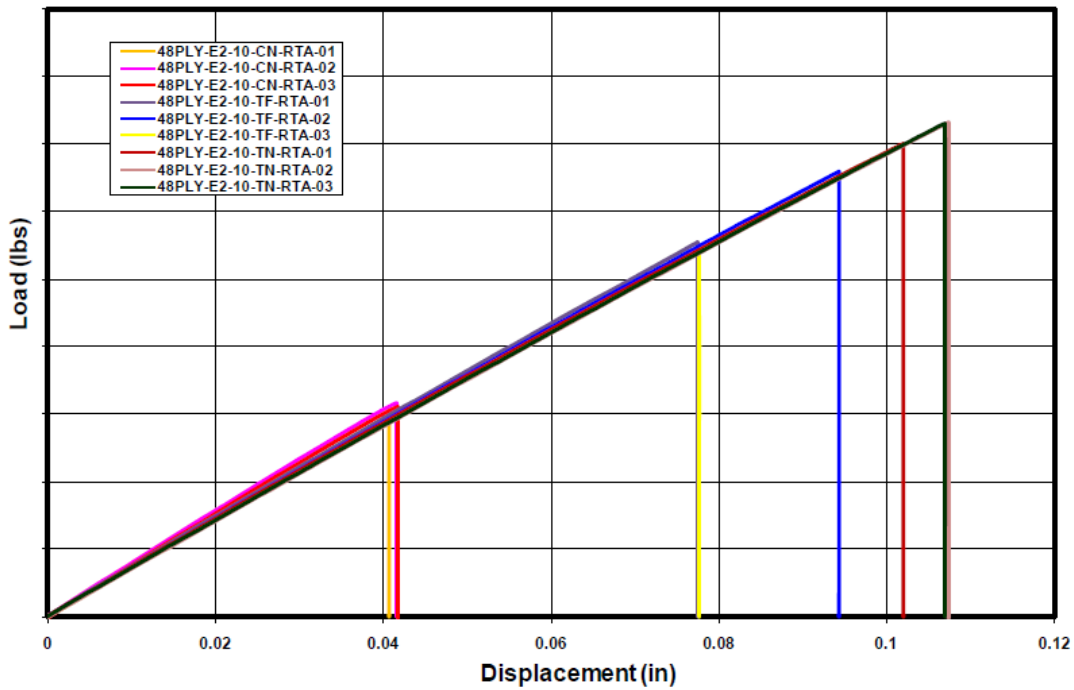
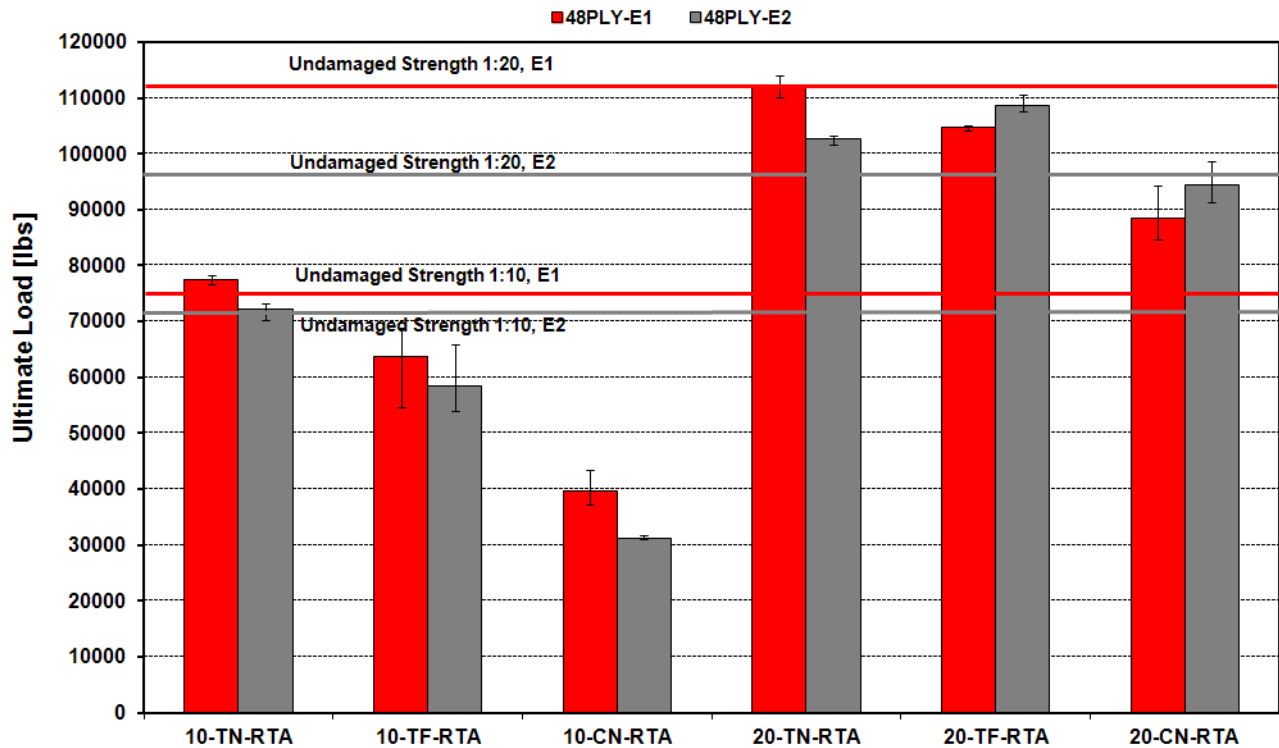


Figure 87. Representative load vs. displacement curves of damaged 48-ply laminate scarf repairs tested at room temperature (1:10 scarf rate)



**Figure 88. Residual strength after damage (static strength) of 48-ply laminate scarf repair configurations**

Figure 89 shows a summary of the far field parent ultimate strains obtained for all static damaged scarf repairs tested at room temperature. The results of figure 88 correlated with those in figure 89. The TN specimens resulted in the highest residual strengths and corresponding far field parent ultimate strains (these samples had the smallest damage area) followed by the TF specimens and the CN specimens. The CN specimens yielded the lowest strengths and corresponding far field parent ultimate strains (largest damage area). The 48-ply-E1-10 configurations yielded average ultimate parent far field strains of  $6685\mu\epsilon$ ,  $5597\mu\epsilon$ , and  $3749\mu\epsilon$  for the TN, TF, and CN specimens, respectively. Similarly, the 48-ply-E2-10 configurations yielded average ultimate parent far field strains of  $4982\mu\epsilon$ ,  $4207\mu\epsilon$ , and  $2601\mu\epsilon$  for the TN, TF, and CN specimens, respectively.

The 48-ply-E1-20 configurations yielded average ultimate parent far field strains of  $10302\mu\epsilon$ ,  $9051\mu\epsilon$ , and  $8056\mu\epsilon$  for the TN, TF, and CN specimens, respectively. Similarly, the 48-ply-E2-20 configurations yielded average ultimate parent far field strains of  $7429\mu\epsilon$ ,  $8345\mu\epsilon$ , and  $7113\mu\epsilon$  for the TN, TF, and CN specimens, respectively. The larger repairs (1:20) failed at higher strains than the smaller repairs, and the softer substrate (E1) yielded higher strains to failure than the stiffer substrate (E2). The mechanical data correlated very well with the impact data (damage area).

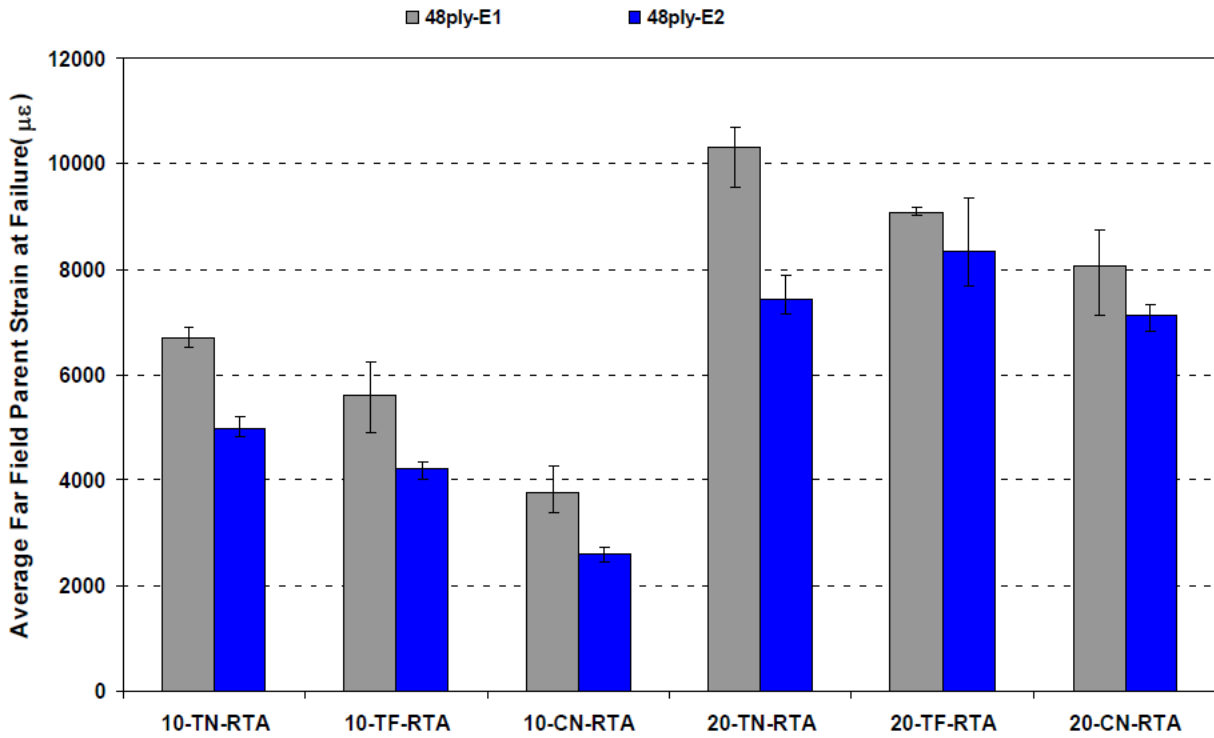


**Figure 89. Far field parent strain at failure of 48-ply laminate scarf repair configurations**

Figures 90–96 are representative y-strain maps and corresponding longitudinal y-strain section plots lengthwise through the center of specimens impacted at the TN, TF, and CN, respectively.

The impact site created a stress riser at the damage location, which appears to be the locus of failure initiation, as shown in the figures.

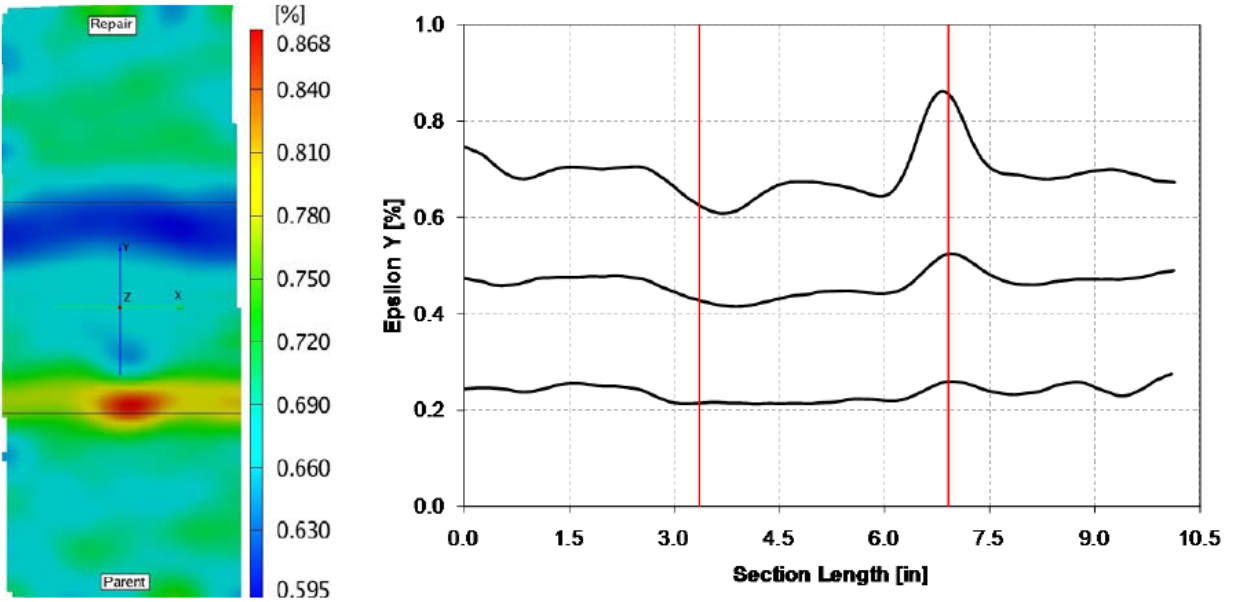


**Figure 90. Y-strain distribution 48-ply-E1-10-TN-RTA-2 scarf repair specimen**

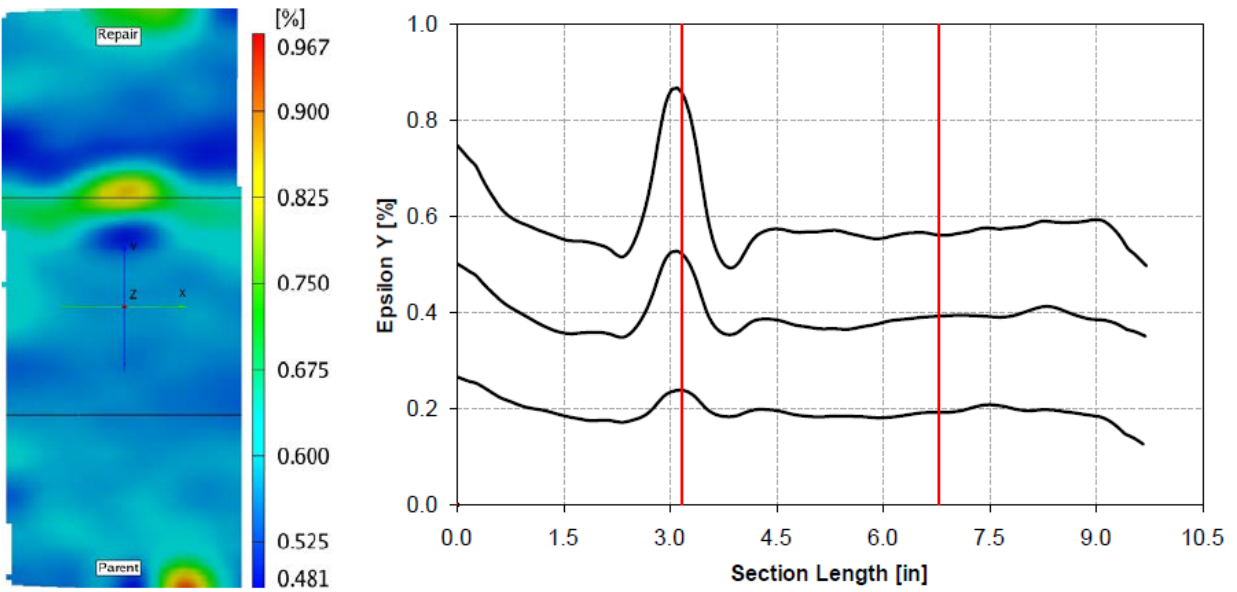


**Figure 91. Y-strain distribution 48-ply-E1-10-TF-RTA-01 scarf repair specimen**

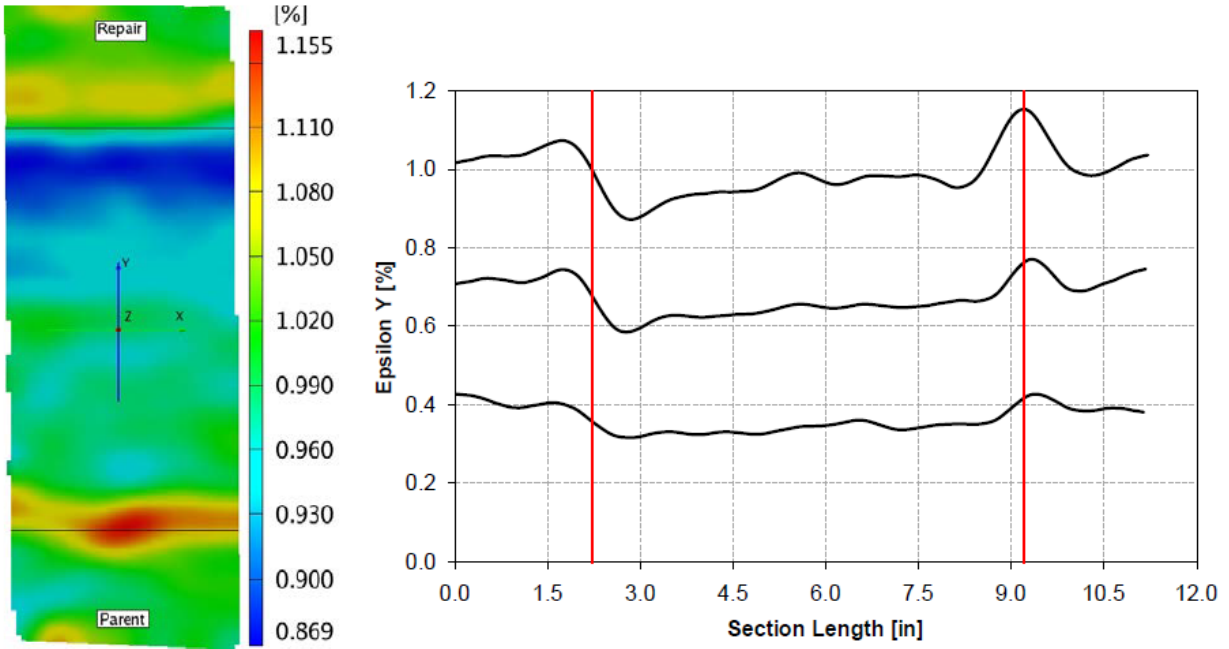


**Figure 92. Y-strain distribution 48-ply-E1-20-TN-RTA-03 scarf repair specimen**

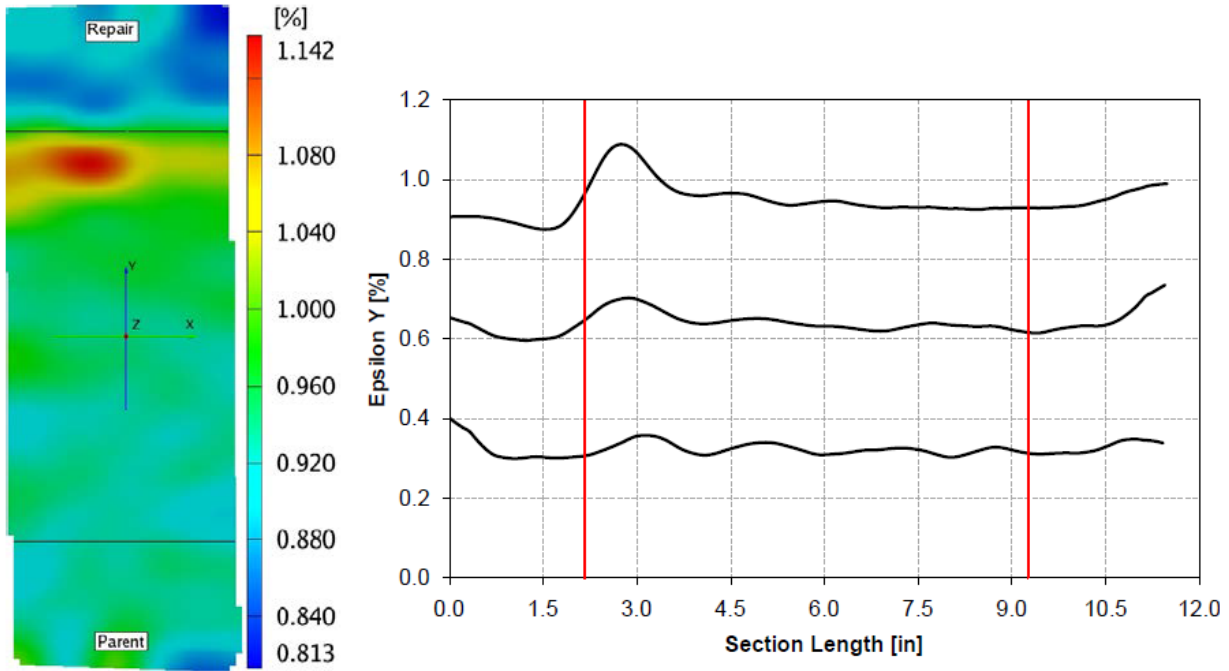


**Figure 93. Y-strain distribution 48-ply-E1-20-TF-RTA-01 scarf repair specimen**

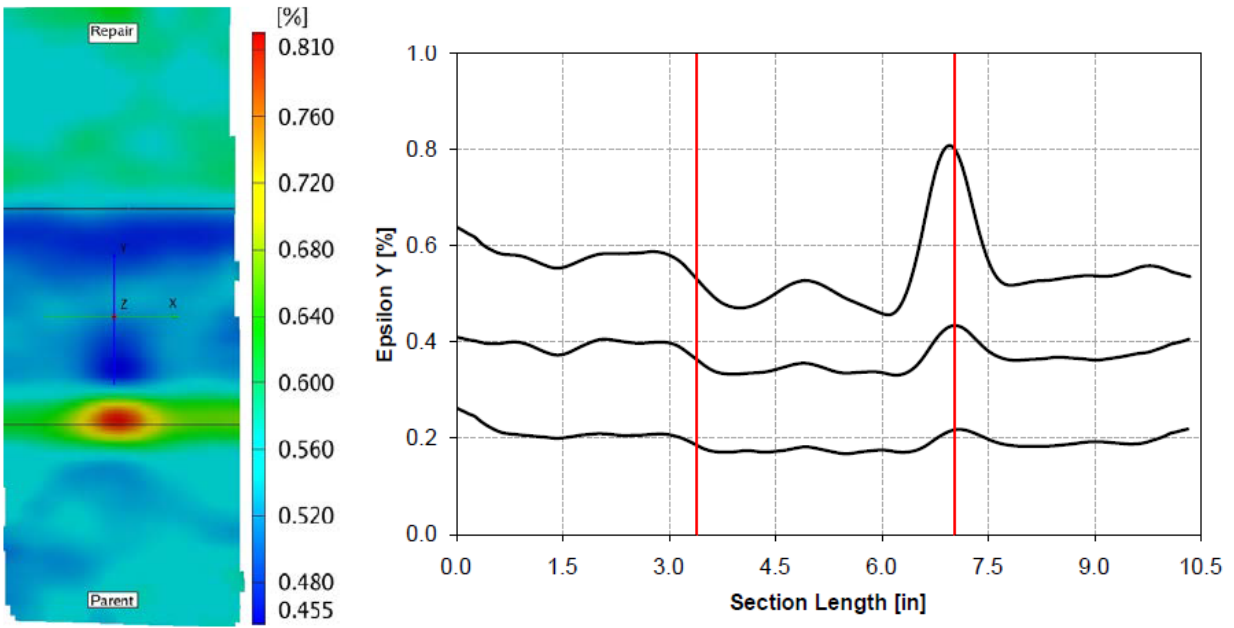


**Figure 94. Y-strain distribution 48-ply-E2-10-TN-RTA-2 scarf repair specimen**

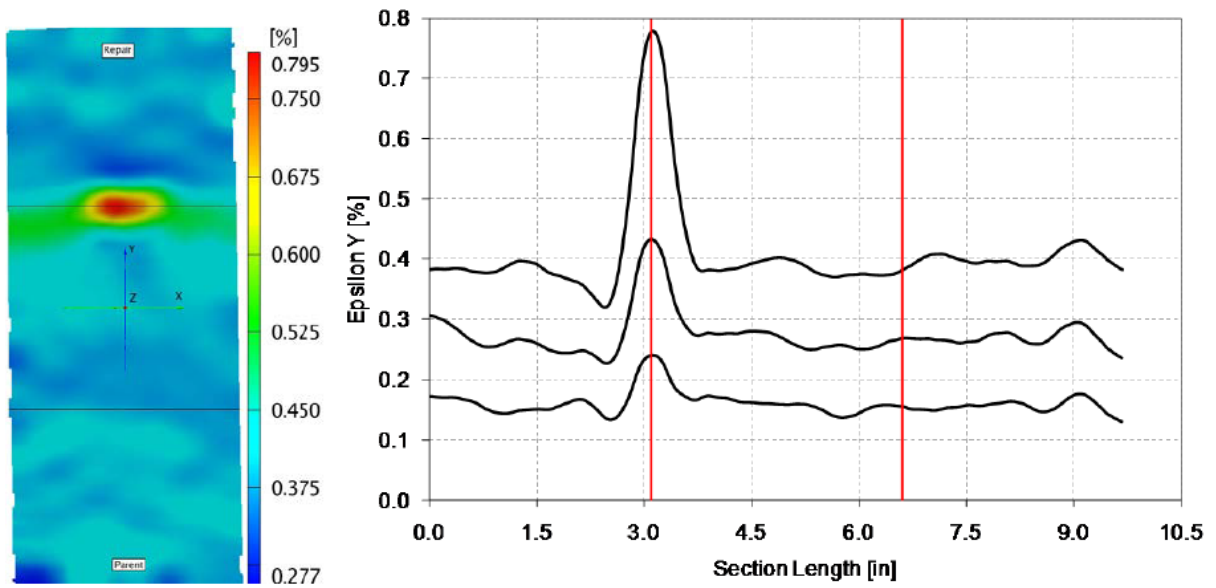


**Figure 95. Y-strain distribution 48-ply-E2-10-TF-RTA-2 scarf repair specimen**

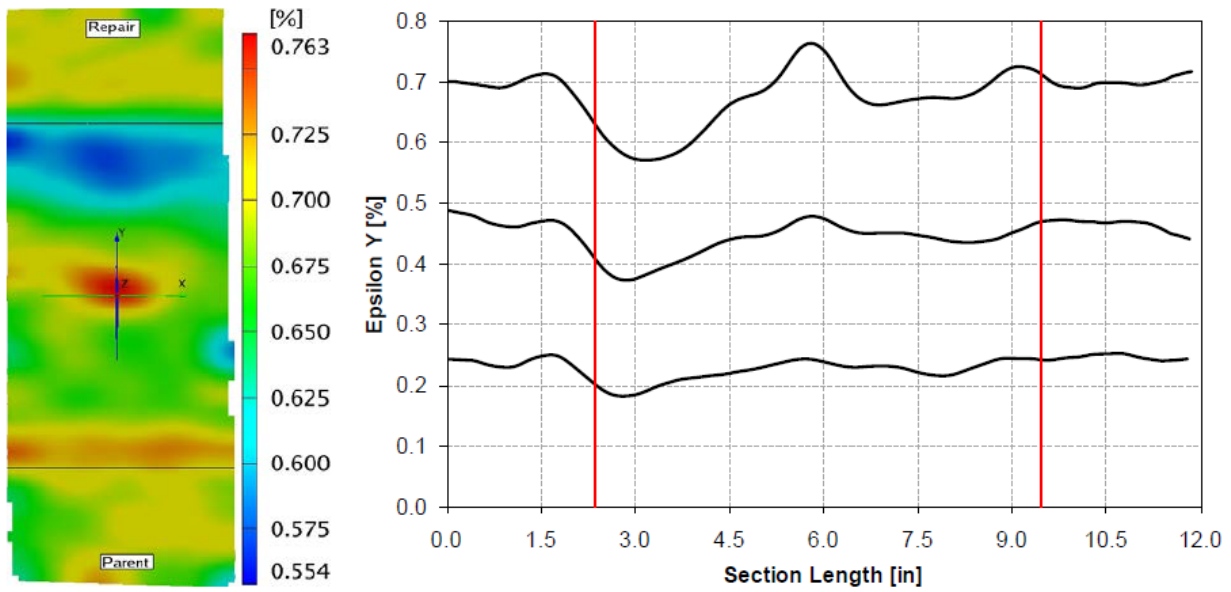


**Figure 96. Y-strain distribution 48-ply-E2-20-CN-RTA-03 scarf repair specimen**

Cyclic testing was conducted on 1:10 and 1:20 specimens impacted at all three damage sites in the scarf repair TN, TF, and CN to assess the durability of these repairs. The target fatigue life was 165,000 cycles and fatigue data are summarized in tables 4 and 5. It should be noted that because of the limited number of samples, an S-N curve to evaluate the fatigue capability of these damaged repairs could not be established. The 48-ply-E1-10 specimens survived 165,000 cycles at a load level equivalent to  $2500\mu\epsilon$ ,  $2000\mu\epsilon$ , and  $1000\mu\epsilon$  for TN, TF, and CN configurations, respectively. Similarly, the 48-ply-E2-10 specimens survived 165,000 cycles at a load level equivalent to  $1500\mu\epsilon$  for all configurations tested.

**Table 4. The 48-ply-10 fatigue data summary**

Panel Name	Specimen #	Frequency (Hz)	Number of Cycles	Fatigue Strain (microstrain)
48-PLY-E1-10-TN-RTF	1	2	36,873	3000
	2	2	165,000	2000
	3	2	165,000	2500
48-PLY-E1-10-TF-RTF	1	2	3540	3000
	2	2	165,000	2000
	3	2	9754	2500
48-PLY-E1-10-CN-RTF	1	2	249	2000
	2	2	165,000	1000
	3	2	7005	1500
48-PLY-E2-10-TN-RTF	1	2	519	3000
	2	2	24,519	2000
	3	2	165,000	1500
48-PLY-E2-10-TF-RTF	1	2	4	3000
	2	2	5538	2000
	3	2	165,000	1500
48-PLY-E2-10-CN-RTF	1	2	165,000	1500
	2	2	2829	1750
	3	2	17,514	1500

**Table 5. The 48-ply-20 fatigue data summary**

Panel Name	Specimen #	Frequency (Hz)	Number of Cycles	Fatigue Strain (microstrain)
48-PLY-E1-20-TN-RTF	1	2	165,000	3000
	2	2	165,000	3000
	3	2	165,000	3000
48-PLY-E1-20-TF-RTF	1	2	165,000	3000
	2	2	165,000	3000
	3	2	165,000	3000
48-PLY-E1-20-CN-RTF	1	2	122,540	3000
	2	2	165,000	3000
	3	2	165,000	3000
48-PLY-E2-20-TN-RTF	1	2	143,402	3000
	2	2	165,000	3000
	3	2	106,129	3000
48-PLY-E2-20-TF-RTF	1	2	78,087	3000
	2	2	106,538	3000
	3	2	165,000	3000
48-PLY-E2-20-CN-RTF	1	2	64,713	3000
	2	2	111,840	3000
	3	2	50,450	3000

All 48-ply-E1-20 specimens were cycled at a load equivalent to  $3000\mu\epsilon$  far field and all specimens tested survived 165,000 cycles of fatigue except 48-E1-20-CN-RTF-01, which failed at 122,540 cycles. All 48-ply-E2-20 specimens were cycled at a load equivalent to  $3000\mu\epsilon$  far field and the resulting average cycles to failure were 138,177 cycles, 116,542 cycles, and 75,668 cycles for the TN, TF, and CN, respectively. The cyclic data showed a reduction in the fatigue life (165,000 cycles for the undamaged scarf repairs) due to the inflicted damage.

Failure modes were very consistent for all specimens tested at room temperature and all specimens failed in the scarf joint. The dominant failure mode was a cohesive failure of the adhesive mainly in the 45 and 0 plies and a 90 ply peel/tension failure as shown in figures 97 and 98. For the specimens impacted at the CN, a visible disbond in the bondline was observed after failure, as shown in figures 98 and 99. It should be noted that figure 99 is shown for illustration purposes only as the environmental tests were not included in the scope of this study.



**Figure 97. Failure modes: 48-ply-E2-10-TN-RTA**

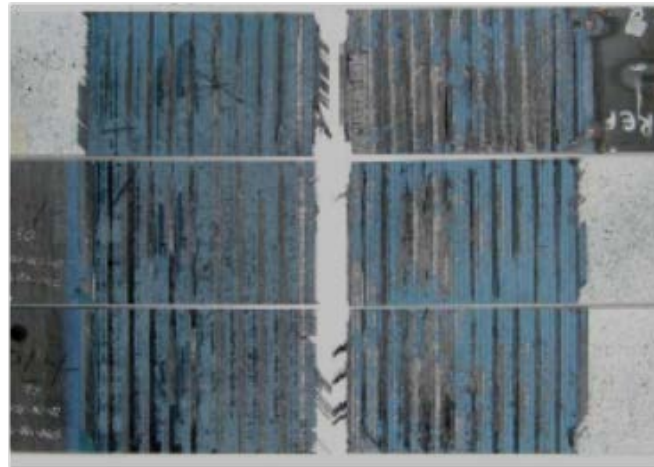


**Figure 98. Failure modes 48-ply-E2-20-CN-RTA**

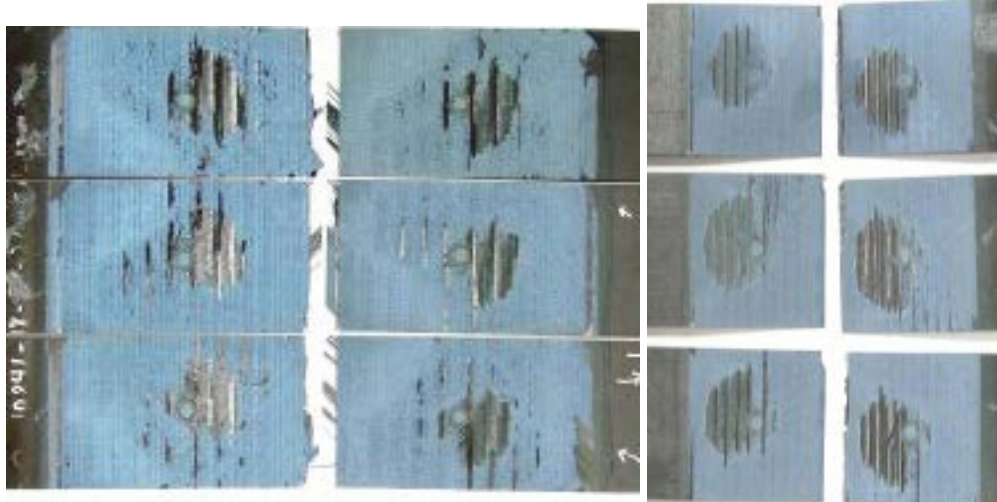


**Figure 99. Failure modes, environmental tests, 48-ply-E2-20-CN/48-ply-E1-10-CN (showing disbond/damage to the bondline due to impact at the center of the specimen)**

**4. CONTAMINATION/WEAK BOND INVESTIGATION RESULTS.**

All testing conducted for the contamination investigation was performed according to the test matrix outlined in table 6. There were 288 static specimens used for the investigation. Variables considered included two different substrate moduli (E1 and E2), two different scarf ratios, several test conditions, and numerous contaminants.

**Table 6. Contamination investigation test matrix**

Plies	Modulus	Scarf Rate	Test Condition	Contaminant													
				SH		JF		PS		PR		WA75		WA5		WA25	
32	E1	10	CT	3		3		3		3		3		3		3	
			RTA	3	3	3	3	3	3	3	3	3	3	3	3	3	3
		20	RTA	3	3	3	3	3	3	3	3	3	3	3	3	3	3
			180W	3		3		3		3		3		3		3	
	E2	10	RTA	3	3	3	3	3	3	3	3	3	3	3	3	3	3
			CT	3		3		3		3		3		3		3	
		20	RTA	3	3	3	3	3	3	3	3	3	3	3	3	3	3
			180W	3		3		3		3		3		3		3	

**4.1 SURFACE ANALYSIS PRIOR TO PANEL REPAIR**

The surface of all scarfed panels subjected to the contaminants, as well as the baseline uncontaminated panels, were analyzed prior to bonding the repairs using a contact angle measuring goniometer. Water drops were deposited on the scarfed surface, and the contact angle was

measured, as shown in figures 100–102. Low, medium, and high contact angles were achieved depending on the degree of wetting of the water (liquid used for analysis) with respect to the analyzed surface.

A low contact angle, shown in figure 100, was achieved for surfaces contaminated with SH, PR, and WA75 (scarfed panels that have reached moisture equilibrium and then dried back to 75% of the moisture equilibrium/saturation level). A low contact angle shows good surface wetting, but this does not necessarily mean that a good bond would be achieved. A medium contact angle was achieved with baseline uncontaminated specimens and WA0 panels, as shown in figure 101. A high contact angle was achieved with JF-contaminated scarfed panels, as shown in figure 102. A low contact angle yields a high SFE, whereas a high contact angle yields a low SFE. A high SFE yields efficient wetting before cure, but does not necessarily mean a good bond would be achieved. A surface contaminated with polar compounds analyzed with water yields a high SFE, but not necessarily a good bond. Contaminated surfaces with SH, PR, and WA75 had a high SFE, but a poor bond. All contact angle/SFE experiments used water as the testing liquid. Water is a very polar liquid (with a powerful permanent dipole caused by the hydrogen adopting a partial positive charge and the oxygen a partial negative charge). This allows the water molecule to strongly bind to polar sites on the scarfed surface.



**Figure 100. Low contact angle**

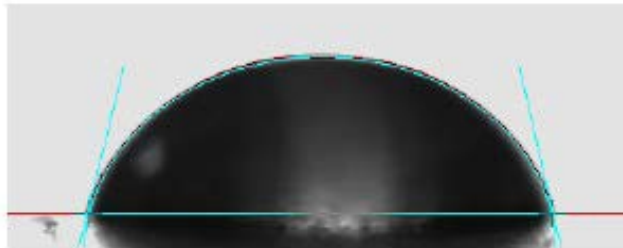


**Figure 101. Medium contact angle**

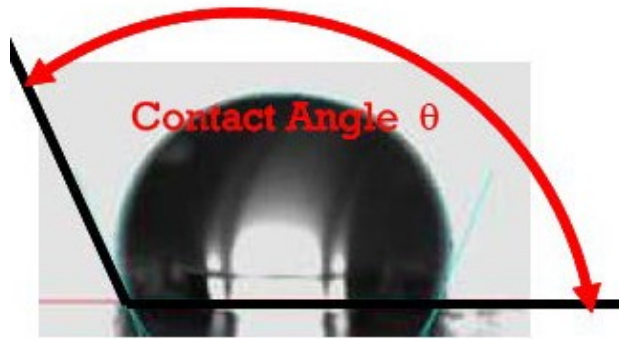


**Figure 102. High contact angle**

The contaminant occupies secondary bonding sites on the scarfed surface (cured resin system and fibers in parent). The contaminant prevents the uncured adhesive from occupying those sites. This lessens full adhesion of the cured adhesive to the fiber/resin surface. During cure cycle, the contaminant migrates to and from the surface into the adhesive and can chemically react with the adhesive at high temperatures. Contaminants, in sufficient quantities, brought to the surface during the cure phase may separate to form porosity.

Contamination with water increased the apparent scarfed SFE. This increase in free energy does not translate into a better bond. The scarfed surface must be dried and the apparent SFE must be dropped to the original value before a good bond can be produced. For the contact angle measuring experiment, the surface contaminated with water is highly polar; the analysis is conducted with water that is also highly polar, causing the water drop to wet the water- contaminated surface.

The scarfed laminates contaminated with SH exhibited a high SFE because SH is a highly polar compound, thus, attracting the highly polar water drops, which in turn wet the surface. The SH and its additive package could possibly interfere with the adhesive cure reaction.

The scarfed laminates contaminated with JF exhibited a low SFE because the JF, unlike water, SH, and PR, is a non-polar compound, thus, repelling the very polar water droplet. The water molecules in the water droplet tended to bind to themselves, rather than to the JF-contaminated scarfed surface, as shown in figure 102. This results in a large contact angle with a water droplet and a low apparent SFE. This would lead to poor spreading of the repair adhesive over the scarfed surface. Figures 103 and 104 show the contact angle and apparent SFE results. As shown in the figures, the JF-contaminated panels yielded the highest contact angles and the lowest SFE. The SH-, PR-, and WA75-contaminated panels yielded the lowest contact angles (the most efficient wetting) and the highest SFEs.

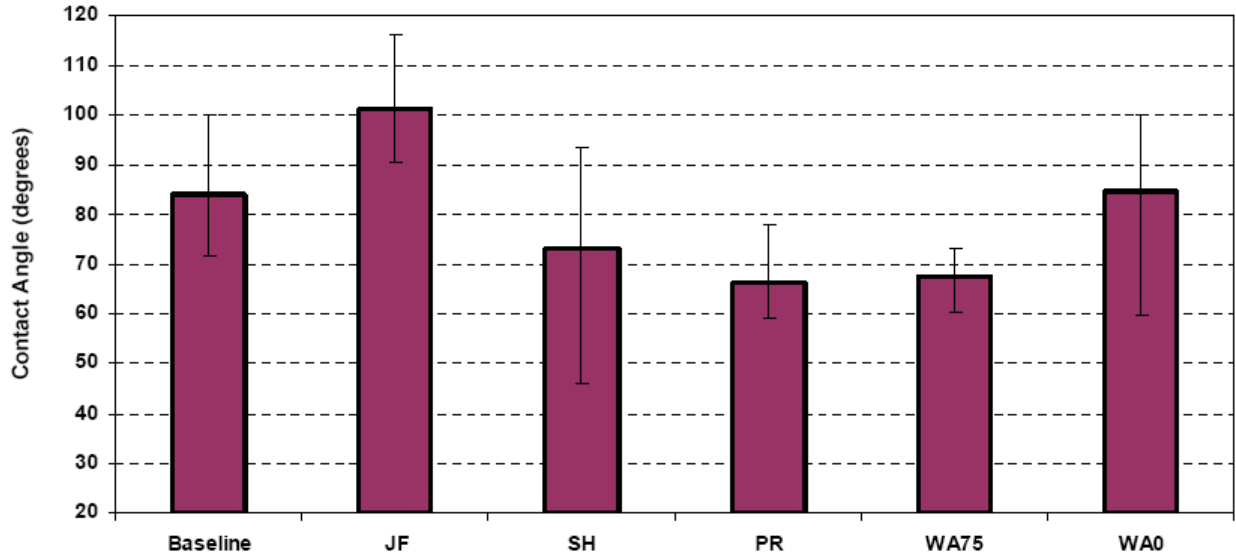


**Figure 103. Contact angle measurements**

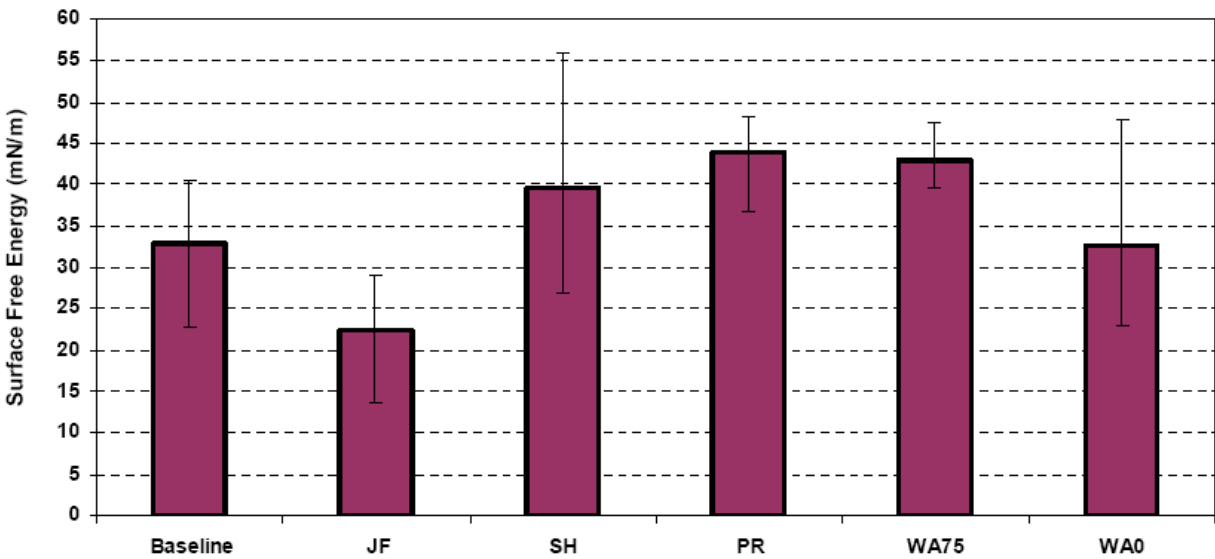


**Figure 104. SFE measurements**

#### 4.2 CONTAMINATION/WEAK BOND INVESTIGATION DATA SUMMARY

Figure 41 in section 2.8 shows a sample moisture absorption/desorption curve for traveler specimens used to monitor moisture content for the water-contaminated samples. The scarfed panels were conditioned until moisture equilibrium was achieved, resulting in approximately 1% total moisture content, as shown in the figure. The scarfed panels were then dried to achieve moisture levels equivalent to 75%, 50%, and 25% of the level achieved at equilibrium, denoted as WA75, WA50, and WA25. The WA0 samples were fully dried after reaching moisture equilibrium. It took less than 24 hours to dry the 32-ply scarfed panels to a 75% moisture equilibrium level (0.75% effective moisture content by weight), approximately 5 days to dry the

32-ply scarfed panels to a 50% moisture equilibrium level (0.5% effective moisture content by weight), approximately 18 days to dry the 32-ply scarfed panels to a 25% moisture equilibrium level (0.25% effective moisture content by weight), and more than 40 days to dry the 32-ply scarfed panels to a 0% moisture level (i.e., fully dry).

Figures 105–108 show the normalized ultimate strength results of contaminated scarf repairs tested to failure at cold temperature (-65°F), RTA, and elevated temperature wet (180W) for substrates of two different stiffnesses (E1 and E2). E1 corresponds to a quasi-isotropic lay-up, whereas E2 corresponds to a stiff lay-up. Two different scarf rates, 1:10 and 1:20, were considered for this study. The 1:10 scarf rate specimens were tested at cold and room temperature, whereas the 1:20 scarf rate specimens were tested at room temperature and elevated temperature wet.

It should be noted that in addition to the variability due to contamination, there are other sources of variability in the mechanical data that should be considered: thickness variation in the parent panels, variation in the scarf length from panel to panel, variation in the repair lay-up process (relative humidity [RH], operators, surface preparation, repair ply orientation, oven cure), variation in the compaction level/bondline porosity from panel to panel (debulking the repair system has not yielded repeatable results) yielding varying porosity (especially bondline porosity between panel to panel). This variability should be considered carefully when reviewing the data shown in figures 105–108 and caution should be exercised when interpreting the data from the figures.

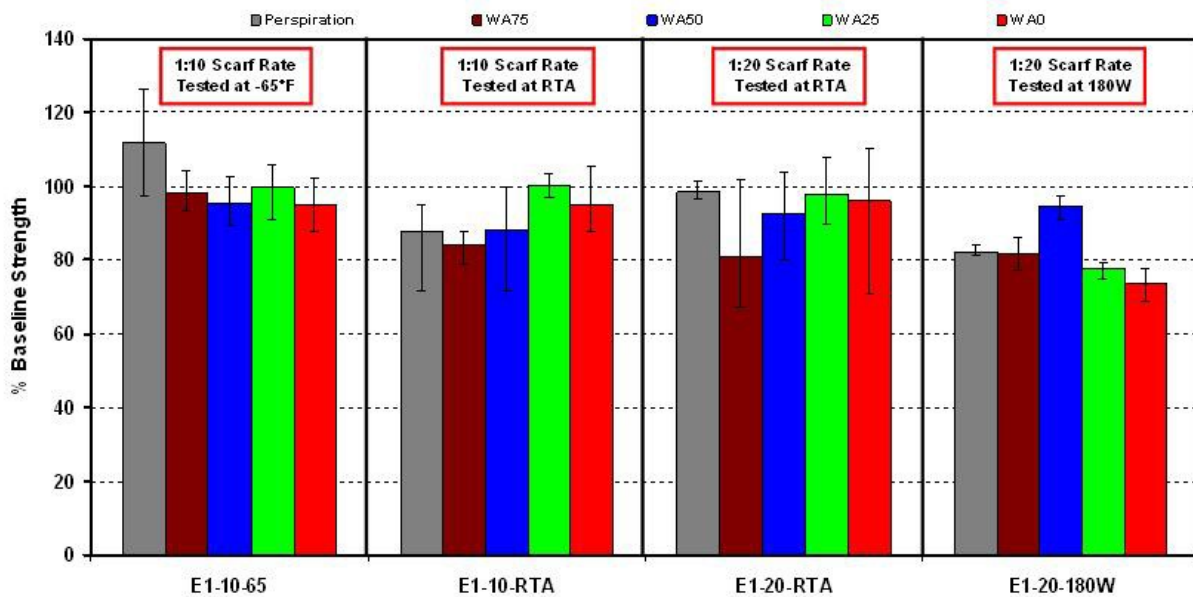
Failure loads for each of the four configurations shown in figure 105 were normalized with respect to the average ultimate load of the uncontaminated joints for that configuration tested at the same temperature. All contaminated samples from configuration 1 (1:10 scarf rate tested at -65°F) were normalized with respect to the average ultimate load of the uncontaminated 1:10 scarf joints tested at -65°F. Similarly, all contaminated samples from configuration 2 (1:10 scarf rate tested at RTA) were normalized with respect to the average ultimate load of the uncontaminated 1:10 scarf joints tested at RTA.

Figure 105 shows significant scatter in the contamination results obtained across environmental conditions. Specimens exposed to PR yielded a maximum average strength degradation of 18% for the 1:20 scarf rate specimens tested at 180W (E1-20-180W). The minimum individual data point recorded for all PR-contaminated specimens corresponds to 28% strength reduction (1:10 scarf rate tested at RTA). Specimens exposed to WA75 yielded a maximum average strength degradation of 19% for the 1:20 scarf rate specimens tested at RTA (E1-20-RTA). The minimum individual data point recorded for all WA75-contaminated specimens yielded 33% strength reduction with respect to the baseline uncontaminated strength of the same joint (1:20 scarf rate tested at RTA).

Specimens exposed to WA50 yielded a maximum average strength degradation of 12% for the 1:10 scarf rate specimens tested at RTA (E1-10-RTA). The minimum individual data point recorded for all WA50 contaminated specimens yielded 28% strength reduction with respect to the baseline uncontaminated strength of the same joint (1:10 scarf rate tested at RTA). Specimens exposed to WA25 yielded a maximum average strength degradation of 23% for the 1:20 scarf rate specimens tested at 180W (E1-20-180W). The minimum individual data point recorded for all WA25-contaminated specimens yielded 25% strength reduction with respect to the baseline uncontaminated strength of the same joint (1:20 scarf rate tested at 180W).

Specimens exposed to WA0 yielded a maximum average strength degradation of 27% for the 1:20 scarf rate specimens tested at 180W (E1-20-180W). The minimum individual data point recorded for all WA0 specimens yielded 31% strength reduction with respect to the baseline uncontaminated strength of the same joint (1:20 scarf rate tested at 180W). These results suggest that drying the samples did not restore the original strength of these repairs.

A previous study [25] has shown that water absorption may cause irreversible changes in the epoxy network. Absorption and diffusion of water in polymeric material is related to the free volume, which depends on molecular packing (degree of cure). Also, water molecules that attach to the polymer through H bonds disrupt the interchain H bonds, induce swelling, and plasticize the polymer. Moisture absorption is a function of degree of cure. Imperfectly cured systems allow moisture ingress because of the relatively loose chemical network structure. Moisture absorption causes irreversible changes in the epoxy network (evidence provided by the study of absorption-desorption cycling) [25].



**Figure 105. Normalized strength of PR- and water-contaminated panels (E1 lay-up)**

As shown in figure 106, specimens exposed to PR yielded a maximum average strength degradation of 15% for the 1:10 scarf rate specimens tested at -65°F (E2-10-65). The minimum individual data point recorded for all PR-contaminated specimens corresponds to 37% strength reduction (1:10 scarf rate tested at -65°F). Specimens exposed to WA75 yielded a maximum average strength degradation of 21% for the 1:20 scarf rate specimens tested at 180W (E2-20-180W). The minimum individual data point recorded for all WA75-contaminated specimens yielded 29% strength reduction with respect to the baseline uncontaminated strength of the same joint (1:20 scarf rate tested at 180W).

Specimens exposed to WA50 yielded a maximum average strength degradation of 17% for the 1:20 scarf rate specimens tested at 180W (E2-20-180W). The minimum individual data point recorded for all WA50-contaminated specimens yielded 41% strength reduction with respect to

the baseline uncontaminated strength of the same joint (1:20 scarf rate tested at 180W). Specimens exposed to WA25 yielded a maximum average strength degradation of 23% for the 1:10 scarf rate specimens tested at -65°F (E2-10-65). The minimum individual data point recorded for all WA25-contaminated specimens yielded 36% strength reduction with respect to the baseline uncontaminated strength of the same joint (1:10 scarf rate tested at -65°F).

Specimens exposed to WA0 yielded a maximum average strength degradation of 29% for the 1:20 scarf rate specimens tested at 180W (E2-20-180W). The minimum individual data point recorded for all WA0 specimens yielded 40% strength reduction with respect to the baseline uncontaminated strength of the same joint (1:20 scarf rate tested at 180W). With the exception of the E2-10-RTA configurations, static data showed a lower static strength for panels contaminated with PR, WA75, WA50, WA25, and WA0 (compared to the baseline/uncontaminated joint strength).

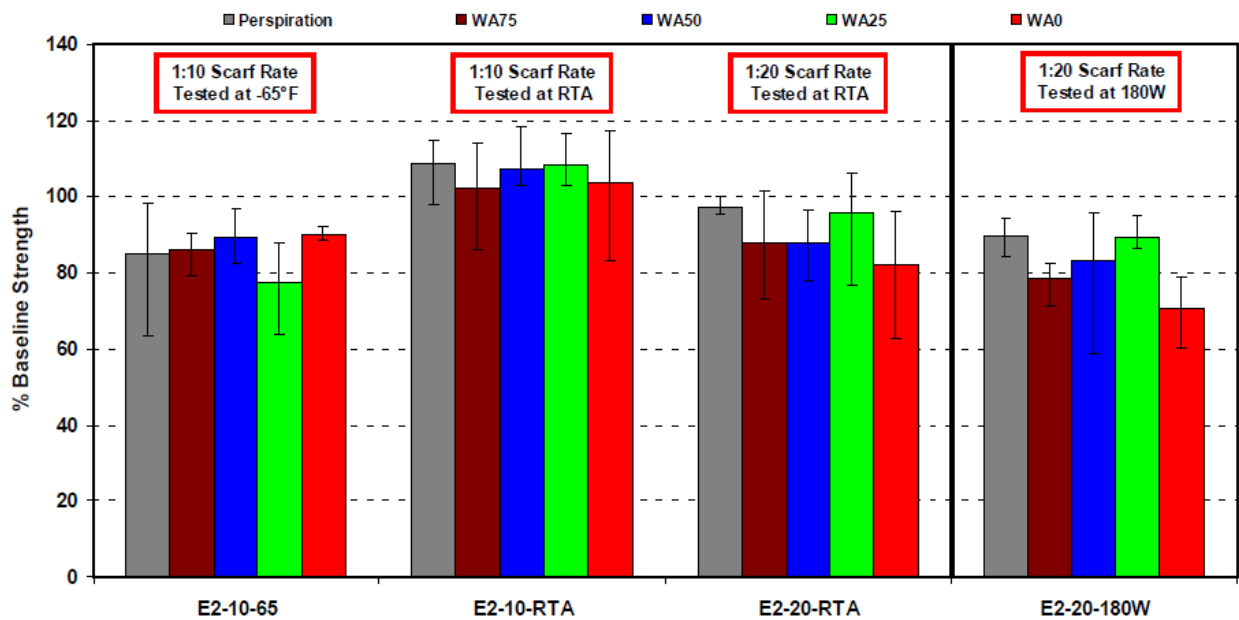


**Figure 106. Normalized strength of PR- and water-contaminated panels (E2 lay-up)**

As shown in figure 107, the minimum individual data points recorded for all PS-, JF-, and SH-contaminated specimens correspond to 8% strength reduction for PS (1:10 scarf rate tested at RTA), 5% strength reduction for JF (1:10 scarf rate tested at RTA), and 12% strength degradation for SH-contaminated panels. As shown in figure 108, the minimum individual data points recorded for all PS-, JF-, and SH-contaminated specimens correspond to 9% strength reduction for PS (1:10 scarf rate tested at RTA), 5% strength reduction for JF (1:20 scarf rate tested at RTA), and 6% strength degradation for SH-contaminated panels.

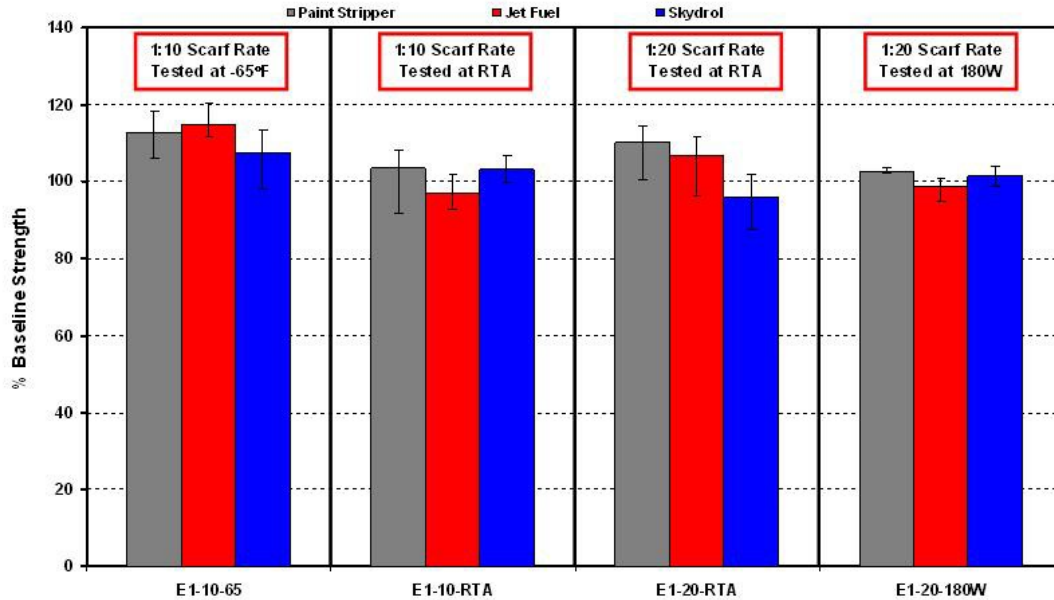


Figure 107. Normalized strength of PS-, JF-, and SH-contaminated panels (E1 lay-up)

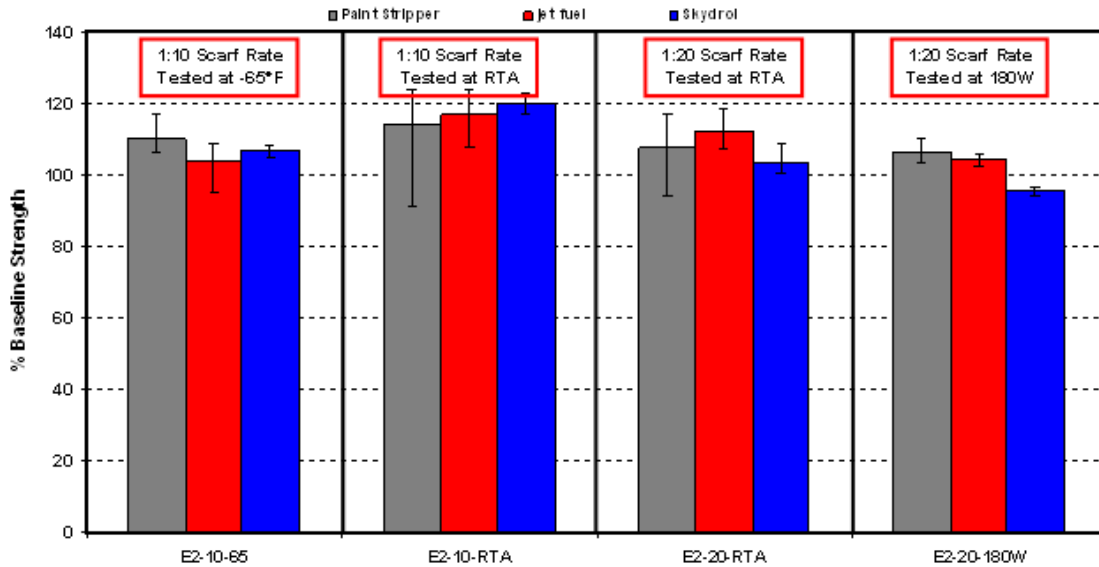
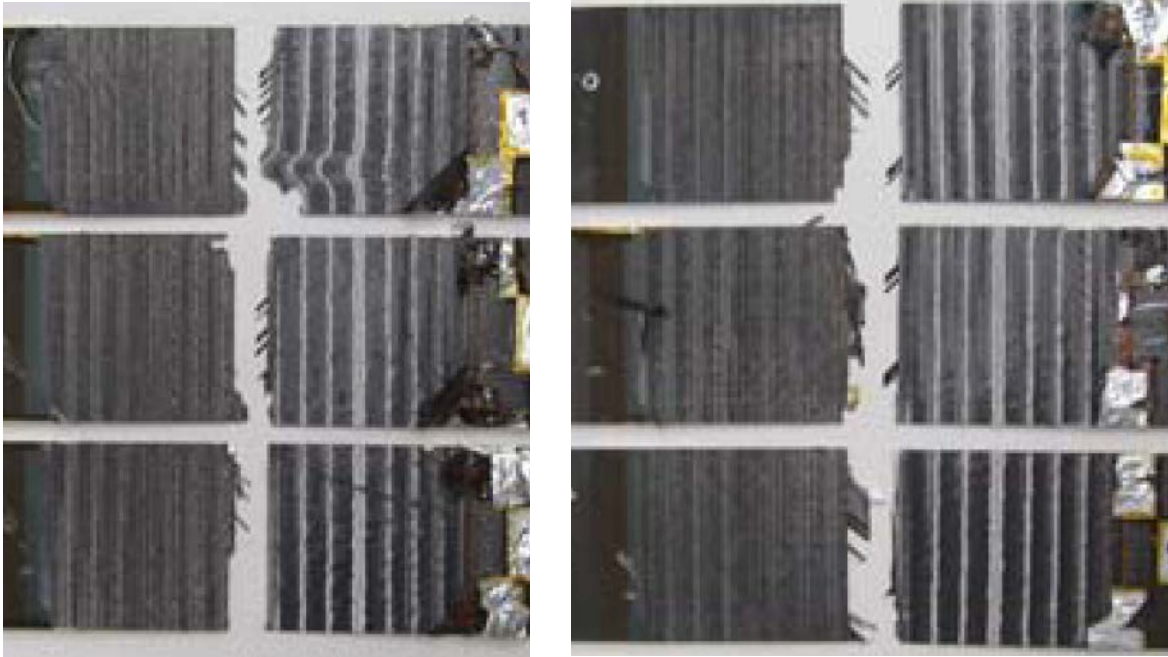
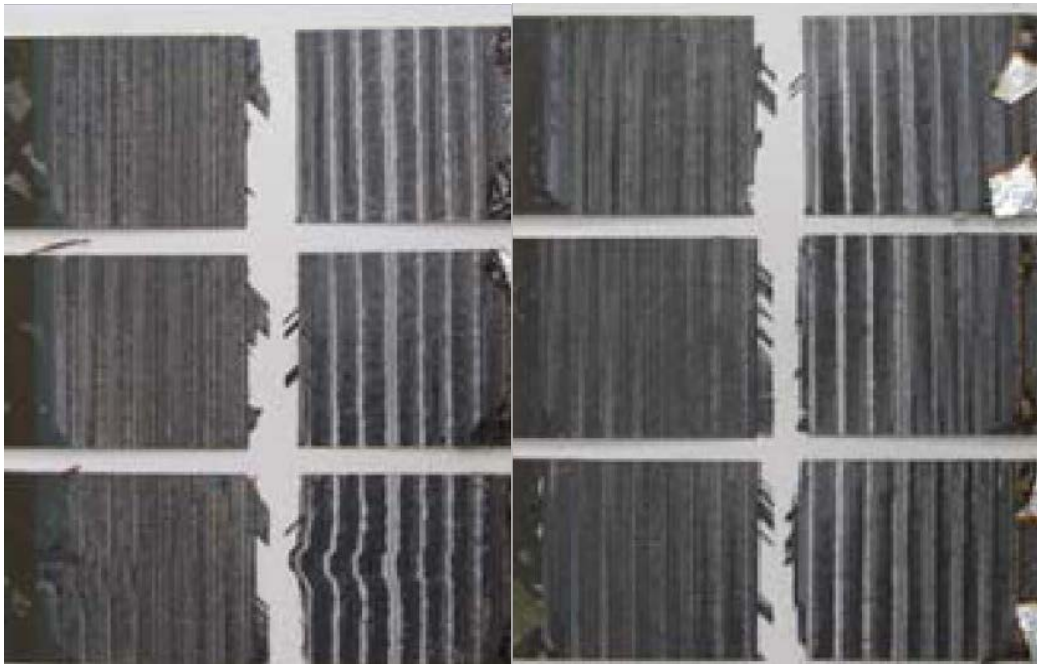


Figure 108. Normalized strength of PS-, JF-, and SH-contaminated panels (E2 lay-up)

Failure modes were very consistent for all specimens within the same test conditioning environment. The dominant failure mode for the specimens tested at room temperature and at -65°F was a combination of an adhesive failure and a 45°/90° ply failure in the scarf joint. The elevated temperature wet specimens all yielded adhesion failures, as shown in figures 109 and 110.



**Figure 109. Failure modes 32-ply-E1-20-JF-180W/32-ply-E1-20-PR-180W**



**Figure 110. Failure modes 32-ply-E1-20-SH-180W/32-ply-E1-20-WA75-180W**

## 5. CONCLUSIONS AND RECOMMENDATIONS

The objective of this research program was to evaluate the ultimate strength and durability of bonded scarf repairs applied to solid laminates subjected to impact damage and pre-bond contamination. Repair data were generated for repair systems representative of factory and field

repairs. The factory repairs were used as a baseline for the damage tolerance investigation, whereas the field repairs were used as a baseline for the contamination investigation.

Five different contaminants were used for the contamination investigation: jet fuel (JF), paint stripper (PS), Skydrol (SH), water (WA75, WA50, WA25, WA0), and perspiration (PR). The JF and SH panels were soaked in the contaminants for 30 days; PR (salt water) was applied to the surface prior to bonding, PS panels were exposed to the contaminant for 6 days, and water panels were exposed to moisture at 85%RH at a temperature of 180°F until moisture equilibrium was achieved. Once 100% moisture equilibrium was achieved, panels were subsequently dried to achieve %saturation levels of 75%, 50%, 25%, and nearly 0% (fully dry).

The surfaces of all scarfed subpanels were analyzed prior to repair using a contact angle measurement goniometer. Low, medium, and high contact angles were achieved depending on the degree of wetting of the water (liquid used for analysis) with respect to the contaminated surface. A low contact angle showed good surface wetting but did not necessarily yield a good bond, as demonstrated by the mechanical test results. A medium contact angle was achieved with baseline uncontaminated specimens and WA0 panels. A high contact angle was achieved with the JF-contaminated scarfed panels. Contamination with water and PR increased the apparent scarfed surface free energy (SFE). This increase in free energy did not translate into a better bond. Contamination with SH exhibited a high SFE because SH is a very polar compound, thus, attracting the very polar water drop, which in turn wet the surface. Contamination with JF exhibited a low SFE because JF, unlike water, SH, and PR, is a nonpolar compound and, thus, repels the very polar water droplet. The proposed surface analysis method provided promising results and demonstrated the importance of pre-bond surface evaluation methods to assess fitness of a composite surface for bonding. The mechanical test data confirmed the detrimental effects of pre-bond contamination on the static strength of bonded scarf repairs. Individual data points recorded for PR- and water-contaminated panels yielded strength reductions exceeding 33% at 180W. Similarly, individual data points recorded for JF-, PS-, and SH-contaminated panels yielded strength reduction exceeding 7%. Only static data were obtained for the contamination investigation. Cyclic testing should be conducted to further understand the effects of pre-bond contamination on bond durability and subsequent residual strength.

Coupons used for the damage tolerance investigation were repaired using the double vacuum debulking process in which the repair patch was consolidated prior to bonding it to the cured scarfed parent. All 18-ply and 48-ply repair specimens were impacted at three different impact sites in the scarf region: the tip of the scarf from the far side (TF), the tip of the scarf from the near side (TN), and at the scarf center (CN). For the 18-ply 1:10 scarf rate configurations, the TN specimens yielded the highest residual strength, followed by the TF specimens, and the CN specimens yielded the lowest residual strength. For the 1:20 scarf rate configurations, the TF specimens yielded the highest residual strength, followed by the TN specimens, and the CN specimens yielded the lowest residual strength. The magnitude of the strength degradation observed for the 1:10 scarf repairs was more severe than that observed for the 1:20 scarf repair samples. For the same impact energy level inflicted on the 1:10 and 1:20 scarf repairs, the percentage of residual structurally sound bond area in the joint was higher for the larger scarf repairs (1:20).

For the 48-ply specimens, for all configurations tested with the exception of 48-ply-E2-20, the TN specimens produced the highest residual strength (smallest damage area), followed by the TF specimens, and the CN specimens yielded the lowest strengths (largest damage area). For the 48-ply-E2-20 configuration, the TF specimens had a higher strength than the TN specimens, but the CN specimens yielded the lowest residual strength. The magnitude of the strength degradation observed for the 1:10 scarf repairs was more severe than that observed for the 1:20 scarf repair samples. For the same impact energy level inflicted on the 1:10 and 1:20 scarf repairs, the percentage of residual structurally sound bond area around the damage was higher for the larger scarf repairs (1:20). Large scatter was observed in impact damage formation from the impact tests and, subsequently, in the repair strength tests, particularly for the 18-ply laminate; however, the scatter does not negate the general trends that were observed.

The results of the damage tolerance investigation demonstrated that the residual strength of damaged scarf repairs is dependent on the damage location in the repair. The results are based on specimens tested at room temperature and, thus, environmental effects have to be investigated and more extensive durability studies performed to establish the capability of these damaged repairs and their associated residual strength.

The long-term durability and damage tolerance of adhesively bonded structures and repairs are key elements in the acceptance and implementation of bonded technology by original equipment manufacturers (OEMs) and operators in the repair of composite primary structural elements. Interfacial bond formation and degradation is a complex mechanism that has to be rigorously studied and understood. Most failures reported in the literature are interfacial failures resulting from a deficient bonding process yielding weak bonds susceptible to environmental degradation that deteriorate over time and potentially lead to catastrophic failures. The problem is further exacerbated by the lack of inspection methods to interrogate the structural integrity of degraded interfaces and detect weak bonds and repairs. Results from the current study emphasize the importance of rigorous validated repeatable processes to warrant the structural integrity of bonded structures and repairs. This substantiation should be conducted during the design/certification of a structure.

Some important considerations related to bonded repairs can be summarized as follows:

- OEM/factory repair system substantiation—whereas these systems may be used in the factory environment, with the possibility of processing parts in the autoclave using the parent systems, these systems (requiring autoclave pressure for optimum performance) may not be used in maintenance depots.
- Limitations associated with out of autoclave systems—whereas these systems have to be used in the maintenance environment, rigorous process substantiation and validation is necessary for optimum performance. Inadequate processes may yield porous repairs, weak interfacial bonds due to improper surface preparation, pre-bond contamination, ineffective/inadequate cure cycle, and improper choice of materials that may have serious implications of the residual strength of the bonded structure leading to potentially catastrophic failures. Furthermore, these systems may have a much lower strength capability as compared to the parent systems.

- The integrity of the bonded structure depends on the integrity of the bonded interface, which is dependent on a clean, chemically active surface prior to bonding and, thus, is a direct result of the bonding process
- Process substantiation and validation—rigorous procedures are necessary to ensure the structural integrity of bonded structures and repairs. The use of adequate processes specific to the substrate materials is a key to the structural integrity of the repaired part. Process documentation is necessary to ensure that all steps have been adequately followed during the bonding process.
- Education and training—there is a need for education and training of mechanics, inspectors, and engineers involved in the design, implementation, and inspection of the bonded repair. Because of the chemical characteristics of the various systems used for bonding and repair, it is important to understand the capabilities and limitations of the specific systems used. Caution should be exercised when applying results from one configuration to the next. A robust substantiation for the systems used is necessary to understand their capability once bonded together in a single combined structure/joint.

## 6. REFERENCES

1. Tenney, D.R. et al., “NASA Composite Materials Development: Lessons Learned and Future Challenges,” NASA Report LF99-9370, 2009.
2. Stickler, Patrick B., “Composite Materials for Commercial Transport – Issues and Future Research Direction,” *ASC 17th Annual Technical Conference*, 2002.
3. “Guide for the Design of Durable, Repairable, and Maintainable Aircraft Composites” AE-27, SAE, August 1997.
4. Shyprykevich, P., Tomblin, J., Ilcewicz, L., Vizzini, A.J., Lacy, T.E., and Hwang, Y., “Guidelines for Analysis, Testing, and Nondestructive Inspection of Impact-Damaged Composite Sandwich Structures,” FAA report DOT/FAA/AR-02/121, March 2003.
5. SAE International, Composite Materials Handbook-17 (CMH-17), Volume 3-G, “Polymer Matrix Composites Material Usage, Design, and Analysis,” 2009.
6. FAA Advisory Circular AC 20-107B, Composite Aircraft Structure, September 8, 2009.
7. Davis, M.J., Janardhana, M., and Mac Kenzie, A., “A Rigorous Approach to Certification of Adhesive Bonded Repairs,” *FAA Workshop on Certification of Adhesive Bonded Structures and Repairs*, Seattle, Washington, June 16-18, 2004.
8. Davis, M.J., Janardhana, M., and Wherrett, SQNLDR, A., “Adhesive Bonded Repair Technology: Supporting Aging Aircraft,” presented at the *Ageing Aircraft Users Forum*, Brisbane, May 2006.
9. Baker, A., Chester, R., and Mazza, J., “Bonded Repair Technology for Aging Aircraft,” RTO-MP-079, Manchester, United Kingdom, October 8-11, 2001.

10. Armstrong, K. and Barrett, R., *Care and Repair of Advanced Composites*, Second edition, SAE International, Armstrong, K.B., Bevan, L.G., and Cole II, W.F., eds., Warrendale, Pennsylvania, June 2005.
11. Davis, M. and Tomblin, J., “Best Practice in Adhesively Bonded Structures and Repairs,” FAA report DOT/FAA/AR-TN06/57, April 2007.
12. Tomblin, J., Salah, L., Borgman, M., and Welch, J., “Bonded Repair of Aircraft Composite Sandwich Structures,” FAA report DOT/FAA/AR-03/74, February 2004.
13. Baker, A.A., “Bonded Composite Repair of Metallic Aircraft Components—Overview of Australian Activities,” 79th meeting of the *AGARD Structures and Materials Panel on Composite Repair of Military Aircraft Structures*, Seville, Spain, October 3–5, 1994.
14. Davis, M.J., Chester, R.J., Perl, D.R., Pomerleau, E., and Vallerand, M., “Honeycomb Bond and Core Durability Issues; Experiences Within CREDP Nations,” *Aging Aircraft Conference*, Williamsburg, Virginia, August 31-September 2, 1998.
15. Davis, M. and Bond, D., “Principles and Practices of Adhesive Bonded Structural Joints and Repairs,” *International Journal of Adhesion and Adhesives*, Volume 19, Issues 2–3, April 1999, pp. 91–105.
16. Davis, M., “Safety Risks in Applying Damage Tolerance Analysis to Certification of Adhesively Bonded Structures and Joints,” *Aircraft Airworthiness and Sustainment Conference*, Brisbane, Australia, July 2011.
17. Vakula, V.L. and Pritykin, L.M., “Polymer Adhesion, Basic Physico-Chemical Principles,” Ellis Horwood, Chichester, United Kingdom, 1991.
18. Comyn, J., “Adhesion Science,” The Royal Society of Chemistry, Cambridge, United Kingdom, 1997.
19. Stokes, R.J. and Evans, F., “Fundamentals of Interfacial Engineering,” Wiley–VCH, 1997.
20. Garbassi, F., Morra, M., and Occhiello, E., “Polymer Surfaces: From Physics to Technology,” Wiley–VCH, 1994.
21. Gdoutos, E.E., Pilatoukos, K., and Rodopoulos, C.A., “Failure Analysis of Industrial Composite Materials,” McGraw Hill, 2000.
22. Brady, R., “Comprehensive Desk Reference of Polymer Characterization and Analysis,” American Chemical Society, Oxford, United Kingdom, 2003.
23. “Handbook of Adhesion Technology,” Da Silva, L., Öchsner, A., and Adams, R., eds., Chapter 2 Theories of Fundamental Adhesion, pg 23, 2011.
24. Springer, G.S., “Environmental Effects on Composite Materials—Volume 3,” Technomic Publishing, Westport, Connecticut, 1988.

25. Hinley, J.A. and Connell, J.W., *Resin Systems and Chemistry: Degradation Mechanisms and Durability*, Chapter 1, “Long-Term Durability of Polymeric Matrix Composites,” Springer, 2011.
26. Abdelkader, A.F. and White, J.R., “Water Absorption in Epoxy Resins: The Effects of the Crosslinking Agent and Curing Temperature,” *Journal of Applied Polymer Science*, Vol. 98, 2005, pp. 2544–2549.
27. Comyn, J., “Structural Adhesives, Developments in Resins and Primers,” Chapter 8, A.J. Kinloch, ed., Elsevier Applied Science Publishers, London, England, 1986.
28. Bond, D., “The Effect of Environmental Moisture on the Performance and Certification of Adhesively Bonded Joints and Repairs,” FAA and CAA Workshop on Bonded Structures, Gatwick, October 26-27, 2004.
29. Davis, M.J. and Bond, D.A., “Certification of Adhesive Bonds for Construction and Repair,” *Aging Aircraft Conference*, St. Louis, Missouri, May 15-18, 2000.
30. Tomblin, J., Salah, L., Hoffman, D., and Miller, M., “Teardown Evaluation of a Decommissioned Boeing 737-200 CFRP RH Horizontal Stabilizer,” FAA report DOT/FAA/AR-12/1, October 2012.
31. Aniversario, R.B., Harvery, S.T., McCarty, J.E., et al., “Design, Ancillary Testing, Analysis, and Fabrication Data for the Advanced Composite Stabilizer for Boeing 737 Aircraft,” NASA CR 166011, Volume II, Final Report, December 1982.
32. Glen, S., “Non-Autoclave Processing of Advanced Composite Repairs,” *International Journal of Adhesion and Adhesives*, Vol. 19, Issues 2–3, April 1999, pp. 155–159.
33. Hou, T.H. and Jensen, B.J., “Double Vacuum Bag Technology for Volatile Management in Composite Fabrication,” *Polymer Composites*, Vol. 29, Issue 8, August 2008, pp. 906–914.